DEVELOPMENT OF HORIZONTAL VIBRATION-ASSISTED PULSED ELECTROCHEMICAL MACHINING SYSTEM

A Dissertation

by

ZHUJIAN FENG

Submitted to the Office of Graduate and Professional Studies of
Texas A&M University
in partial fulfillment of the requirements for the degree of

DOCTOR OF PHILOSOPHY

Chair of Committee,	Wayne Hung
Committee Members,	Bruce Tai
	Hamn-Ching Chen
	Hong Liang
Head of Department,	Andreas A. Polycarpou

August 2018

Major Subject: Mechanical Engineering

ABSTRACT

This research aims to understand flushing of byproducts between the anodic workpiece and the cathodic electrode in the electrochemical machining (ECM) process. The ion transport mechanism between the inter-electrode gaps under low vibration frequency applied on the workpiece has been theoretically analyzed and simulated. A series of holes have been machined on a 1018 steel plate by the presented device to evaluate the effects of vibration on machining depth and taper angle. Mathematical model and simulation model for ion transport between the anodic workpiece and the cathodic electrode were developed to illustrate the effects of vibration frequency on by-products' average flushing speed between the inter-electrode gaps. The results showed that the maximum machining depth (1584 μm) and the minimum taper angle (16.57°) achieved at 40 Hz vibration frequency and 10 μm vibration amplitude. Meanwhile, the simulation results showed that the maximum average flushing speed (0.3968 m/s) were obtained at this vibration frequency and vibration amplitude. There is a positive/negative correlation between the average flushing speed and machining depth/taper angle.

ACKNOWLEDGEMENTS

First, I would like to express my sincere appreciate to my committee chair, Dr. Wayne Hung, for his excellent guidance, patient and support during the completion of this research. I would never been able to finish my dissertation without his guidance.

Moreover, I also want to express my deepest gratitude to my committee members, Dr. Hamn-Ching Chen, Dr. Hong Liang and Dr. Bruce Tai. During my stay in Texas A&M University, they provide me with good advice, both on technical content and form of this research.

In addition, I need to show special thanks to my wife, Zhaofeng Li and my parents, for their extremely valuable help, continuous care, patience, encouragement, unconditional love and full support.

Finally, Thanks also go to my friends for their generous loans without any interests to help me complete my study period. I also want to extend my gratitude to colleagues and the faculty and staff of Department of Manufacturing & Mechanical Engineering Technology and Department of Mechanical Engineering for making my time at Texas A&M University a fantastic experience.

CONTRIBUTORS AND FUNDING SOURCES

This work was supervised by a dissertation committee consisting of Dr. Wayne Hung, Dr. Hong Liang and Dr. Bruce Tai of the Department of Mechanical and Professor Dr. Hamn-Ching Chen of the Department of Civil Engineering.

All work for the dissertation was completed by the student, under the advisement of Dr. Wayne Hung of the Department of Mechanical Engineering.

This work was made possible in part by CONACyt (Mexico) under Grant Number 1745678 and Agilent University Research Corporation (USA) under Grand Number 512433 & 2847.

Its contents are solely the responsibility of the authors and do not necessarily represent the official views of the CONACyt and Agilent University Research Corporation.

NOMENCLATURE AND ACRONYMS

Symbols

a_1, a_2, a_3	Constants that apply over several ranges of R_e
a_r	Particle acceleration along the radial direction (m/s^2)
A	Effective electrode area (mm^2)
$A(t), A'(t)$	Workpiece vibration travel distance (μm)
A_0	Gap between particle and workpiece surface at $t = 0$ (mm)
A_C	Cross-section area of conductor (mm^2)
A_p	Projected particle surface area (mm^2)
A_v	Anodic workpiece vibration amplitude (μm)
B	Magnetic flux density (WB/m^2)
c_b	Concentration of dissolved metal ions in the bulk (mole/L)
c_s	Concentration of dissolved metal ions at the anodic workpiece (mole/L)
c_{sat}	Saturation concentration of dissolved metal ions (mole/L)
C	Specific removal rate of workpiece (m^3/A/s)

C_1, C_2, C'_1, C'_2	Coefficient
C_{1018}	Cumulative specific removal rate for 1018 steel
C_d	Particle-fluid drag coefficient
C_{Domex}	Cumulative specific removal rate for Domex steel
C_E	$= M\kappa_e/zF\rho_a$ is machining parameter
C_p	Specific heat of electrolyte (J/kg/℃)
C_{RL}	Rotational lift coefficient
C_{vm}	Virtual mass coefficient which typically has a value of 0.5
d	Workpiece density (kg/m^3)
d_p	Particle diameter (m)
d_g	Gap between particle center and workpiece
D	Graham's diffusion coefficient
D_1, D_2	Hole dimeter at level 1 and level 2 (mm)
e_a	$= M/zF$ is the electrochemical equivalent for the anodic material
E	Applied voltage (Volt)

f	Vibration frequency (Hz)
f_e	Cathode electrode feed rate (μm/s)
F	Faraday's constant = 96,500 coulomb/mole
F'	Force (N)
F_b	Buoyance force (N)
F_B	Basset force (N)
F_c	Force generated in the armature coil (N)
F_d	Drag force (N)
F_{dv}	Driven force for vibration system (N)
$\overrightarrow{F_{ij}^{c}}$	Contact force acting on particle i by particle j (N)
$\overrightarrow{F_{i}^{f}}$	Particle-fluid interaction force on particle i (N)
$\overrightarrow{F_{i}^{g}}$	Gravitation force of particle i (N)
$\overrightarrow{F_{ik}^{nc}}$	Noncontact force acting on particle i by particle k or other sources (N)
F_p	Pressure gradient force (N)
F_{p-F}	Force of particle act on fluid (N)

F_{F-p}	Force of fluid act on particle (N)
F_r	Total force along the radial direction (N)
F_{RL}	Magnus lift force (N)
F_S	Saffman lift force (N)
F_{vm}	Virtual mass force (N)
F_x, F_y, F_z	Body force along the x, y, z direction respectively (N)
g	Inter-electrode gap (μm)
g_0, g'_0	Inter-electrode gap at time $t = 0$ (μm)
g_e	$= \frac{M\kappa_e E}{zF\rho_a f_e}$ is the equilibrium inter-electrode gap (μm)
G	Gravity force (N)
h	Machining depth (mm)
h_c	Conductor length (mm)
H	Height between level 1 and level 2 (mm)
i_p	Peak current density (A)
i_a	Average current density (A)

I	Current (A)
I_0	Initial current for PoweerTIG 255 EXT DC power supply (A)
I_b	Minimum current for PoweerTIG 255 EXT DC power supply (A)
I_{max}	Maximum driven current for armature coil (A)
I_p	Maximum current for PoweerTIG 255 EXT DC power supply (A)
$I_{vibration}$	Driven current for vibration table (A)
J	Current density (A/mm^2)
J_a	Average current density (A/mm^2)
J_l	Anodic limiting current density (A/mm^2)
J_p	Peak current density (A/mm^2)
K_1	Physical constant
K_v	Effective volumetric electrochemical equivalent (mm^3/A/s)
L	Gap distance in the electrolyte flow direction (μm)
L_a	Arc length of a simulation domain (μm)
L_c	Length of conductor in the gap (mm)

m	Mass dissolved from the anode (g)
$\dot{m}$	Mass removal rate (g/s)
m_A	Mass attached on armature coil (kg)
m_i	Mass of particle i (g)
m_p	Mass of particle (g)
M	Molecular mass of anodic workpiece (g/mole)
M'	Momentum (kg · m/s)
$\vec{N}$	Total flux of ion ($\mathrm{mole/m^2 s}$)
p	Pressure (Pa)
Q'	Energy (J)
r	Resistivity of electrolyte ($\Omega\, m$m)
r_p	Particle radius (μm)
r_{pi}	Particle injection rate (times/s)
R	Resistance of the conductor (Ohms)
R_e	Reynold's number

$R_{e\omega}$	Rotational Reynold's number
R_{ep}	Particle Reynold's number
R_g	Gas constant
S	Effective electrode area (mm^2)
S_{spin}	Spin parameter
S_*	Minimum gap size in PECM (m)
t, t'	Time (s)
t_{on}	Pulse on-time (s)
t_{off}	Pulse off-time (s)
t_p	Pulsed period time equals $t_{on} + t_{off}$ (s)
T	Electrolyte temperature (℃)
T_0	Initial temperature of electrolyte (℃)
T_{boil}	Boiling temperature of the Electrolyte (℃)
T_v	Vibration period time (s)
u, v, w	Electrolyte flow speed at x, y, z direction respectively (m/s)

u', v', w'	Electrolyte flow speed at x', y', z' direction respectively (m/s)
U_0	Amplitude of voltage pulse (V)
ΔU	Overpotential (V)
$\overrightarrow{v_i}$	Translations velocity of particle i respectively (m/s)
V	Removed anode material volume (mm^3)
$\dot{V}$	Volumetric material rate (m^3/s)
V_{ave}	Average particle flushing speed (m/s)
V_e	Electrolyte flow speed (m/s)
$\overrightarrow{V_F}$	Fluid phase flow velocity (m/s)
V_p, V'_p	Average particle flow speed (m/s)
V_w	Workpiece moving speed (μm/s)
w_t	Electrode tube thickness (μm)
x	Location of workpiece relative to the fixed origin (μm)
x_p, x'_p	Particle center location (μm)
z	Valence electrons of anode

α	Under-relaxation factor for particles
α_T	Temperature coefficient of the conductivity at T_0
δ	Diffusion layer thickness (µm)
δ_c	Conicity (%)
δ_p	Pulsating diffusion layer thickness
η_I	Current efficiency (%)
η_l	Current efficiency of metal dissolution J_l (%)
η_p	Current efficiency of metal dissolution at peak current density (%)
θ	Average temperature increment equals $T - T_0$ (℃)
θ_{boil}	Temperature increment from T_0 to T_{boil} (℃)
ρ_e	Electrolyte density (g/mm^3)
κ	Specific conductivity (S/mm)
κ_0	Electrolyte conductivity at T_0 (S/mm)
κ_e	Electrolyte conductivity (S/mm)
μ	Viscosity of the fluid (Pa·s)

ρ	Specific resistance or resistivity of the conductor ($\Omega \cdot$mm)
ρ_a	Anode material density (g/mm^3)
ρ_e	Electrolyte density (g/mm^3)
ρ_F	Fluid density (g/mm^3)
ρ_p	Particle density (g/mm^3)
τ_r	Particle relaxation time
φ	Angle between particle and horizontal reference (°)
Ω	Relative fluid-particle angular velocity (rad/s)

Acronyms

CBN	Cubic Boron Nitride
CFD	Computation Fluid Dynamics
DC	Direct Current
DEM	Discrete Element Model
DNS	Direct Numerical Simulation
ECM	Electro-chemical Machining
EDM	Electro-discharged Machining
FEM	Finite Element Method
HSLA	High strength low alloy
IEG	Inter-electrode gap
JECM	Jet Electrochemical Machining
MRR	Material removal rate
PECM	Pulsed Electrochemical Machining
PECMM	Pulsed Electrochemical Micromachining

TFM	Two Fluid Model
WECM	Wire-type Electrochemical Machining

TABLE OF CONTENTS

Page

LIST OF FIGURES

Page

LIST OF TABLES

Page

1 INTRODUCTION

The emphasis on fuel economy and passenger safety has led to a remarkable increase in the usage of high strength low alloy (HSLA) steel in automobile application due to their high strength-to-weight ratio, higher fatigue resistance and better corrosion resistance as compared to carbon steel. Engineering components using HSLA steels usually have complex geometries and are manufactured by various metal forming or machining techniques. Fabrication of holes and slots on HSLA steel, for example, is a common work procedure when designing engineering components. Drilling, milling, punching, laser cutting and electro-discharged machining (EDM) are general processes that are applied to shape a component. However, microstructural damages, expensive deburring and time-consuming residual stress relieving treatments prompt researchers to consider alternative manufacturing techniques [1].

Cubic boron nitride (CBN) and coated carbide tools are required when machining HSLA steels due to its high strength and poor machinability. High energy is required to shear chips which results in thermal-induced defects in the materials and costly tool wear. When punching/stamping HSLA steels, it requires high energy, very tough yet hard cutting tool material, high stiffness of tool holder, are pre-requisites for successful punching holes on HSLA steels due to work-hardening property of HSLA steels. Besides, impurities, such as rust spots and non-metallic inclusion, leave on the grooves of machined surfaces [2], which are unacceptable for some applications. Although laser cutting has the advantages of no mechanical cutting forces and tool wear, its high energy-consumption, low material

removal rate (MRR), tapering cutting profile, thermally induced residual stress on laser cut surfaces are inherent drawbacks of this process. In the EDM process, a conductive material can be removed without mechanical contact forces and independent of material hardness. Although EDM can be used to form features on HSLA steels, but a defective EDM'ed subsurface and a relatively slow MRR limit the application of EDM for demanding and high-volume applications. A recast layer after EDM'ing is under high residual stress and may contain voids or micro-cracks; heat affected zone beneath recast layer undergoes microstructure morphing; insufficient flushing leads to abnormal discharging and resulting in extensive electrode wear. In all traditional and nontraditional processes, inevitable burrs are formed and must be removed in subsequent operations that further drives up the lead time and manufacturing cost.

Electrochemical machining (ECM), introduced in early 1960s in defense and aerospace industries, has been extended to many other industries, such as automobile, tools and dies, medical, and, recently, in micro manufacturing. This technique, based on the principle of controlled atomic-level anodic dissolution, has been used to fabricate complex shapes from any electrically conductive components. This is particularly useful to shape engineering alloys that are difficult to be machined, such as HSLA steels, tool steels, tungsten carbides and super alloys. Moreover, ECM does not induce any thermal or mechanical stresses/surface effects on the workpiece, generates no burr, has no tool wear, yet can achieve excellent surface quality as in electrochemical polishing. Eliminating secondary processes for deburring and stress relieving, the ECM is a promising technique to machine/polish HSLA steels if a decent MRR can be achieved.

Ion transport movement is the basic mechanism that controls the MRR in the ECM. When two electrically conductive materials are closely placed in the presence of an electrolytic fluid that conducts ions, the anodic workpiece releases ions towards the cathodic electrode. If the cathodic electrode (tool) moves at a controlled feed rate and motion toward anode, a desirable shape can be formed on the anodic workpiece. An electrolyte flows between the anodic workpiece and the cathodic electrode to enhance ion transport, maintain the temperature, and flush the resulted debris. If the newly formed by-products in the inter-electrode gap (IEG) are not effectively flushed away from an anode surface, cumulative ions would be stagnant and inhibits further ion dissolution, therefore, affecting the MRR and the quality of ECM'ed profile. Thus, increasing the ion transport rate and effective flushing of by-products are keys to improve the MRR. The movement of ions is controlled by three processes [3]:

i) Migration, i.e. movement under the influence of the electric field;
ii) Diffusion, i.e. movement due to the ion concentration gradients in the solution;
iii) Convection, i.e. bodily movement of the electrolyte solution; this is mainly affected by force agitation of the electrolyte in the ECM.

Therefore, a high MRR requires fast ion and by-products moving rates (i.e. migration rate, diffusion rate and convection rate). Researchers have attempted to utilize different techniques to improve these transport rates: by applying a high voltage to increase migration rate, by increasing high electrolyte flow rate to increase diffusion rate, by vibrating either the anodic workpiece or the cathodic electrode to increase the MRR. In

this study, we propose to study the flushing of by-products in the ECM while enhance the MRR with pulsed current and low frequency workpiece vibration.

2 OBJECTIVES AND SCOPES

Faraday's law and experimental data from literature showed that a higher voltage/current resulted in high MRR. However, more by-products and heat which required a higher electrolyte flow rate to be removed. An elaborate pumping system was needed to provide higher electrolyte flow rate, and a heavy machining frame was also required to maintain rigidity, which led to installing and operating costs increasing and presented a major limitation to the wide application of the ECM. This study incorporates the vibration into ECM to improve the electrolyte flow and avoid the installing and operating cost when compared with the high electrolyte flow.

The theoretical model studied the basis of the by-products traveling speed under the influence of low frequency vibration and the mechanism of the MRR increase when applied pulsed current. The simulation model aims to accurately predict the change of by-products' flushing speed under varied vibration amplitudes and vibration frequencies. The experiments verify the simulation model and theoretical hypothesis by linking the MRR and the ECM part quality with input parameters, such as peak current, current frequency, vibration frequency, vibration amplitude and feed rate.

The following sections detail the theoretical analysis, simulation modelling and experimental procedure. The specific tasks will be achieved as follows:

i) Investigating the ECM process theoretically, analyzing the influence of pulsed current and low frequency vibration on the MRR.

ii) Developing a simulation model to investigate the influence of vibration amplitude and vibration frequency on by-products' average convection rate.

iii) Constructing the experimental ECM system including workpiece vibration system, tool feeding system, pulsed DC power supply system and electrolyte circulation system. Horizontal feeding is developed.

iv) Comparing the theoretical results, the simulation results and the experiment results to reveal the influence of pulsed current, low frequency vibration on the by-products' convection rate and MRR.

The scope of this study is limited to:

i) Simulation using Star CCM+ and ANSYS Fluent software

ii) Select and justify using 1018 steel rather than the 550MC HSLA steel.

iii) Keep constant electrolyte concentration.

iv) Keep constant current frequency, but vary the vibration frequency in the range of 0-80 Hz.

.

3 BACKGROUND

3.1 Process Selection for Energy Efficiency

Engineers often specify joined components to achieve a complex shape or specific function. Precision holes are required for close fit between joining parts, and quality holes are required for reliability when a component is used in dynamic and/or harsh environments. It is desired to select a manufacturing process to produce a quality hole in HSLA steel (for the automobile industry). Both traditional and non-traditional processes can be used to produce holes and similar features on a metal plate. Mechanical stamping or drilling can quickly fabricate holes on a metal plate, but excessive burr, significant plastic deformation, and microcracks may occur below the sheared surface. Laser and plasma cutting produce rough holes with severe thermal damage to the microstructure; the slow MRR of chemical etching limits its application on thin metallic sheets. Both the EDM and ECM can be used on conductive materials regardless of material strength or hardness. This is the key advantage over other traditional processes like drilling or punching. Although a variety of processes are available to fabricate features on a metallic plate, an ideal process should (i) consume minimal energy, and (ii) ensure maximum reliability and quality of the product.

To compare the energy consumption of punching, EDM and ECM, a ϕ8mm through hole was fabricated on $300 \times 100 \times 4.86$ mm aluminum and Domex HSLA steel by using punching, EDM and ECM, as shown in the Figure 3.1. The energies that are consumed were calculated with the assumption that all processes operated at ideal conditions [4].

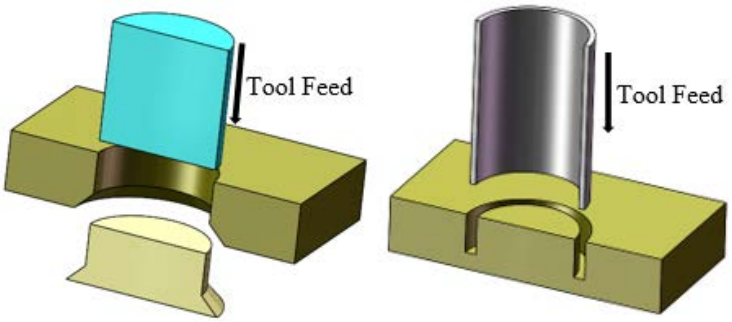

Figure 3.1 Illustration of punching with solid punch and EDM/ECM with a hollow electrode.

Mechanical punching requires a minimum cycle time. Punching force sheared the workpiece material partially, then generated a circular crack that propagated through the rest of the plate thickness, as shown in Figure 3.1. Figure 3.2 shows the surface microstructure after punching, EDM, and ECM. Since the hole size and hole shape were not uniform, honing was proposed to true the hole diameter while residual stress resulting from plastic deformation (Figure 3.2a) was removed by an annealing process. Energy consumed by the mechanical punching process was the highest since it included (i) shearing and honing, (ii) deburring by countersinking and (iii) annealing. The annealing energy dominated other terms.

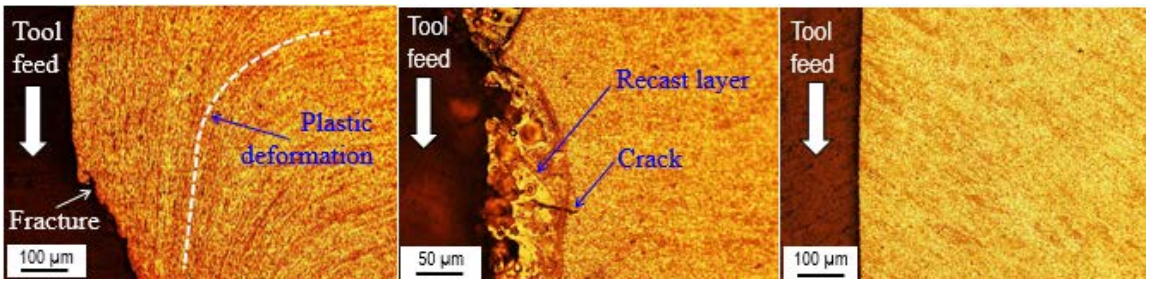

(a) (b) (c)

Figure 3.2 Microstructure of machining aluminum holes, reprinted from [4].

The EDM process removed material with a series of high energy sparks. The molten material from both the anodic workpiece and the cathodic electrode were redeposited onto the machined surface to form a defective recast layer. Non-uniform thermal contraction caused micro-cracks that even penetrated the parent material (Figure 3.2b). Energy for the EDM process included (i) discharging energy for the process and (ii) energy to remove the recast layer by honing. The energy for honing, however, was insignificant when compared to that for EDM.

The ECM process removed material by complex ion transport mechanisms in electrochemical reactions and ion diffusion. No microstructure damage was found at the optimal operating parameters (Figure 3.2c) and no secondary process was required. Energy for the ECM process was the lowest and depended solely on electrical energy for the process (Figure 3.3).

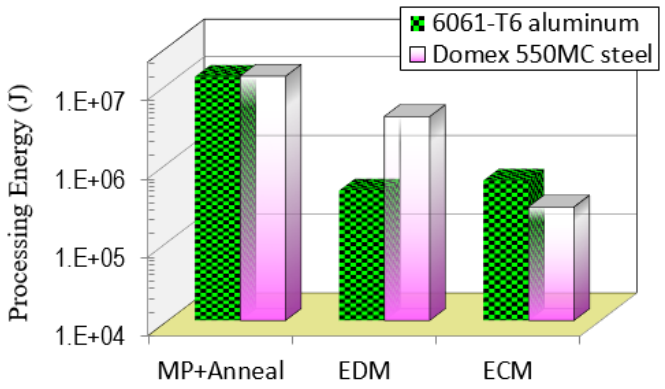

Figure 3.3 Comparing processing energy for different methods to fabricate a quality ϕ8mm through hole on a 300 × 100 × 4.86 mm plate, reprinted from [5].

Although shearing and honing energy were low, annealing energy was high for the mechanical punching process. The EDM required a secondary process to remove the recast layer. The ECM required the lowest processing energy, and manufactured best hole quality, and was hence the optimal choice to fabricate holes on HSLA steels.

3.2 Principal of ECM

Define:

A	Effective electrode area (mm^2)
c_b	Concentration of dissolved metal ions in the bulk (mole/L)
c_s	Concentration of dissolved metal ions at the anodic workpiece (mole/L)
c_{sat}	Saturation concentration of dissolved metal ions (mole/L)
C_E	$= M\kappa_e/zF\rho_a$ is machining parameter
D	Graham's diffusion coefficient
e_a	$= M/zF$ is the electrochemical equivalent for the anodic material
E	Applied voltage (Volt)
f_e	Cathodic electrode feed rate (μm/s)
F	Faraday's constant = 96,500 coulomb/mole
g	Inter-electrode gap (μm)
g_0	Inter-electrode gap at time $t = 0$ (μm)
g_e	$= \frac{M\kappa_e E}{zF\rho_a f_e}$ is the equilibrium inter-electrode gap (μm)
h_c	Conductor length (mm)

I	Current (A)
J	Current density (A/mm^2)
J_l	Anodic limiting current density (A/mm^2)
m	Mass dissolved from the anodic workpiece (g)
$\dot{m}$	Mass removal rate (g/s)
M	Molecular mass of anodic workpiece (g/mole)
R	Resistance of the conductor (Ohms)
t	Time (s)
V	Removed anode material volume (mm^3)
z	Valence electrons of anode
δ	Diffusion layer thickness (µm)
η_I	Current efficiency (%)
η_l	Current efficiency of metal dissolution J_l (%)
κ	Specific conductivity (S/mm)
κ_e	Electrolyte conductivity (S/mm)
ρ	Specific resistance or resistivity of the conductor (Ω ·mm)
ρ_a	Anode material density (g/mm^3)

When two electrically conductive materials are placed close in the presence of an electrolytic fluid that conducts ions, a high current is passed through this electrochemical circuit, the anodic workpiece releases ions toward the cathodic electrode, meanwhile the cathodic electrode moves at a controlled feed rate and motions toward the anode to shape

an anodic workpiece, as shown in Figure 3.4. An electrolytic fluid flows between the cathodic electrode and the anodic workpiece to maintain their temperature while flushing the dissolved debris.

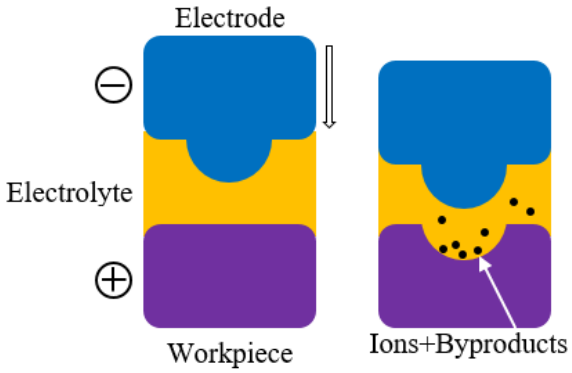

Figure 3.4 Schematic illustration of electrochemical cell.

The dissolved materials (cations) will carry positive charges and move through the electrolyte in the direction of the positive current, that is, towards the cathode. Similarly, the negatively charged ions travel towards the anode and are called anions. The movement of the ions is accompanied by the flow of electrons in the opposite sense outside the cell, and both actions are a consequence of the applied potential difference from the electric source [3].

Since the major composition of HSLA steel is iron (77-79%), during the ECM process several possible reactions may occur at the anodic workpiece and the cathodic electrode. The anodic reaction is the dissolution of iron at the anodic workpiece:

$$Fe \rightarrow Fe^{2+} + 2e^{-} \quad (3.1)$$

At the cathodic electrode, hydrogen and hydroxyl ions are produced:

$$2H_2O + 2e^{-} \rightarrow H_2 \uparrow + 2OH^{-} \quad (3.2)$$

Thus, the overall reaction of iron in the ECM process is:

$$Fe + 2H_2O \rightarrow Fe(OH)_2 + H_2 \uparrow \quad (3.3)$$

The ferrous hydroxide $Fe(OH)_2$ may react further with water and oxygen to form ferric hydroxide $Fe(OH)_3$:

$$4Fe(OH)_2 + 2H_2O + O_2 \rightarrow 4Fe(OH)_3 \quad (3.4)$$

The removed ferrous hydroxide $Fe(OH)_2$ and ferric hydroxide $Fe(OH)_3$ precipitate as sludges and some of the sludges deposit on the anode to form a barrier layer [6]. To make the process continue, a high-pressure electrolyte is pumped through the IEG to flush away the by-products. Meanwhile, the cathode moves toward the anode at a controlled feed rate and finally the anode will form an opposite shape of the cathode.

3.2.1 Theoretical Removal Rates

The iron dissolution rate (or MRR) is governed by the Faraday's two laws of electrolysis:

i) The amount of any substance dissolved or deposited is directly proportional to the amount of electricity which has flowed.

ii) The amounts of different substances deposited or dissolved by the same quantity of electricity are proportional to their chemical equivalent weights.

The Faraday's two laws of electrolysis are combined to give the theoretical material removal equation:

$$m = \frac{MIt}{zF} \tag{3.5}$$

Then the volumetric removal rate of the anode material MRR is:

$$\text{MRR} = \frac{MI}{zF\rho_a} \tag{3.6}$$

The electrolyte between the anodic workpiece and the cathodic electrode can be simplified to a conductor. According to Ohm's law, the current I flowing in a conductor, i.e. volume of electrolyte between the cathodic electrode and the anodic workpiece, is directly proportional to the applied voltage E:

$$E = IR \tag{3.7}$$

$$R = \frac{h_c \rho}{A} = \frac{h_c}{A\kappa} \tag{3.8}$$

Combine Equations (3.7) and (3.8), the current density can be derived:

$$J = \frac{I}{A} = \frac{E}{RA} = \frac{EA}{Ah\rho} = \frac{\kappa_e E}{h_c} \tag{3.9}$$

Consider two parallel electrodes with a constant voltage E applied across them, as shown in Figure 3.5(a). Assuming constant conductivity and neglecting overpotential, the width

of the gap between two electrodes depends only on machining time. Let the gap be $g(t)$ and at beginning be g_0. From the Faraday's law, the machining speed of this traditional ECM is:

$$\dot{g}(t) = \frac{\dot{V}}{A} = \frac{MI}{zF\rho_a A} = \frac{MJ}{zF\rho_a} \tag{3.10}$$

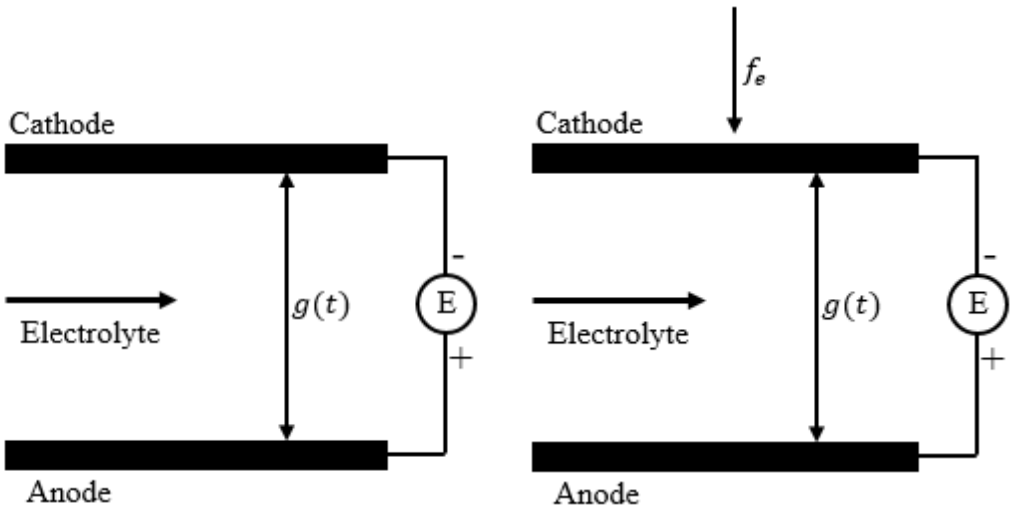

Figure 3.5 Set of plane parallel electrodes.

3.2.2 Current Efficiency

The current efficiency, η_I, is defined as the ratio of the observed amount of metal dissolved to the theoretical amount predicted from the Faraday's law, for the same specified conditions of electrochemical equivalent, current, etc.

If the metal ions dissolve in one valency form z, at current I, we can write:

$$\eta_I = \frac{\dot{m}}{(M/zF)I} \times 100\% \tag{3.11}$$

3.2.3 Variation of Gap Width with Machining Time

For an actual ECM, the cathode moves toward the anode at a constant feed rate f_e, as shown in Figure 3.5(b). If 100% current efficiency is also assumed, the rate of change of gap relative to the cathode surface is:

$$\frac{dg}{dt} = \frac{MJ}{z\rho_a F} - f_e \tag{3.12}$$

Substitution Equation (3.9) into (3.12), then:

$$\frac{dg}{dt} = \frac{C_E E}{g} - f_e \tag{3.13}$$

where

$$C_E = M\kappa_e / zF\rho_a \tag{3.14}$$

is a machining parameter and:

$$g = h_c \tag{3.15}$$

Equation (3.13) has the solution [3]:

$$t = \frac{1}{f_e}\left[g(0) - g(t) + g_e \ln\frac{g(0) - g_e}{g(t) - g_e}\right] \tag{3.16}$$

where

$$g_e = \frac{C_E E}{f_e} = \frac{M\kappa_e E}{zF\rho_a f_e} \tag{3.17}$$

The gap g_e is the equilibrium gap, or the steady-state solution to Equation (3.13) for $dg/dt = 0$.

A useful relationship for determining the equilibrium feed-rates can also be obtained from Equation (3.17):

$$f_e = \frac{e_a J}{\rho_a} \tag{3.18}$$

where

$$e_a = M/zF \tag{3.19}$$

is the electrochemical equivalent for the anodic material.

Three practical cases are now of interest:

i) When $f_e = 0$, that is, no cathode movement, Equation (3.13) has the solution:

$$g^2(t) = {g_0}^2 + 2C_E E t \tag{3.20}$$

The gap then increases indefinitely with the square root of the machining time, as shown in Figure 3.6.

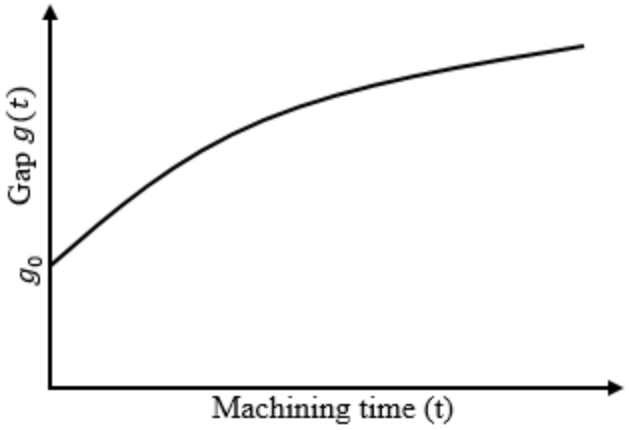

Figure 3.6 Indefinite increase of gap with machining time (zero feed-rate), reprinted from [3].

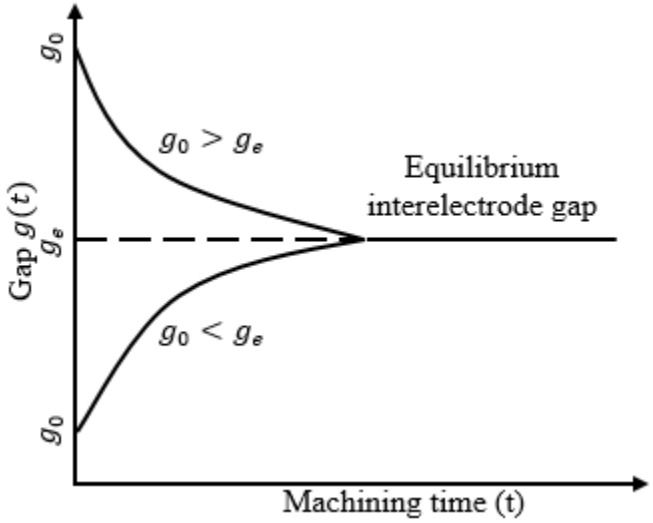

Figure 3.7 Variation of gap width with machining time (constant feed-rate), reprinted from [3].

ii) An increasing gap is not usually desired in the ECM, particularly when an accurate shape must be produced on the anode. Accordingly, fixed mechanical movement of the cathode is much more common. Thus, when Equation (3.16) is used to compare the gap with the machining time, and if the initial gap is

greater than the final gap, the gap width is seen to decrease with time to its equilibrium value. When the gap is initially smaller than the steady-state value, it increases to equilibrium width. This dependence of the gap width on machining time is illustrated in Figure 3.7.

iii) Finally, the condition $g(t) = 0$ implies a short circuit between the cathodic electrode and the anodic workpiece; and values of $g(t)$ less than zero are physically impossible.

3.2.4 Double Layer Diffusion Layer Model

For steady state metal dissolution process, the anode current density can be written as [7]:

$$J = \frac{zFD}{\eta_l}\frac{c_s - c_b}{\delta} \tag{3.21}$$

In the ECM, c_b usually is 0 and δ is determined by the prevailing hydrodynamic conditions. Upon increasing current density under otherwise constant conditions, c_s increases and eventually reaches the value of the saturation concentration c_{sat} leading to precipitation of anodic salt film. The anodic limiting current density is thus defined by Equation (3.22):

$$J_l = \frac{zFD}{\eta_l}\frac{c_{sat} - c_b}{\delta} \tag{3.22}$$

J_l is an important quantity in the ECM since surface finish, anode potential and reaction stoichiometry may differ drastically depending on whether dissolution is carried out above or below the limiting current density.

A duplex diffusion layer model is used to describe mass transport in PECM [7] which is similar to that originally proposed for pulse plating. According to this model, at the anode, there is a Nernst diffusion layer with the thickness δ and the value of δ is determined by hydrodynamic conditions, as shown in Figure 3.8. The diffusion layer may be divided into two parts, a pulsating diffusion layer and outer diffusion layer. The thickness of pulsating diffusion layer is δ_p. The dissolved metal ion concentration in pulsating diffusion layer is a periodic function of time. In addition, the thickness of the outer diffusion layer is $\delta_p' = \delta - \delta_p$ in which the concentration of dissolved metal ion is constant. The proposed duplex diffusion layer model is a gross simplification of real behavior. However, the results obtained by this approximate model are close to those obtained by other more complex models. In addition, it has the benefits of yielding simple expressions and providing a good physical insight into the mass transport processes in PECM [7].

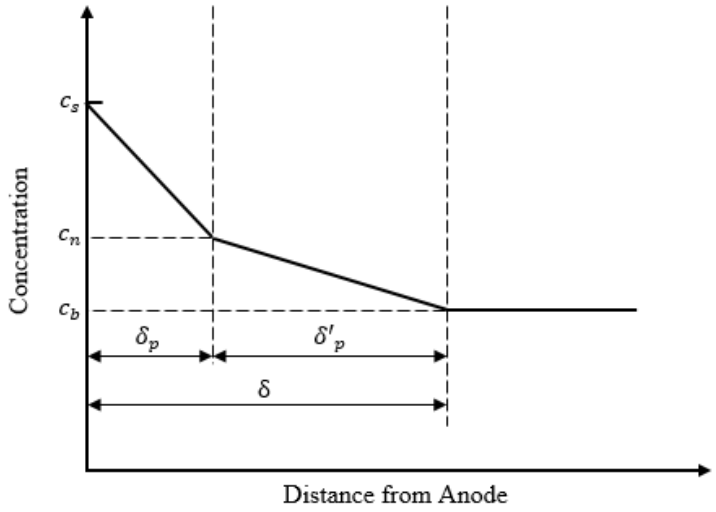

Figure 3.8 Schematic representation of duplex diffusion layer model, reprinted from [7].

3.3 Literature Review

Advantages of the ECM are plenty. However, the main advantages of the ECM are offset by:

i) The challenge of accuracy and process stability resulting from the complex and stochastic nature of the IEG [8-11]. Varying electrolyte conductivity [6] in the IEG caused by hydrogen gas bubbles generation and electrolyte heating [3, 6, 8, 12-14]. Electrolyte flow field distribution significantly affects the machining accuracy in the ECM. Some flow field disrupting phenomena, such as cavitation [3, 6, 13], striations [3, 15], slug formation [6, 8, 14, 16], can result in abnormal dissolution and uneven sparking [12, 14, 17]. The stray current in the side gap region due to the electric potential and conductive electrolyte existed between the anodic workpiece and the cathodic electrode. Consequently, the remarkable overcut caused by the persistent metal removal

at the side wall [18] adversely affects the dimension accuracy of machined component [3, 12-15, 19].

ii) Low MRR, lack of prediction of the MRR and optimization machining parameters theory [20] due to its complex nature, along with the need of proper tool design [3, 8, 13, 21, 22] especially for complicated component, are major challenges encountered by the ECM investigators.

iii) Surface quality control is another concern when using the ECM technique to manufacture alloys due to the non-uniform MRR, non-conductive inclusions and high grain boundary etching rates.

To improve the MRR and machining quality in the ECM, numerous techniques are proposed: variation of ECM, high current/voltage, pulsed current/voltage, electrolyte flow, electrode feed rate, mechanical vibration either on the anodic workpiece or the cathodic electrode, ultrasonic vibration either on the cathodic electrode or the electrolyte. The following sections review the effect of these factors on the MRR and the machining qualities.

3.3.1 ECM Techniques

Jet electrochemical machining (JECM), as shown in Figure 3.9, is a variation of the ECM where the electrolyte is pumped through a nozzle to form a jet. A potential difference was applied between the nozzle and workpiece and the current transferred by the jet electrolyte. Complicated shapes, as shown in Figure 3.10, were machined with the motion of the nozzle [23, 24].

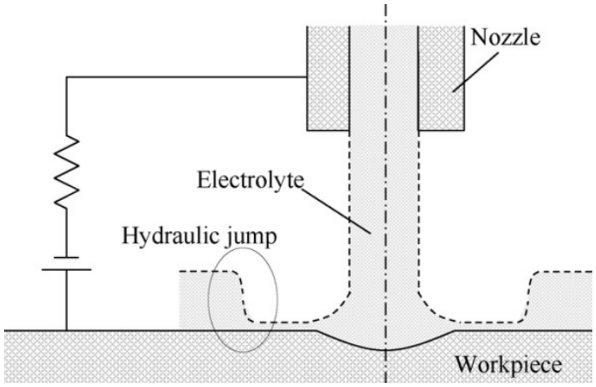

Figure 3.9 Schematic illustration of electrolyte jet machining, reprinted from [24].

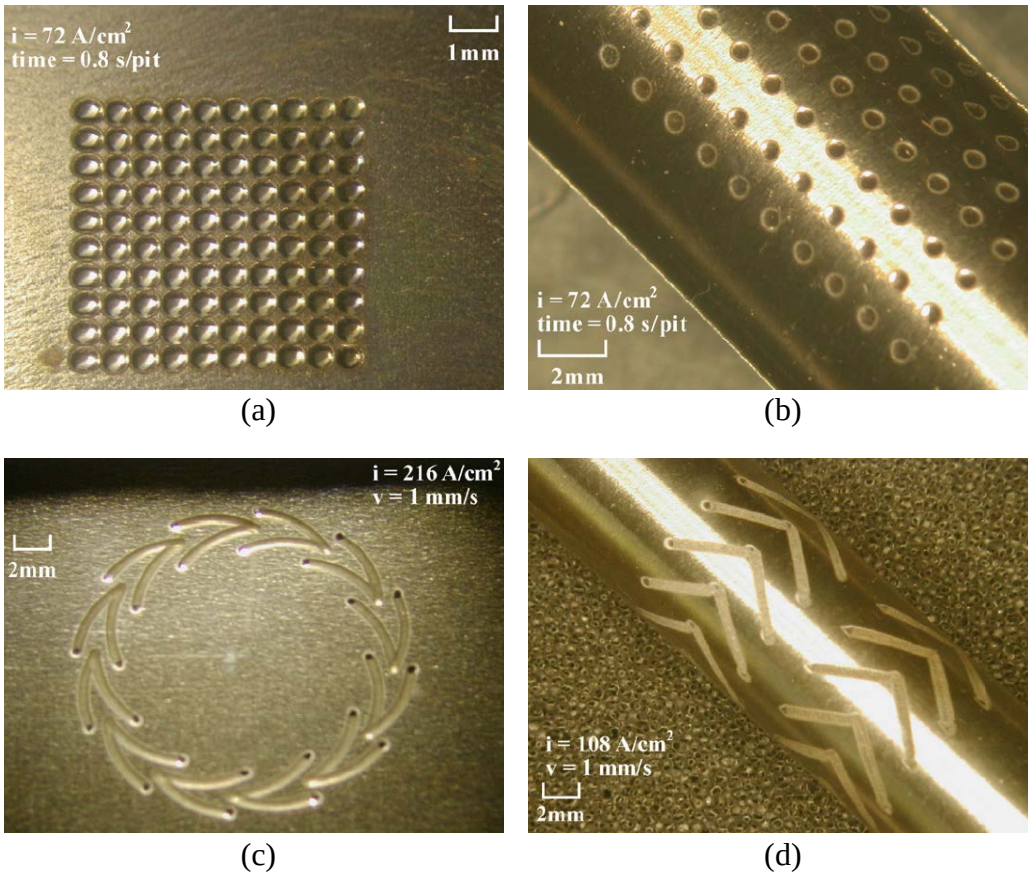

(a) (b)

(c) (d)

Figure 3.10 Complicated shapes machined by JECM, reprinted from [23].
(a) Pit array on plate; (b) pit array on cylinder; (c) groove on plate; (d) grove on cylinder

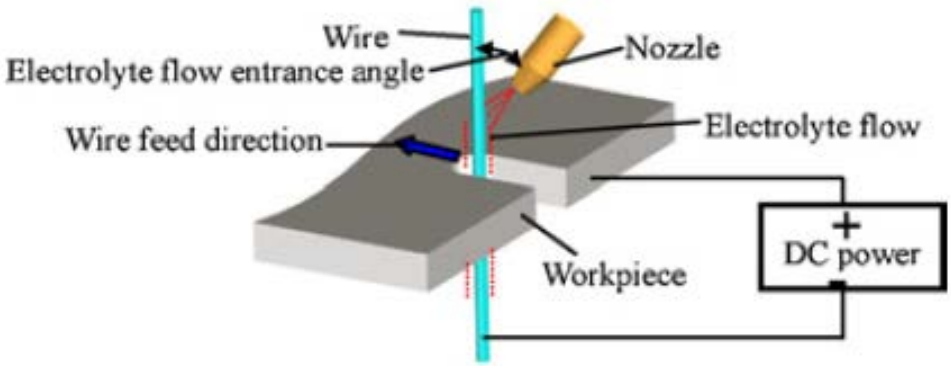

Figure 3.11 Schematic diagram of micro wire ECM with electrolyte flushing, reprinted from [25]

The WECM (wire type ECM), is shown in Figure 3.11, has been developed to machine high aspect ratio micro structures [25-32]. The wire electrode used in WECM must be rigid enough to withstand the forces due to generated bubbles and inadvertent physical contact between the tool and workpiece.

A hybrid machining center consisting of EDM, ECM and mechanical milling was developed by Kurita [33, 34], as shown in Figure 3.12. The EDM surface was improved to 0.06 μm Ra by applying ECM lapping. Similarly, a hybrid process of grinding and ECM to machine precise small holes on hard-to-machine materials was developed by Zhu [35], as shown in Figure 3.13. Precision holes of diameters of 0.6 mm with sharp edges and without burrs had been produced. The hybrid processes were developed to enhance the machining advantages and to minimize the potential disadvantages that were usually accompanied with the individual techniques.

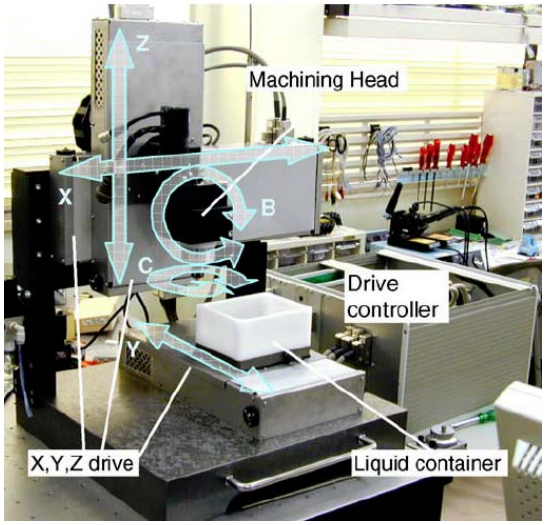

Figure 3.12 A desktop-size hybrid ECM set-up, reprinted from [34].

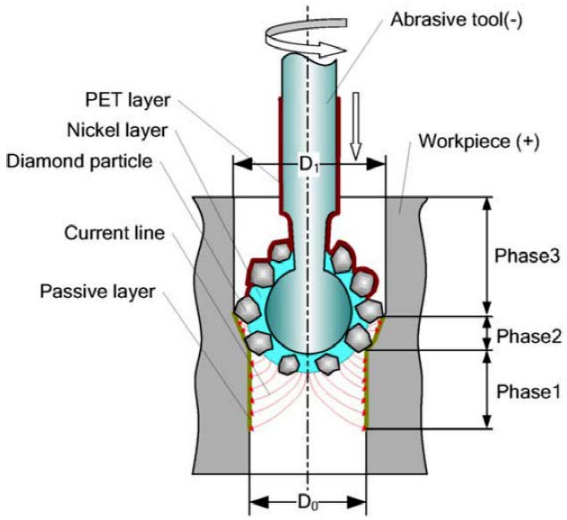

Figure 3.13 Schematic illustration of grinding and ECM hybrid system, reprinted from [35].

In laser assisted ECM, as shown in Figure 3.14, a laser beam was focused on an area exposed to the electrolyte jet, which dissolved a specific region and improved precision and surface roughness [36, 37]. Due to increased temperature in the region affected by the

laser beam, this process improved the volumetric MRR of 20%, 25%, 33%, and 54% for Hasteloy, titanium alloy, stainless steel and aluminum alloy, respectively.

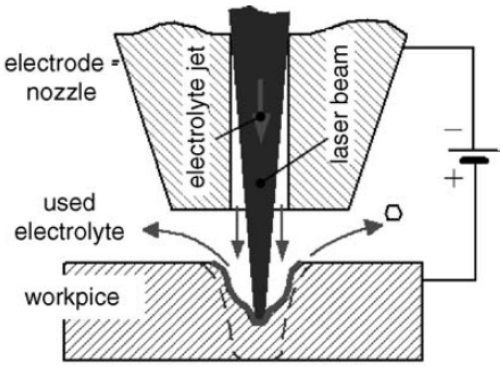

Figure 3.14 Schematic illustration laser assisted ECM, reprinted from [37].

A novel process for the ECM of metal using masking layer was proposed by Shin [38] and Qian [39]. In the masking step, a patterned layer on an anode surface was formed by laser marking or other masking techniques. This patterned surface was selectively dissolved during the ECM process because masked areas temporarily acted as an insulation layer, as shown in Figure 3.15. The anodic workpiece can only be machined at selected area. However, undercut was observed.

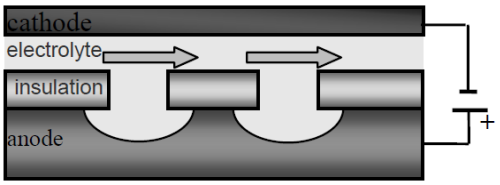

Figure 3.15 ECM with masking insulation layer, reprinted from [39].

Ultrasonic assisted ECM, involves vibrating either the tool electrode or electrolyte which agitates the abrasives suspended in the electrolyte for a good surface finish [40]. A study of the geometry and type of electrode which gave a well-polished surface (0.7 μm Ra) was reported and the effect of ultrasonic energy was acknowledged [41]. This energy was also responsible for the removal of debris from the machining zone and creation of optimal hydrodynamic conditions affecting the surface layers [42].

Hybridization ECM with low frequency tool vibration provides a positive and beneficial effect by changing the physical conditions in the inter-electrode gap. The variation of the gap pressure leads to the removal of the sludge products and allowed renewal of the electrolyte in the machining gap. The reciprocal motion between the tool and the workpiece surface enhanced the circulation of the electrolyte through the interface to permit the use of higher current densities in order to improve the quality of the resultant surface. In traditional vibration assisted ECM, anode/cathode vibrated in the vertical direction, the by-products precipitated at the bottom of machining zone due to gravity, which hindered the flushing away process. A horizontal vibration assisted ECM was proposed by Feng [1, 4, 5, 11, 40], workpiece vibrated in the horizontal direction instead of the vertical direction which facilitated the by-products flush away process.

3.3.2 Numerical Simulation of ECM

For ECM and its variant processes, it is essential to estimate the volume of anode material removal for a specific time increment. The MRR is a function of current density distribution in the IEG where varying electrical conductivity of the electrolyte exists.

Electrolyte velocity and pressure field in the IEG affect the gas bubble formation and temperature distribution, hence affect the properties of electrolyte properties and current density [43]. Therefore, numerical simulation model involves mass, momentum, heat, electric charge and energy balance equations [44, 45].

Due to the non-contact nature of the ECM process, it is crucial to develop a simulation model to predict the anodic profile. The first electrode shape change simulation model was based on analytical techniques. McGeough [3] solved the ECM tool design using the "sine rule". This rule can be used to obtain an approximate shape but it failed when the tools have sharp discontinuities due to the neglection of stray current effects and the assumption of parallel flux lines. Alder et al. [46] used an analytical direct computation for 2D ECM, represented the workpiece by Fourier's series. In addition, an experimental validation of the model was given. Prentice and Tobias [47] used the FEM for the 2D computation of the metal removal rate. Their model took the effects of simultaneous changes in the electrolyte flow speed and temperature rise into consideration. Another similar method also reported by Ali [48]. Marius et al. [49] proposed a general applicable numerical method for the simulation of 3D electrode shape changes obtained during the ECM processes based on the "marker" method. Kozak [50] reported a study of pulse electrochemical micromachining (PECMM) using ultrashort pulse for generating complex 3-D microstructures. The effect of unsteady phenomena in electrical double layer on final anode shape also included in this study. Numerical simulation of the ECM process included the temperature effects was studied in [44, 45] and the temperature distribution was found to have an influence on the shape of the anode. For better accuracy and

simplification of tool design, a small yet stable IEG (by reducing the nonuniformity of the electrolyte conductivity) was required. Commercial software package was also used to predict the final anode shape [51].

A review of mass transfer issues in the ECM with the problems associated with the ECM process was given by Volgin [52]. Numerical modeling of the ECM process considering the hydrodynamics involved in the process was studied by Minazetdinov [53, 54]. The final anode shapes resulting after the ECM using a triangular shaped cathode and curved surface were modeled in these studies.

A model was developed by Ma [55] to predict the variation of gap in the ECM process and the pulsed current was taken into account. The model was for a stationary electrode and rotating workpiece. In addition to predict the gap, the model also predicted the surface roughness value after the finishing process was completed.

Simulation of heat generation during the ECM process and its effective dissipation using electrolyte flow was studied by Kozak [56]. It was found that a hollow cathode and pulse voltages help in the effective control of the heat generation.

In addition to simulation methods, experiment techniques were also used to reveal the nature of the ECM process. To improve the MRR in the ECM, numerous techniques are proposed: changing high current/voltage, pulsed current/voltage, electrolyte flow rate, electrode feed rate, mechanical vibration either on the anodic workpiece or the cathodic electrode, ultrasonic vibration either on the cathodic electrode or electrolyte. The

following sections review the effect of these machining parameters on the ECM performances.

3.3.3 Effect of Voltage/Current

In subtractive processes, the productivity is measured quantitatively as the MRR. Common practice for the ECM is to measure the removed volume or weight loss within a specific time. Based on the Faraday's law for electrochemical reaction, the MRR for the ECM can be shown in Equation (3.6) [3]. This equation demonstrates that there is a linear relationship between the MRR and the applied voltage.

In Bhattacharyya's investigation [57], sets of experiments had been conducted to investigate the effect of the ECM process parameters, such as applied voltage, electrolyte concentration, pulse on time and frequency of power supply on the MRR. In this investigation, copper plate with 0.4 mm thickness anode, $\phi 200$ µm platinum wire cathode, 25 g/L sodium nitrite electrolyte and the power supply with 15 ms on-time and 5 ms off-time were used. As shown in Figure 3.16, the MRR increased from 0.5 mg/min to 2.6 mg/min when the applied voltage changed from 4 V to 10 V. There was a linear relationship between the applied voltage and the MRR, as shown in Figure 3.16.

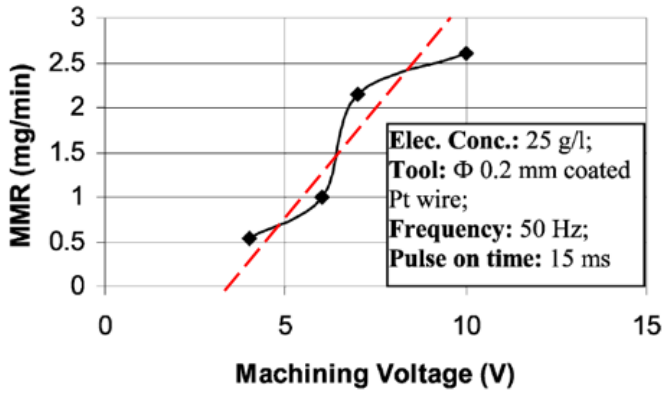

Figure 3.16 Variation of the MRR with machining voltage, reprinted from [57].

In another investigation carried out by Bhattacharyya [58], a ϕ16mm solid brass cathode, ϕ19 mm EN-8 steel anode and varied concentration NaCl solutions electrolyte were used. The experiment results indicated that for a preset electrolyte flow and concentration, the MRR increased with applied voltage at a quadratic manner for various IEG thicknesses. For a fixed electrolyte concentration and flow rate and for a constant IEG, the increase in applied voltage resulted in greater current available in the machining zone, hence causing the enhancement of MRR, as shown in Figure 3.17.

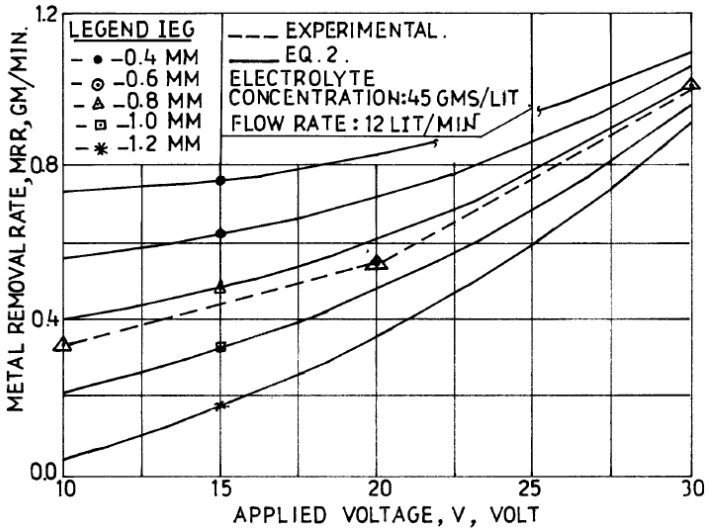

Figure 3.17 Effect of the applied voltage on the MRR for various IEG, reprinted from [58].

In Munda's investigation [12], a $\phi 335$ μm stainless steel wire with coating layer was chosen as the micro-tool, 0.15 mm thickness bare copper plate used as the anode and sodium nitrate was chosen as the electrolyte. The MRR increased with an increase of machining voltage for all levels of electrolyte concentration and for all levels of vibrations while other process parameters remain constant, as shown in Figure 3.18 and Figure 3.19.

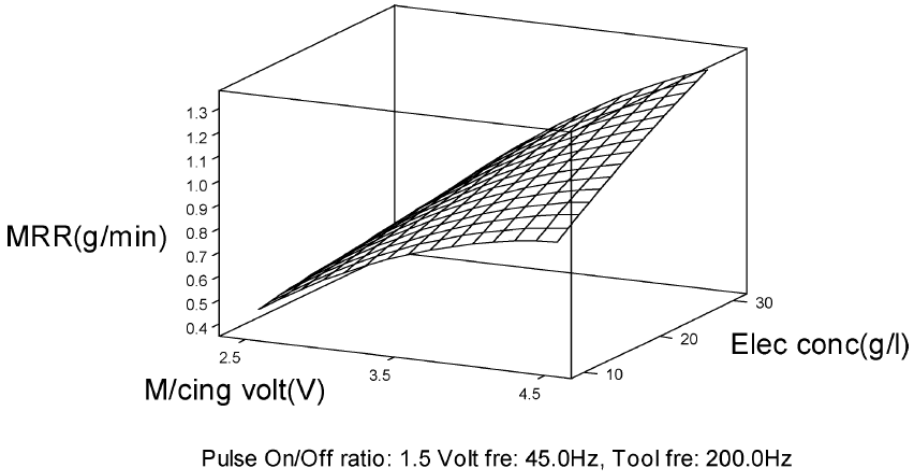

Figure 3.18 Influence of machining and electrolyte concentration on the MRR, reprinted from [12].

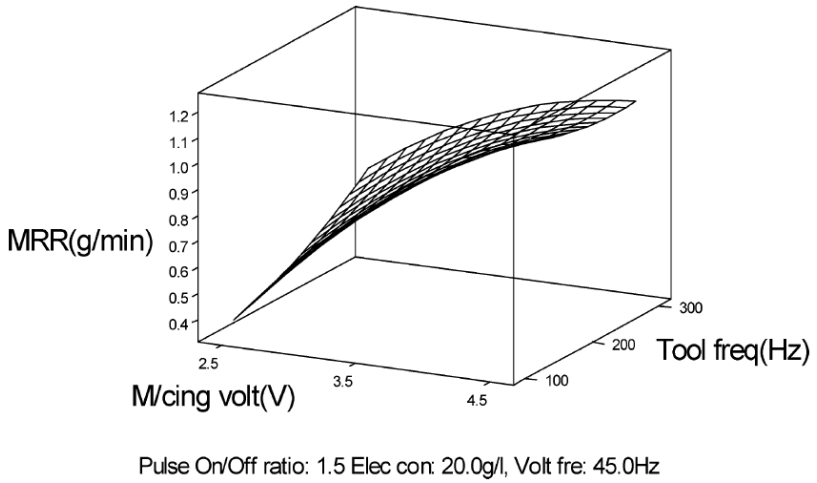

Figure 3.19 Influence of machining voltage and tool vibration frequency on the MRR, reprinted from [12].

Dhobe [59] investigated the relationship between the MRR and the applied voltage at different electrolyte flow speeds, as shown in Figure 3.20. In this investigation, $\phi 16mm$ copper cathode, $\phi\ 25\ mm\ \times\ 4\ mm$ titanium anode, 20 g/L NaBr electrolyte, 20, 22, 24, 26 V applied voltages and 13, 15, 17, 19 m/s electrolyte flow speeds were used.

Experiment results indicated that the maximum MRR of 116.732 mg/min was obtained at 17 m/s flow speed and 26 V applied voltage during the ECM process. The relationship between the MRR and the machining voltage was almost linear.

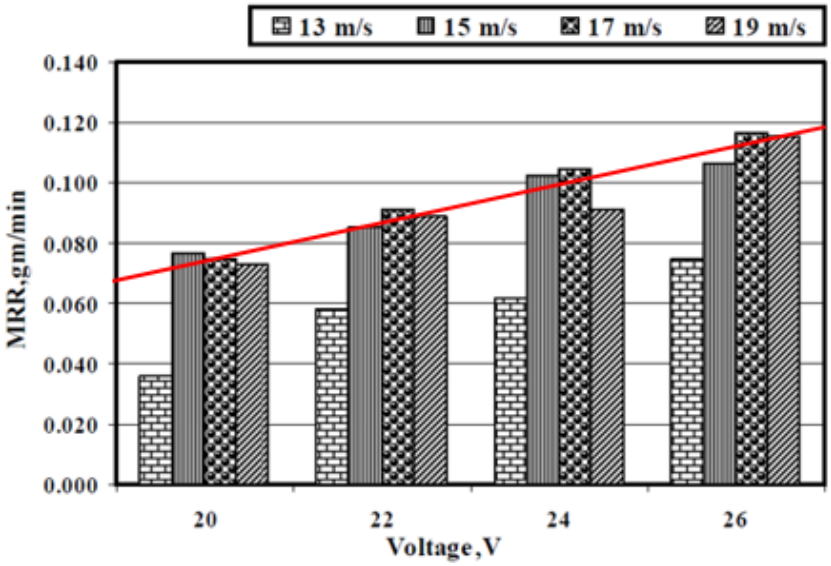

Figure 3.20 Histogram plot showing the effect of applied voltage on the MRR, reprinted from [59].

In Ayyappan's investigation [60], 5 g/L potassium dichromate ($K_2Cr_2O_7$) of water mixed with aqueous NaCl electrolyte, brass cathode, 8 L/min electrolyte flow rate and 0.1 mm/min cathodic electrode feed rate were used. At every level of the IEG and electrolyte concentration, the MRR increased with an applied voltage increase, as shown in Figure 3.21.

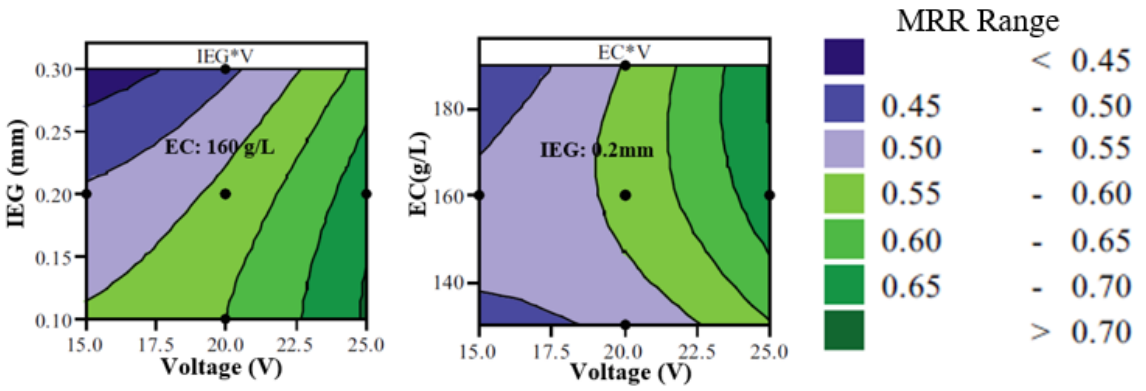

Figure 3.21 Parametric influence on the MRR, reprinted from [60].

In Senthilkumar's investigations [61-63], applied voltages ranged from 12-16V, the cathode was copper with square cross-section, the anodes were LM25Al/10%SiCp, Al/15% SiCp and Al/20%SiCp, the electrolyte was 20 g/L $NaNO_3$, the electrolyte flow rate was 7 L/min and the feed rates were 0.2, 0.4, 0.6, 0.8, 1 mm/min. As the applied voltage increased from 12 V to 16V, the MRR increased from 0.0514 g/min to 0.0634 g/min for LM25Al/10%SiCp (Figure 3.22), from 0.0227 g/min to 0.0462 g/min for Al/15% SiCp (Figure 3.23) and from 0.0112 g/min 0.0397 g/min for Al/20% SiCp (Figure 3.24), as shown in Figure 3.22 to Figure 3.24.

High applied voltage and current lead to an added MRR due to the following factors [61]:

i) Break down the passive films on active material surface.

ii) Facilitate the electrochemical reactions between the cathodic electrode and the anodic workpiece.

iii) Improve the migrating rate which also enhanced the MRR due to accelerating ion transport.

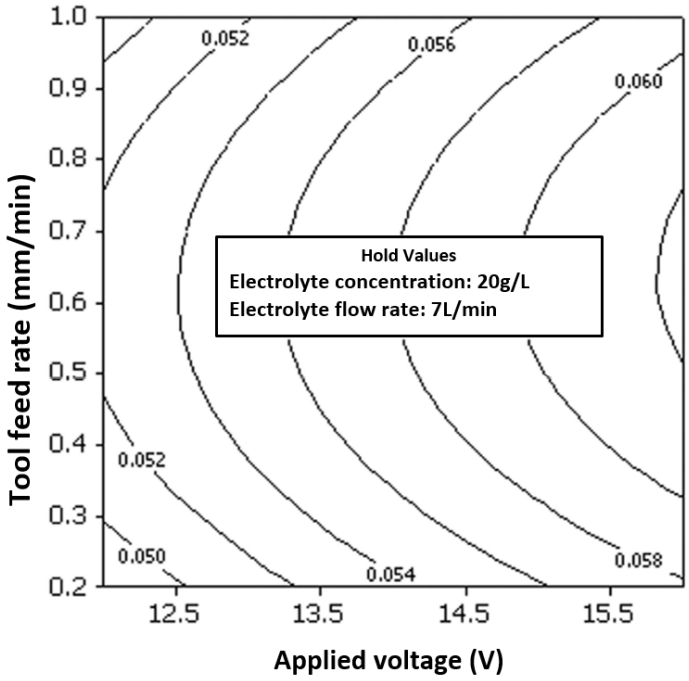

Figure 3.22 Influence of applied voltage on the MRR when machining LM25Al/10%SiCp, reprinted from [63].

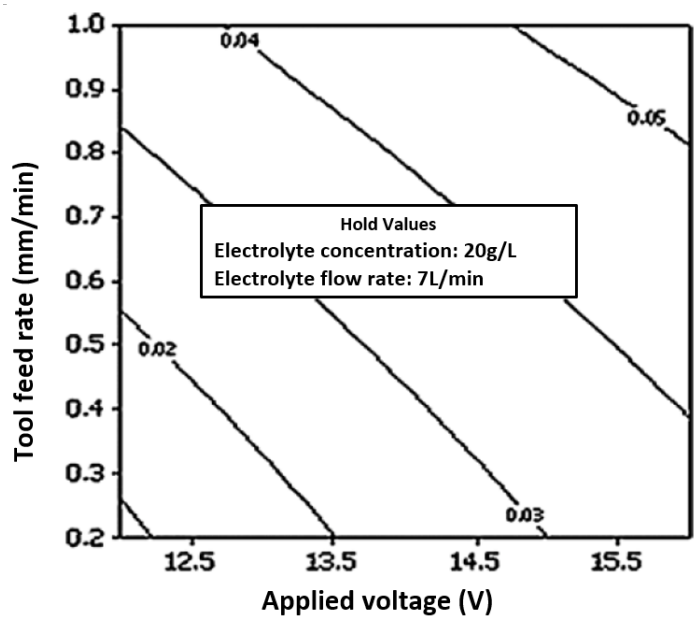

Figure 3.23 Influence of applied voltage on the MRR when machining Al/15% SiCp , reprinted from [62].

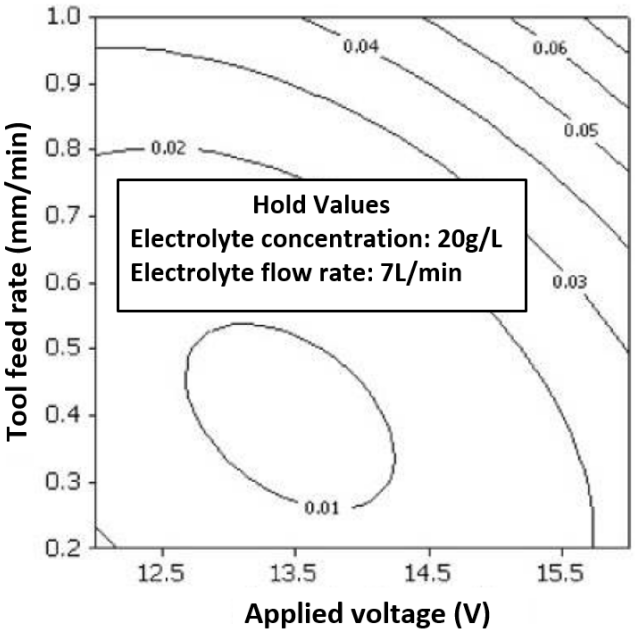

Figure 3.24 Influence of applied voltage on the MRR when machining Al/20% SiCp, reprinted from [61].

3.3.4 Effect of Pulsed Current

In the conventional ECM, a DC power was generally applied. The MRR increased with an increase of applied voltage/current. The electrolyte between the IEG was easily boiled due to energy dissipation of high current density, which resulted in a varying local distribution of electrolyte conductivity and hence led to poor machining accuracy [55]. In addition, a higher voltage/current also resulted in more undesired products and heat which required a higher electrolyte flow rate to be removed. An elaborate pumping system was needed to provide higher electrolyte flow rate, and a heavy machining frame was also required to maintain rigidity, which led to installing and operating costs increasing and presented a major limitation to the wide application of the ECM. Pulsed current (as shown

in Figure 3.25), instead of direct current, was applied in the ECM to enhance the process [8, 55]. In this figure, i_p is the peak current, i_a is the average current, t_{on} is the pulse on time, t_{off} is the pulse off time and $t_p = t_{on} + t_{off}$ is the pulse period time.

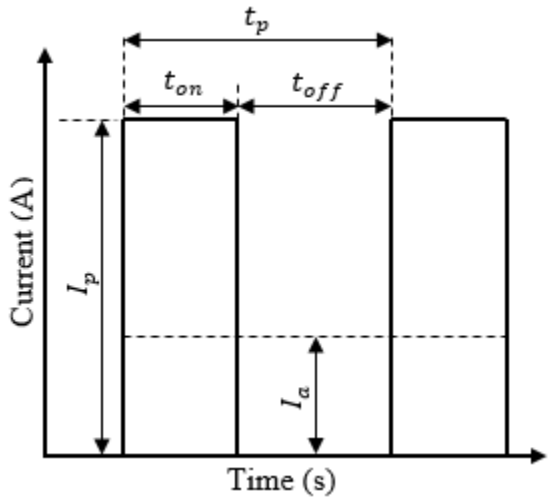

Figure 3.25 Schematic illustration of pulsed current

In principle, pulsed ECM (PECM) allowed one to apply a high instantaneous voltage/current without the need of high electrolyte flow rate since each current pulse was followed by an off-time such that the system relaxed between two consecutive pulses [6, 7]. The improved electrolyte flow condition in the IEG, enhanced localization of anodic dissolution [64] and small yet stable gaps [6, 65] benefits introduced by PECM led to higher machining accuracy [66], better process stability and suitability for control [8, 43, 67]. These technical advantages combined with the inherent benefits of the traditional ECM using DC (such as burr free, stress free, independent of workpiece hardness and no tool wear) made PECM effective and economical for machining high strength, heat-

resistant material into complex shapes, such as turbine blades of titanium alloys and nickel-based super alloys [9]. Hence, the usage of pulsed power generated a major breakthrough in improving the ECM process [8, 9, 55].

When applying pulsed voltage/current in the ECM, the combination of peak current, voltage frequency and duty cycle exerted influence on the MRR and the dimension accuracy.

An ECM study [11] was conducted using $\phi 9.5$ mm bare stainless steel cathodic electrodes, 60 mm × 50 mm × 6.3 mm 1018 steel workpiece, 1 mol/L KBr electrolyte, 13 A average current. When the current frequency increased from 0 to 60 Hz, the MRR increased slightly from 34.3 mm^3/min to 34.9 mm^3/min. When the current frequency increased to 100 Hz, the MRR increased to 36.4 mm^3/min, as shown in Figure 3.26.

Bhattacharyya studied the effect of pulse on time on the MRR and overcut using $\phi 200$ μm platinum wire cathodic electrode, 6 mm × 4 mm × 0.4 mm copper plate workpiece, 15 g/L $NaNO_3$ electrolyte, 10 V peak voltage and 50 Hz voltage frequency [57]. When the duty cycle increased from 25% to 75% (pulse on-time increased from 5 ms to 15 ms), the MRR increased from 0.2 mg/min to 1.2 mg/min but the overcut also increased from 0.04 mm to 0.07 mm [9], as shown in Figure 3.27. For a fixed voltage frequency, the MRR increased with an increase of pulse on time, since more time had been allowed to remove the anode material. In other words, average current density increased with an increase of pulse on time, which led to an increase of anode dissolution efficiency. The MRR increased rapidly at the range of pulse on time 5-10 ms due to rapid increment of

dissolution efficiency. Pulse on time further increased in the range of 10-15 ms, the MRR did not increase quickly due to dissolution efficiency reached its maximum value because the by-products were not flushed away from machining zone.

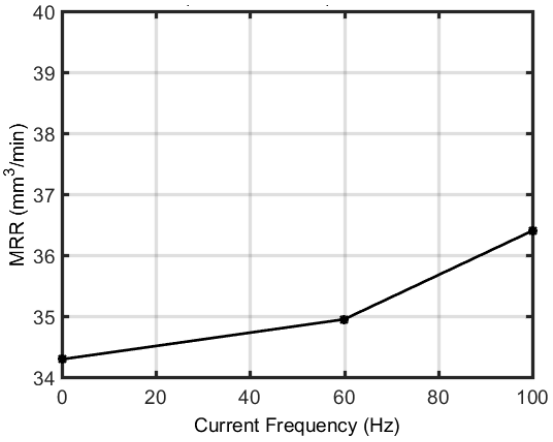

Figure 3.26 MMR for DC and pulsed DC current, reprinted from [11].

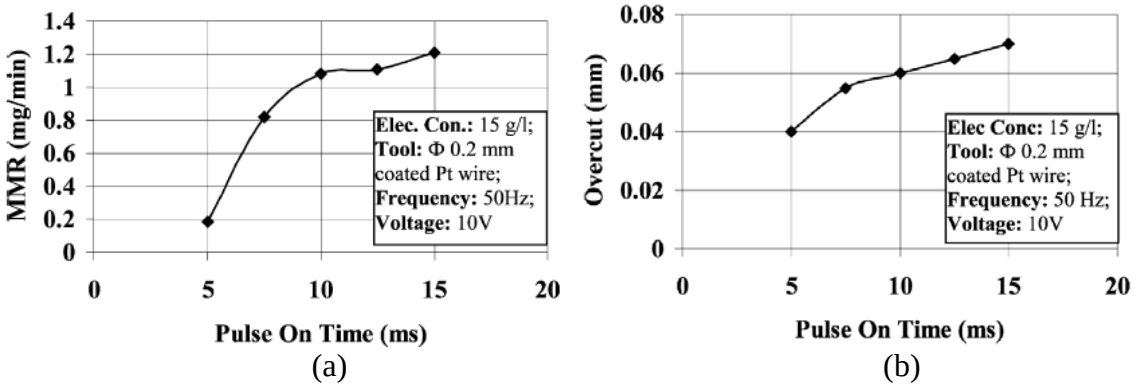

(a) (b)

Figure 3.27 Variation of the MRR and overcut with pulse on time, reprinted from [57].

Munda examined the effect of pulse on/off ratio on the MRR using $\phi 335$ μm stainless steel wire cathodic electrode with coating layer, 15 mm × 10 mm × 0.15 mm bare copper

plate workpiece, 20 g/L sodium nitrate electrolyte and 3.5V peak voltage [12, 14]. For a specific value voltage frequency, i.e. at 35 Hz, as shown in Figure 3.28, the MRR initially increased with an increase of duty cycle to the maximum value, but the MRR then decreased with further increasing in duty cycle at a preset machining parameter. The paper cited that the MRR increased with an increase of duty cycle due to more machining time. With further increased in duty cycle, the MRR decreased in small span of off time due to inefficient removing of the by-products from the machining zone that led to improper dissolution of workpiece material. In addition, radial over cut increased with increasing duty cycle. Since the by-products were inefficiently flushed away from machining zone during shorter off-time (i.e. higher duty cycle), the presence of the by-products microparticles between the anodic workpiece and the cathodic electrode would increase the chance of micro-sparking when high voltage applied and hence increased the radial over cut. Moreover, localization effect diminished with an increasing in duty cycle. For a specific duty cycle, i.e. 60%, when voltage frequency increased from 35 Hz to 55 Hz, the MRR increased from 821.948 mg/min to 919.980 mg/min and the radial overcut increased from 161.389 μm to 203.190 μm [10].

Pulsed ECM leads to a higher dimension accuracy, better surface quality, better process stability, and suitability to online process control. These benefits are obtainable due to several factors [67]:

i) Enhancing localized anodic dissolution,

ii) Improving electrolyte hydrodynamic uniformity in the IEG by removing the undesired by-products and reducing heat during off-time,

iii) Reducing and stabilizing IEG, and

iv) Reducing required electrolyte flow rate.

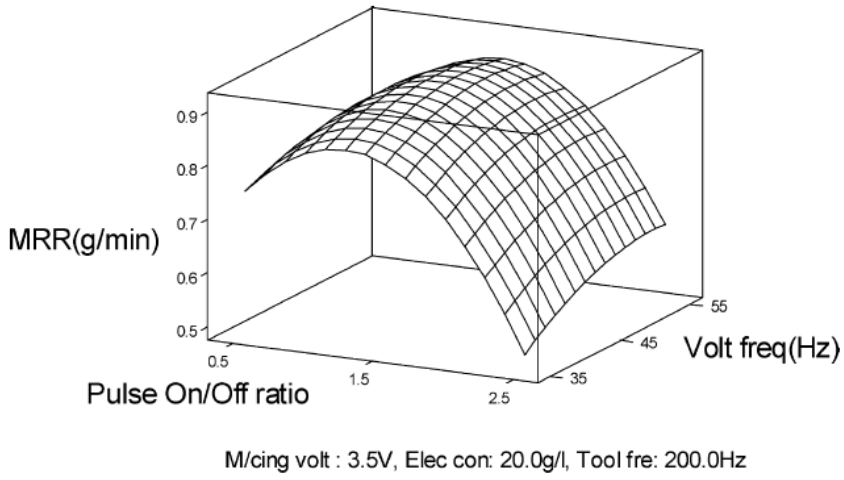

Figure 3.28 Influence of pulse on/off ratio and voltage frequency on the MRR, reprinted from [12].

3.3.5 Effect of Electrolyte Flow

Diffusion rate is another major factor that affects the ion transport and the MRR. Although an electrolyte can be static in theory, it is commonly pumped at high flow rate to flush away the by-products, reduce electrolyte temperature and replenish fresh electrolyte in the IEG.

An ECM with copper cathodic electrode with square cross section, $\phi 30 \times 6$ mm alloy steel workpiece, 20 g/L $NaNO_3$ electrolyte, 0.6 mm/min cathodic electrode feed rate and 14 V applied voltage was investigated [62]. When the flow rate increased from 5 L/min to

9 L/min, the MRR increased from 0.0242 g/min to 0.0478 g/min, and the surface roughness reduced from 3.241 µm to 2.785 µm.

Other authors [58] used ϕ16 mm solid brass cathodic electrode, ϕ19 mm EN-8 steel workpiece, 45 g/L NaCl electrolyte, 20 V applied voltage and 0.8 mm IEG. When the electrolyte flow rate increased from 10 L/min to 14 L/min, the MRR increased from 552.60 mg/min to 840.95 g/min and overcut reduced from 0.275 mm to 0.250 mm.

However, a high electrolyte flow rate requires an elaborate pumping system and a heavy machine frame to maintain rigidity. A very high flow rate may introduce two drawbacks:

i) Non-uniform electrolyte hydrodynamic condition in the IEG result in a poor machining dimensional accuracy.

ii) Cavitation results in poor surface quality.

3.3.6 Effect of cathodic electrode Feed Rate

Senthilkumar investigated the effect of feed rate on the MRR using a square cross-section copper cathodic electrode, 20 g/L $NaNO_3$ electrolyte, 14 V applied voltage, LM25Al/10%SiCp, Al/15% SiCp and Al/20%SiCp workpieces [61-63]. For LM25Al/10%SiCp workpiece, when the cathodic electrode feed rate increased from 0.2 mm/min to 1 mm/min, the MRR increased from 0.0101 g/min to 0.0464 g/min and surface roughness reduced from 10.814 µm to 8.217 µm, as shown in Figure 3.22. Similarly results also found for Al/15% SiCp and Al/20%SiCp. For Al/15% SiCp, when the cathodic electrode feed rate increased from 0.2 mm/min to 1 mm/min, the MRR increased from

0.0274 g/min to 0.0452 g/min and surface roughness reduced from 5.249 μm to 3.204 μm, as shown in Figure 3.23. For Al/20%SiCp, the MRR increased from increased from 0.0521 g/min to 0.0562 g/min and surface roughness reduced from 3.637 μm to 1.819 μm, as shown in Figure 3.24.

The author cited that the MRR was less at low tool feed rate. This was because current density in the IEG was low due to increasing gap size. A higher MRR achieved at high feed rate (0.8-1 mm/min). This was because an increase in the cathode feed rate increased the current density thus resulted in a higher MRR, as shown in previous Figures 3.22 - 3.24. However, there was an upper limit of feed rate. If the feed rate was larger than its upper limit, the cathodic electrode would contact the workpiece and sparks occurred in the ECM which damage both the cathodic electrode and electrical system. Thus, it is crucial to find the optimal value of feed rate at the preset machining parameters combination.

3.3.7 Effect of Cathodic Electrode Side-Insulation

A non-conductive layer was coated on the cathodic electrode circumference to increase current density in the frontal area and reduce the stray current, hence to increase the current density in the IEG. A proper coating must overcome technical challenges, such as chose the appropriate coating material that strongly adhered to the substrate, was nonconductive, robust, and uniformly thin with minimum porosity while had superior chemical and thermal resistance. A conductive ECM cathodic electrode had been successfully coated with polyethylene terephthalate (PET) powder by electrostatic spraying [68], synthetic

material [14], Parylene by vapor deposition polymerization under vacuum [69], epoxy resin [15], Teflon [11], and silicon nitride /silicon carbide [57].

To compare the effect of the cathodic electrode insulation layer on the MRR in the ECM, Feng [11] experimented with $\phi 9.5$ mm stainless steel cathodic electrode with Teflon coated on both outside and inside and another set without coating layer, 60 mm × 50 mm × 6.3 mm 1018 steel workpiece, 1 mol/L KBr electrolyte, 13 A average current. Compared with the uncoated cathodic electrode, using DC current (voltage frequency is zero), the The MRR increased from 34.3 mm^3/min to 35.4 mm^3/min when using coated cathodic electrode and other machining parameters remain constant. In addition, at 60 Hz voltage frequency, the MRR increased from 34.9 mm^3/min to 37.1 mm^3/min; at 100 Hz voltage frequency, the MRR increased from 36.4 mm^3/min to 39.8 mm^3/min, as shown in Figure 3.29.

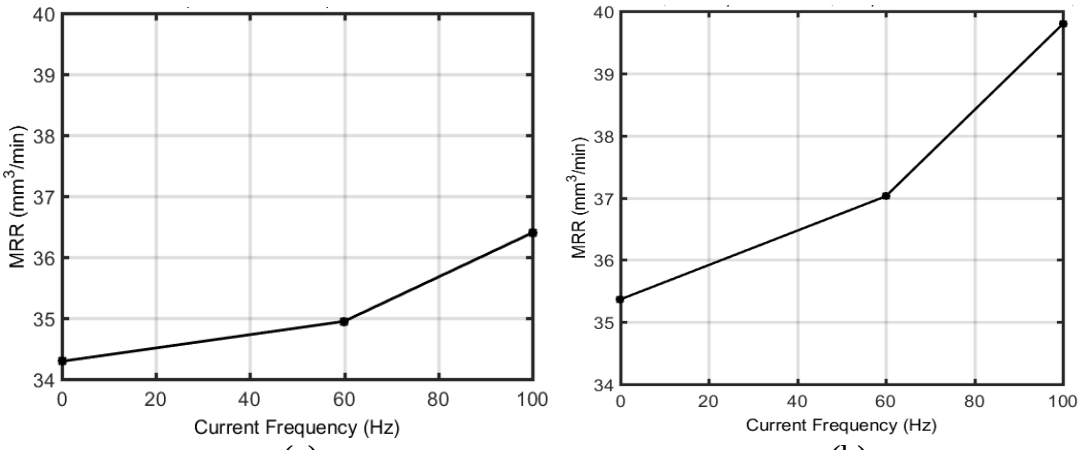

Figure 3.29 MRR using (a) uncoated cathodic electrode and (b) coated electrode, reprinted from [11].

3.3.8 Effect of Ultrasonic Vibration

Some researchers explored the effect of ultrasonic vibration on the ECM process. Ruszaj [70] used brass cathodic electrode, NC6 steel workpiece, 20-120 W ultrasonic vibration power with 10 μm maximum vibration amplitude at 20 kHz. They found a slight improvement in surface finish R_a from 1.5 μm to 1.0 μm, and concluded that specific ultrasonic amplitude for each combination of machining parameters would result in an optimal surface finish. Instead of applied ultrasonic vibration on the cathodic electrode or the anodic workpiece, some researchers set up an ECM cell in ultrasonic baths at either 20 kHz or 56 kHz [13]. The effect of ultrasonic waves was expected by the transmission of high frequency waves through the glass walls of the electrochemical cell. Using 10 A current and changing vibration frequencies from 0 to 20 kHz, the authors found the MRR increased slightly from 0.194 g/min to 0.197 g/min. When increasing vibration frequency to 50 kHz, the MRR increased to 0.207 g/min. The study concluded that insignificant improvement was due to the ineffective transmission of ultrasonic wave through glass wall into the IEG gap of the ECM cell.

Patel et al. [40] used ultrasonic probe to send 20 kHz ultrasonic wave to workpiece surface via flowing electrolyte. The authors used 60 mm × 50 mm × 6.3 mm 6061-T6 aluminum workpiece, Teflon coated stainless steel tubular cathodic electrode with ϕ9.5 mm outer diameter, and ϕ8.9 mm inner diameter, 1 mol/L KBr electrolyte, 22 A peak current. When applying 275 Hz current frequency and increasing ultrasonic amplitudes from 0 to 15 μm, the authors found improvement of surface roughness from 2.5 μm to 1.1 μm but at the

expense of MRR. They concluded that the generation and implosion of micro bubbles due to cavitation at the workpiece surface interfered with ionization mechanism at anode.

3.3.9 Effect of Mechanical Vibration

Convection is the most significant factor that affects ion transport mechanism. To improve the convection rate, researchers have attempted to vibration either the cathodic electrode or the anodic workpiece at varied vibration frequencies and amplitudes to enhance the process. Low-frequency vibration of either the anodic workpiece or the cathodic electrode cyclically alter the IEG to enhance flushing of debris while refreshing the anode surface with new electrolyte.

In the traditional vertical vibration assisted ECM, assuming perfect synchronization of pulsed current and mechanical vibration, a single vibration cycle can be divided into two individual movements. For example, a downward movement and an upward movement. The downward movement during the reciprocal motion cycle results in the minimum gap size, hence it reduces the resistance between the IEG, increases the current passing through the cathodic electrode, and removes more material on the anode. The upward movement during the reciprocal motion results in a maximum IEG, which enables enhanced flushing conditions, and hence, a better removal of the by-products as compared to the conditions at minimum gap size [71], as shown in Figure 3.30.

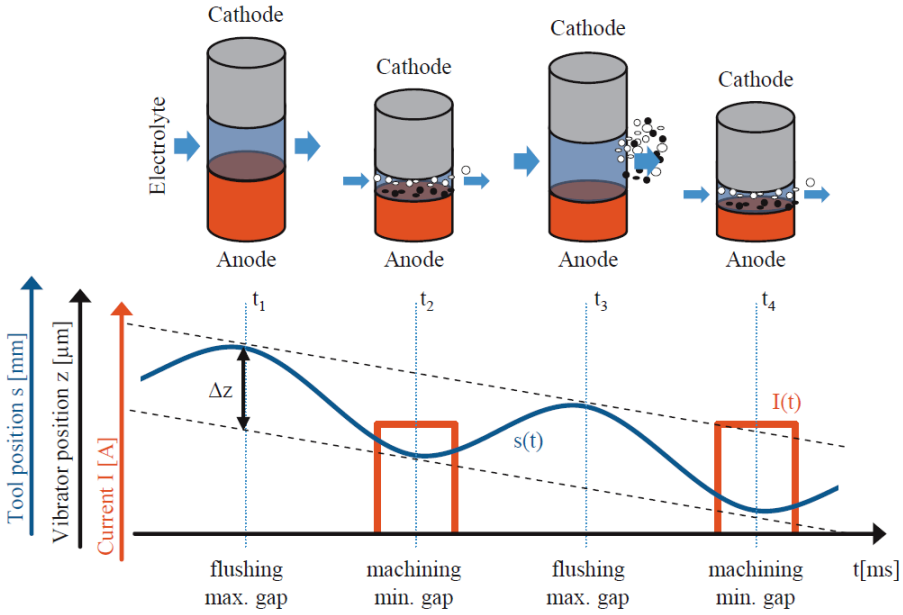

Figure 3.30 Schematic illustration of mechanical vibration in the ECM, reprinted from [71].

Ghoshal [72] pointed out that longitudinal vibration of vibration in the ECM enhanced the circulation of electrolyte. At the maximum IEG, as shown in Figure 3.31(a), the decreased pressure in the IEG generated transient cavitation or micro bubbles of electrolyte vapor. During the next half vibration cycle, the tool moved towards to the workpiece. While in the minimum IEG, as shown in Figure 3.31(b), pressure inside the IEG increased and micro bubbles collapsed rapidly. This phenomenon generated electrolyte turbulence, which drove out the by-products from the machining zone. A fresh electrolyte was forced in the IEG when tool moved away from the workpiece in the next oscillate cycle. Consequently, diffusivity and convective mass transport was enhanced inside the IEG, which played an important role in the case of high aspect ratio machining since it lacked fresh electrolyte at high depth and challenge in removal of the reaction by-products in the

extremely small gap. Figure 3.31(c) illustrated the relationship of displacement-time and velocity-time of tool during vibration. Kept vibration frequency constant and increased vibration amplitude led to tool velocity increased since the cycle time remained the same, which resulted in more energetic bubble collapsed, enhanced mass transport rate and improved diffusivity.

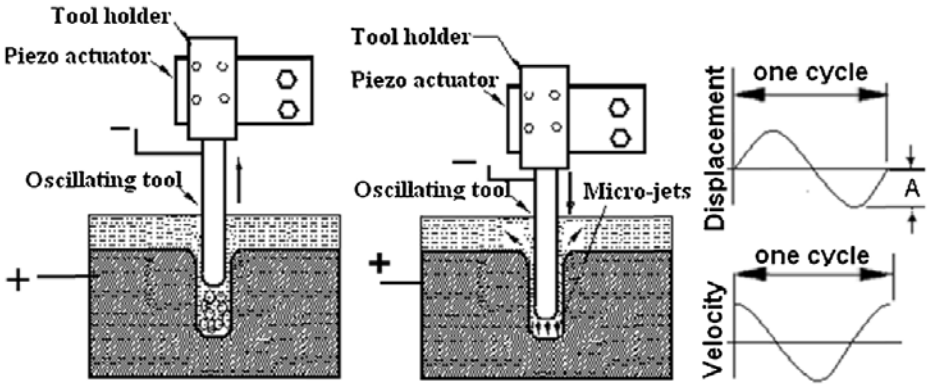

(a) Tool in up position (b) Tool in down position (c) Displacement versus time

Figure 3.31 Formation and collapse of bubbles during oscillating motion of tool, reprinted from [72].

Ebeid investigated the effect of vibration amplitude on machining performances using brass tube cathodic electrode with ϕ8 mm outer diameter and ϕ3.5 mm inner diameter, 20 g/L NaCl electrolyte, 6 L/min electrolyte flow rate, 1 mm/min cathodic electrode feed rate, 18 V applied voltage and 50 Hz vibration frequency [15]. The cathodic electrode was externally insulated with a thin layer using epoxy resin to avoid undesired side cutting. Experimental results illustrated that significant effects of the tool vibration amplitude on the overcut value was pronounced at the lowest tool amplitude values (20 µm peak-to-

peak). The value of the overcut decreased with a ratio of 15% at tool amplitude of 20 μm (peak-to-peak) more than that with zero tool amplitude. The phenomenon was resulted from a higher tool amplitude value which caused a greater stray current during the tool motion, which led to an increase of MRR on the side of workpiece. Conicity, defined as:

$$\delta_c = \frac{D_1 - D_2}{2H} \times 100 \tag{3.23}$$

where

δ_c: Conicity (%)

D_1: Hole diameter at level 1 (mm)

D_2: Hole diameter at level 2 (mm)

H: Height between the two levels (mm)

The conicity decreased with increasing vibration amplitude at every level of the cathodic electrode feed rate, as shown in Figure 3.32. The application of low-frequency vibration to the ECM tool reduced workpiece conicity with a ratio about 23% lower than that without vibration. This effect was due to the success of the pumping action at the frontal zone, intense flushing of the IEG with fresh electrolyte and evacuation of the by-products, which resulted in the decrease of lateral material removal and conicity improvement.

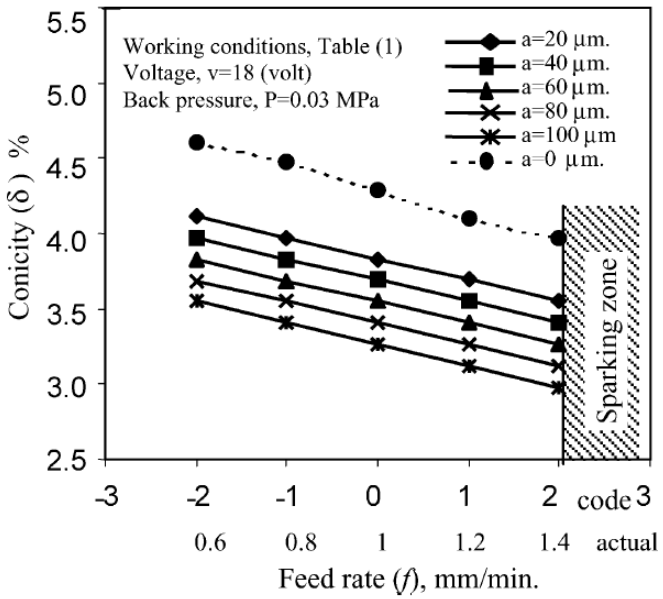

Figure 3.32 Effect of feed rate on conicity at various amplitude, reprinted from [15].

Liu [69] investigated the effects of vibration frequency and vibration amplitude on the MRR with $\phi 160$ µm tungsten cathodic electrode with 5 µm insulate layer, 321 stainless steel workpiece with 0.5 mm thickness, 5 wt% $NaNO_3$ + 0.8 wt% EDTA-Na_2 electrolyte, 6 V voltage with 50% duty cycle, 2 KHz pulsed voltage and 15.6 µm IEG, 3-14 µm vibration amplitude, and 50-200 Hz vibration frequency. The author applied low frequency vibration on the anodic workpiece instead of the cathodic electrode, and pointed out that a low frequency vibration would help the overall process efficiency by:

i) Ejecting the by-products away from the electrode faces, and

ii) Maintaining a stable electrolyte field within the IEG, therefore enhancing the MRR.

As shown in Figure 3.33, at a low vibration frequency of 50 Hz, the MRR increased about 5 times to 0.0388 mg/min (when vibration at 12 μm amplitude) from 0.0062 mg/min (without vibration). A peak value of MRR existed at certain amplitude for each vibration frequency, i.e., at 50 Hz, 12 μm vibration amplitude generated the maximum MRR. On the contrary, at higher vibration frequency of 200 Hz, the vibration amplitude had negligible influence on the MRR: 0.0066 mg/min at 8 μm vibration amplitude, compared with 0.0062 mg/min without vibration. At constant vibration amplitude, as shown in Figure 3.34, the MRR initially increased then decreased with increasing vibration frequency. For a preset vibration amplitude (4 μm, 6 μm and 8 μm), the resulted MRR initially increased with increasing of vibration frequency, but after obtaining the maximum MRR at 50 Hz, then the MRR decreased with increasing of vibration frequency.

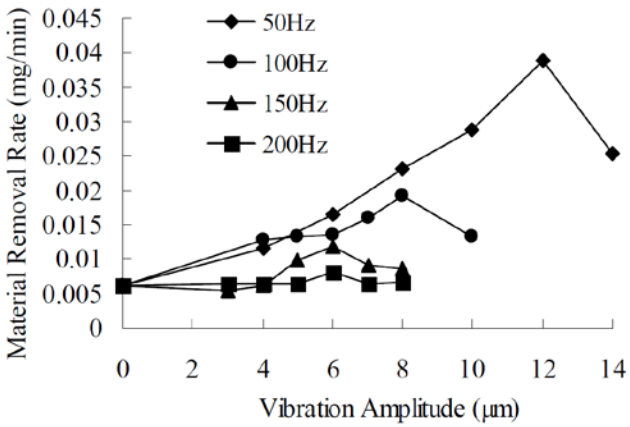

Figure 3.33 Effect of vibration amplitude on the MRR, reprinted from [69].

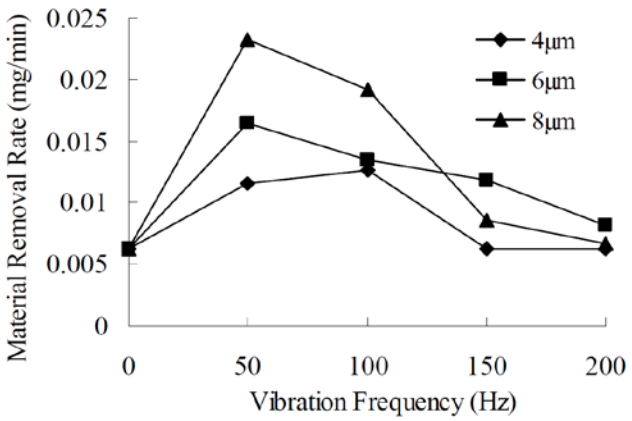

Figure 3.34 Effect of vibration frequency on the MRR, reprinted from [69].

Munda studied the effect of tool frequency on the MRR with ϕ335μm stainless steel wire cathodic electrode with coating layer, 15 mm × 10 mm × 0.15 mm bare copper plate workpiece, 20 g/L sodium nitrate electrolyte and 3.5V peak voltage with 45 Hz voltage frequency and 60% duty cycle [12, 14]. The influence of vibration frequency on the MRR was shown in previous Figure 3.19, keeping the other machining parameters constant, the MRR increased with an increase of vibration frequency. The author cited that vibration cycle help flushing away the sludge material from machining zone. At lower tool vibration frequency, the amount of flushing away sludge materials were fewer, which caused improper dissolution of anode material and led to a low MRR. When the tool vibration frequency increased, the MRR increased due to proper dissolution of anode material and greater amount of sludge material were flushed away from the IEG.

Effect of large range vibration frequency was also studied by Bhattacharyya [21]. The author used stainless steel cathodic electrode, 15 mm ×10 mm × 0.15 mm bare copper plate workpiece, varied concentration of sodium nitrate electrolyte (15 g/L, 20 g/L and 25

g/L), 3 V voltage, 55 Hz voltage frequency, 33% duty cycle and 0.144 mm/min cathodic electrode feed rate. A wide range of frequency from 50-23,000 Hz was selected for cathodic electrode vibration. Vibration amplitudes were 4.5 V-RMS an 8 V-RMS. Experimental results showed that the cathodic electrode vibration at kHz ranges had no significant influence on the MRR (~0.6 mg/min for 15 g/L electrolyte concentration and ~1.1 mg/min for 20 g/L electrolyte concentration), as shown in Figure 3.35. However, at lower ranges of cathodic electrode vibration, a higher MRR (~0.8 mg/min for 15 g/L electrolyte concentration and ~1.75 mg/min for 20 g/L electrolyte concentration) were obtained, as shown in Figure 3.36. The enhanced MRR and dimension accuracy attributed to the introduction of the cathodic electrode tool vibration in Hz range during the ECM process which eliminated the passive layer from the effective machining area of workpiece surface, and thereby improved the ECM actions.

To continue improve the MRR in the vibration-assisted ECM, synchronization of mechanical vibration with pulsed current was introduced. During this process, the cathodic electrode feeding toward the anode was overlaid with cathode vibration, which resulted in two different process phases (refer to Figure 3.30). During minimize gaps size, a pulse current with a pulse duration applied. The resistance between the IEG would decreased due to the tool vibration, which led to more efficient material dissolution. The maximum gap size achieved when the cathodic electrode moved away from the anodic workpiece, which improved the flushing conditions and hence a better removal of the by-products as compared to the minimum gap size condition [71].

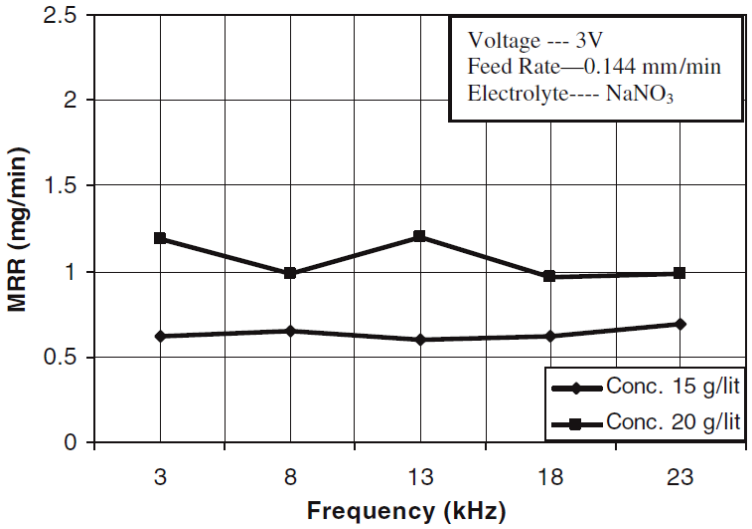

Figure 3.35 Influence of high tool vibration on the MRR, reprinted from [21].

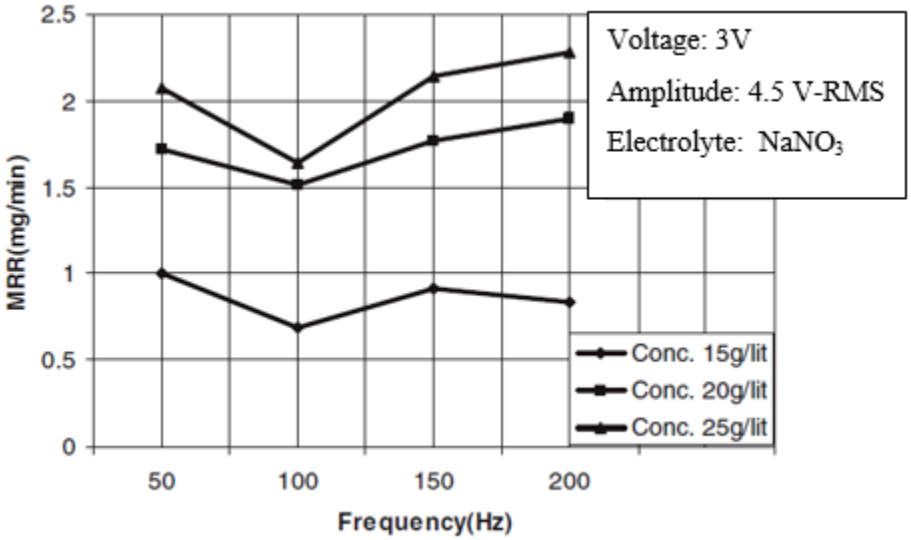

Figure 3.36 Influence of tool vibration frequency on the MRR at different electrolyte concentration, reprinted from [21].

Liu [73] introduced a tool electrode jump motion in the ECM, as shown in Figure 3.37. The author used 0.05 mm thickness stainless steel (1Cr/18Ni/9Ti) workpiece, ϕ145 μm and ϕ340 tungsten shaft cathodic electrode, H_2SO_4 electrolyte, 0.78 μm/s cathodic

electrode feed rate, 4.5 V applied voltage and 10.16 μm IEG. As shown in Figure 3.38, the tool jump height kept at 4 mm, the average machining side gap decreased as the tool jump acceleration increased. The reason can be attributed by the pumping force caused by the toll jump acceleration. Higher jump acceleration would cause higher pumping force to pull electrolyte outwards the IEG. Hence, the refreshing volume of electrolyte was increased as tool jump acceleration increased in each cycle. The consequence of that was improved machining accuracy. In addition, as shown in Figure 3.39, average machining gap also decreased as the tool jump height increased while kept the tool jump acceleration as 3.5 m/s^2. It was because that pumping time during the tool jump up period. Refer to the tool jump speed mode shown in Figure 3.37, the pumping time on the electrolyte was prolonged when tool jump height was extended. The benefit of this was more volume refreshed electrolyte and improved process precision.

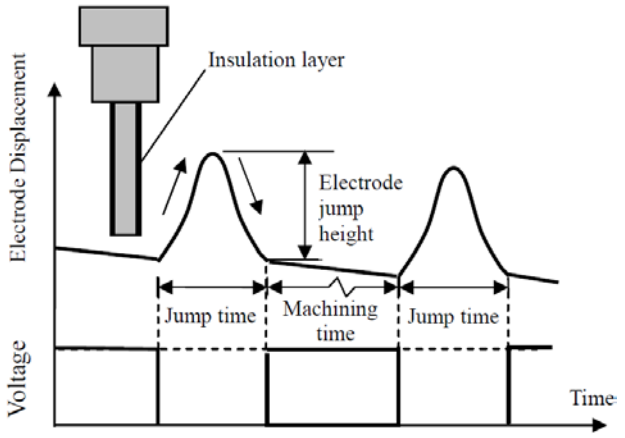

Figure 3.37 Schematic of ECM with tool electrode jump motion, reprinted from [73].

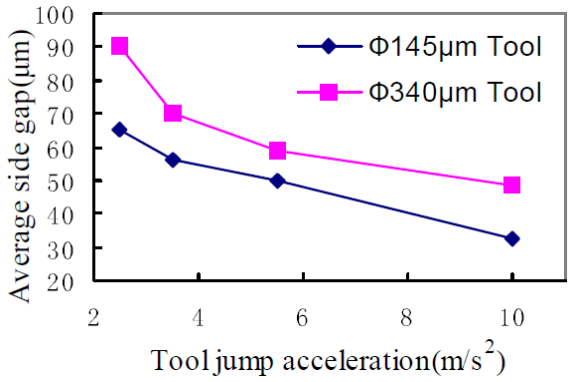

Figure 3.38 Effect of tool jump acceleration on machining side gap, reprinted from [73].

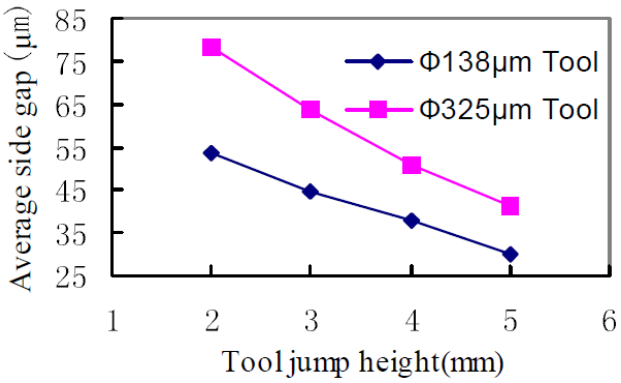

Figure 3.39 Effect of jump height on machining side gap, reprinted from [73].

4 THEORY

The machining speed of PECM with the boundary condition of electrolyte boiling is developed in this section. In the traditional direct current ECM, the electrolyte between the IEG is easily boiled due to the energy dissipation of high current density, which results in a varying electrolyte conductivity and hence leads to a poor dimension accuracy [55]. Pulsed current (as shown in previous Figure 3.25), instead of direct current, has been applied in the ECM to achieve the goal of better machining accuracy [8, 55], since it helps to i) maintain a smaller yet stable IEG size and ii) improve the flushing condition in the IEG due to the beneficial off-time during machining process to flushing away any by-products that were produced during on-time pulse.

A theoretical flushing speed of the by-products between the IEG is also developed for the vibration assisted ECM in this section. The removed materials, must be removed from the IEG by electrolyte flow since they will precipitate on anode surface and hinder further chemical reactions. To improve the flushing conditions, mechanical vibration is usually incorporated in the ECM to improve the by-products' flushing speed since it alters the distance between the anodic workpiece and the cathodic electrode.

4.1 Pulsed Current ECM

In principal, either current or voltage pulse waveform of any shape can be applied across the anodic workpiece and the cathodic electrode. For simplicity, this discussion will be restricted to rectangular constant current pulses separated by intervals of zero current (see

previous Figure 3.25). The ratio t_{on}/t_p is called the duty cycle. PECM then takes place at an average current given by

$$i_a = i_p\left(t_{on}/t_p\right) \tag{4.1}$$

A small gap is essential for better ECM machining accuracy. However, Joule heat increases significantly when a small gap is used since the current passing between the IEG is inversely proportional to the gap size in the ECM. The resulting electrolyte boiling introduces local variation distribution of electrolyte conductivity and process stability.

Consider two parallel plane electrodes with rectangular pulsed voltage applied across them, as shown in Figure 4.1. Voltage pulse off-time is long enough to ensure a complete flushing of the electrolyte in the gap. Under this condition, pulse off-time t_{off} is larger than L/V_e (where L is the gap distance in the electrolyte flow direction and V_e is the average electrolyte flow speed). Thus, the analysis of the process for a single pulse is valid for a series of pulses.

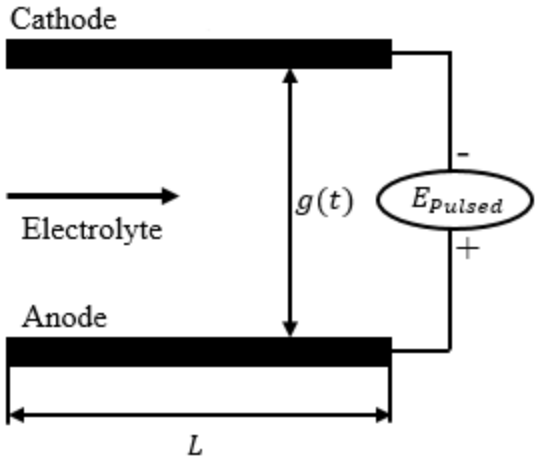

Figure 4.1 Schematic illustration of PECM.

Additional assumptions are made for the model to simplify the analysis which include [9]:

i) No heat transfers through the electrodes into or out of the IEG region.

ii) The temperature in the IEG is constant and equals the temperature averaged over the cross-section.

iii) Current efficiency of the anodic dissolution is constant during pulse on-time.

iv) Neglect the gas generation.

Define:

C_p Specific heat of electrolyte (J/kg/°C)

f_e Cathodic electrode feed rate (μm/s)

g Inter-electrode gap (μm)

J Current density (A/mm^2)

K_v $= \frac{M}{z\rho_a F}$ is the effective volumetric electrochemical equivalent (mm^3/A/s)

T_{boil}	Boiling temperature of the Electrolyte (℃)
T_0	Initial temperature of electrolyte (℃)
U_0	Amplitude of voltage pulse (V)
ΔU	Overpotential (V)
α_T	Temperature coefficient of the conductivity at T_0
θ	Average temperature increment is $T - T_0$ (℃)
θ_{boil}	Temperature increment from T_0 to T_{boil} (℃)
κ_0	Electrolyte conductivity at T_0 (S/mm)
ρ_e	Electrolyte density (g/mm^3)

Under these assumptions, the variation of electrolyte properties is dominated by Joule heating. According to the Bruggeman equation, the electrolyte conductivity κ_e can be expressed as [74]:

$$\kappa_e = \kappa_0(1 + \alpha_T\theta) \tag{4.2}$$

Based on the Faraday's law, the MRR during the pulse on-time t_{on} is:

$$\frac{dg}{dt} = K_v \cdot J = \frac{M}{z\rho_a F} \cdot J \tag{4.3}$$

The current density, J, can be expressed by Ohm's law:

$$J = \frac{I}{A} = \frac{U_0 - \Delta U}{RA} = \frac{U_0 - \Delta U}{\frac{g}{\kappa_e A} A} = \frac{\kappa_e (U_0 - \Delta U)}{g}$$

$$= \kappa_0 (1 + \alpha_T \theta) \frac{U_0 - \Delta U}{g} \tag{4.4}$$

In an ECM system, the heat generation rate per unit area JU_0 is equal to the sum of the electrolyte internal energy changing rate and the heat convection [9], that is,

$$Internal\ Energy + Heat\ convection = Heat\ generation \tag{4.5}$$

Substituting the respective terms to get:

$$\frac{\partial(\rho_e C_p g \cdot \theta)}{\partial t} + \frac{\partial(\rho_e C_p V_e \theta \cdot g)}{\partial x} = JU_0 \tag{4.6}$$

The convection term in this equation, $\frac{\partial(\rho_e C_p V_e \theta \cdot g)}{\partial x}$, can be neglected for the PECM with a short on-time pulse t_{on}. Neglecting the convection term also implies that, in this particular case, g and θ are dependent only on time. Therefore, Equation (4.6) becomes:

$$\frac{d(g\theta)}{dt} = \frac{JU_0}{\rho_e C_p} \tag{4.7}$$

Then, Equation (4.7) can be written as:

$$\frac{d(g\theta)}{dt} = g\frac{d\theta}{dt} + \theta\frac{dg}{dt} = \frac{JU_0}{\rho_e C_p} \tag{4.8}$$

By combining Equations (4.3) and (4.8) , the following equation is obtained:

$$g\frac{d\theta}{dt} = \frac{JU_0}{\rho_e C_p}\left(1 - \frac{K_v \rho_e C_p \theta}{U_0}\right) \tag{4.9}$$

In this investigation, the voltage pulse amplitude U_0 is 26V, the density of an electrolyte (1mol /L KBr) is 1070 kg/m^3, and the specific heat capacity of solution, C_p, is proximately equal to that of water, 4200 J/kg/°C. Thus:

$$\rho_e C_p = 1070\ kg/m^3 \times 4200\ J/kg/℃ = 4.5 \times 10^6 J/m^3 \cdot K \tag{4.10}$$

θ is the average temperature increment and is equal to $T - T_0$ (℃), and $T \leq T_{boil} = 100℃$, then:

$$\theta < 80℃ \tag{4.11}$$

K_v is the effective volumetric electrochemical equivalent. For the 1018 steel that is used in this study [11]:

$$K_v = 3.7 \times 10^{-11} m^3/A/s \tag{4.12}$$

Thus, the term $1 - \frac{K_v \rho_e C_p \theta}{U_0}$ in Equation (4.9) is:

$$1 - \frac{K_v \rho_e C_p \theta}{U_0} = 1 - \frac{3.7 \times 10^{-11} \times 4.5 \times 10^6 \times 80}{26} = 0.9994 \approx 1 \tag{4.13}$$

Therefore, Equation (4.9) becomes:

$$g\frac{d\theta}{dt} = \frac{JU_0}{\rho_e C_p} \tag{4.14}$$

Substituting Equation (4.4) into Equation (4.14), then Equation (4.15) can thus be established for describing the PECM process without electrolyte boiling:

$$\frac{d\theta}{dt} = J\frac{U_0}{g\rho_e C_p} = \kappa_0(1+\alpha_T\theta)\frac{U_0-\Delta U}{g}\frac{U_0}{g\rho_e C_p}$$
$$= \kappa_0(1+\alpha_T\theta)\frac{U_0(U_0-\Delta U)}{g^2\rho_e C_p} \tag{4.15}$$

Equation (4.15) can be written as:

$$\frac{d\theta}{dt} - M'\alpha_T\theta = M' \tag{4.16}$$

where

$$M' = \kappa_0\frac{U_0(U_0-\Delta U)}{{g_0}^2\rho_e C_p} \tag{4.17}$$

Equation (4.16) is the first order differentiation equation with constant coefficient M', its general solution follows:

$$\theta(t) = C\exp\left(-\int_0^t -M'\alpha_T\,dt\right) + \exp\left(-\int_0^t -M'\alpha_T\,dt\right)$$
$$\times\int_0^t M'\exp\left(\int_0^t -M'\alpha_T\,dt\right)dt \tag{4.18}$$

Then,

$$\theta(t) = C\exp(M'\alpha_T t) + \exp(M'\alpha_T t) \times \int_0^t M'\exp(-M'\alpha_T t)dt$$

$$= C\exp(M'\alpha_T t) - \frac{1}{\alpha_T}\exp(M'\alpha_T t)\int_0^t \exp(-M'\alpha_T t)\, d(-M'\alpha_T t)$$

$$= C\exp(M'\alpha_T t) - \frac{1}{\alpha_T}\exp(M'\alpha_T t)\exp(-M'\alpha_T t)$$

$$= C\exp(M'\alpha_T t) - \frac{1}{\alpha_T} \tag{4.19}$$

with initial condition $\theta = 0$ at $t = 0$, then $C = 1/\alpha_T$. The temperature increment θ is obtained as：

$$\theta = \frac{1}{\alpha_T}\exp(M'\alpha_T t) - \frac{1}{\alpha_T} = \frac{1}{\alpha_T}\left[\exp\left(\alpha_T \frac{U_0(U_0 - \Delta U)\kappa_0}{g_0^2 \rho_e C_p} t\right) - 1\right] \tag{4.20}$$

When electrolyte boiling is considered as the limit for maintaining a stable small gap, this minimum gap size, denoted as S_*：

$$\theta_{boil} = \frac{1}{\alpha_T}\left[\exp\left(\alpha_T \frac{U_0(U_0 - \Delta U)\kappa_0}{{S_*}^2 \rho_e C_p} t_{on}\right) - 1\right] \tag{4.21}$$

Equation (4.21) can be rearranged to be:

$$\exp\left(\alpha_T \frac{U_0(U_0 - \Delta U)\kappa_0}{{S_*}^2 \rho_e C_p} t_{on}\right) = 1 + \alpha_T \theta_{boil} \tag{4.22}$$

Solve for S_*:

$$\frac{1}{{S_*}^2} = \frac{\rho_e C_p}{\alpha_T U_0 (U_0 - \Delta U)\kappa_0 t_{on}} \ln(1 + \alpha_T \theta_{boil}) \tag{4.23}$$

$$S_* = \sqrt{\frac{\alpha_T \kappa_0 U_0 (U_0 - \Delta U)}{\rho_e C_p \ln(1 + \alpha_T \theta_{boil})} t_{on}} \tag{4.24}$$

Thus, to obtain a small yet stable gap size in the PECM, a short on-time pulse (high voltage frequency) should be selected. For the minimum gap size S_*, combining with Equations (4.3) and (4.4) to obtain：

$$\frac{dg}{dt} = K_v J = \frac{M}{zF\rho_a} \frac{\kappa_0 (1 + \alpha_T \theta)(U_0 - \Delta U)}{g} \tag{4.25}$$

where $g = S_*$, then:

$$\frac{dg}{dt} = \frac{M}{zF\rho_a} \frac{\kappa_0 (1 + \alpha_T \theta)(U_0 - \Delta U)}{\sqrt{\frac{\alpha_T \kappa_0 U_0 (U_0 - \Delta U)}{\rho_e C_p \ln(1 + \alpha_T \theta_{boil})} t_{on}}} \tag{4.26}$$

Therefore, to achieve a larger machining speed, $\frac{dg}{dt}$, a smaller pulse on time t_{on} should be chosen. However, the electrolyte volume between two electrodes acts as a R-C (resistor and capacitor) circuit in reality, the term t_{on} cannot approaches to 0 due to the charging time. Therefore, the term dg/dt cannot approach to infinite.

4.2 Vibration Assisted PECM

4.2.1 Basic Fluid Dynamics for Incompressible Flow

Define:

$A(t), A'(t)$	Workpiece vibration travel distance (μm)
A_v	Anodic workpiece vibration amplitude (μm)
C_1, C_2, C'_1, C'_2	Coefficients
f	Vibration frequency (Hz)
F_x, F_y, F_z	Body force along the x, y, z direction respectively (N)
g_0, g'_0	Inter-electrode gap at time $t = 0$ (μm)
p	Pressure (Pa)
Re	Reynold Number
t, t'	Machining time (s)
u, v, w	Electrolyte flow speed at x, y, z direction respectively (m/s)
u', v', w'	Electrolyte flow speed at x', y', z' direction respectively (m/s)
V_F	Electrolyte flow speed (m/s)
V_p, V'_p	Average particle flow speed (m/s)
x_p, x'_p	Particle center location (μm)
ν:	Electrolyte kinematic viscosity (m^2/s) = 1×10^{-6} m^2/s
ρ_e	Electrolyte density (g/mm^3)

The governing equations of motion for incompressible flow are Navier-Stoke equations:

$$\rho_e\left(\frac{\partial u}{\partial t}+u\frac{\partial u}{\partial x}+v\frac{\partial u}{\partial y}+w\frac{\partial u}{\partial z}\right)=F_x-\frac{\partial p}{\partial x}+\mu\left(\frac{\partial^2 u}{\partial x^2}+\frac{\partial^2 u}{\partial y^2}+\frac{\partial^2 u}{\partial z^2}\right) \tag{4.27}$$

$$\rho_e\left(\frac{\partial v}{\partial t}+u\frac{\partial v}{\partial x}+v\frac{\partial v}{\partial y}+w\frac{\partial v}{\partial z}\right)=F_y-\frac{\partial p}{\partial y}+\mu\left(\frac{\partial^2 v}{\partial x^2}+\frac{\partial^2 v}{\partial y^2}+\frac{\partial^2 v}{\partial z^2}\right) \tag{4.28}$$

$$\rho_e\left(\frac{\partial w}{\partial t}+u\frac{\partial w}{\partial x}+v\frac{\partial w}{\partial y}+w\frac{\partial w}{\partial z}\right)=F_z-\frac{\partial p}{\partial z}+\mu\left(\frac{\partial^2 w}{\partial x^2}+\frac{\partial^2 w}{\partial y^2}+\frac{\partial^2 w}{\partial z^2}\right) \tag{4.29}$$

The continuity condition gives:

$$\frac{\partial u}{\partial x}+\frac{\partial v}{\partial y}+\frac{\partial w}{\partial z}=0 \tag{4.30}$$

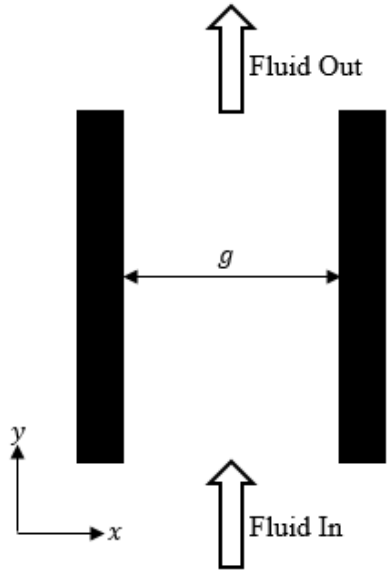

Figure 4.2 Illustration of laminar flow between parallel plates.

Since the Reynold Number of electrolyte is [3]:

$$\text{Re} = \frac{V_F g_0}{\nu} = \frac{4m/s \times 0.0003m}{1 \times 10^{-6} m^2/s} = 1200 < 2320 \tag{4.31}$$

The electrolyte flow between two parallel planes follows a laminar flow. In addition, to simplify the analysis process, following assumptions are made:

i) The fluid between two parallel planes is Newtonian flow;

ii) The fluid is incompressible;

iii) The fluid flow follows a laminar flow.

Consider a two-dimensional, steady, laminar flow along a straight channel with parallel flat walls, spaced at distance g apart, as shown in Figure 4.2. Neglect the effect of electrode vibration on electrolyte flown in the x direction, that is, assume the $u = 0$ and $w = 0$. The continuity Equation (4.30) yields:

$$\frac{\partial v}{\partial y} = 0 \tag{4.32}$$

Then:

$$v = v(y) \tag{4.33}$$

$$\frac{\partial^2 v}{\partial y^2} = 0 \tag{4.34}$$

From Equations (4.27) and (4.29) for the x and z direction:

$$\frac{\partial p}{\partial x} = \frac{\partial p}{\partial z} = 0 \tag{4.35}$$

$$\frac{\partial p}{\partial y} = constant \tag{4.36}$$

The Navier-Stokes equations for the y direction then becomes:

$$\frac{dp}{dy} = \mu \frac{d^2 v}{dx^2} \tag{4.37}$$

4.2.2 Anode Moves Away from Cathode

In this section, the flow speed of a particle which located between two parallel plates is calculated. Fluid flows inside the parallel plates at a constant speed, and one plate vibrates following a sine wave at varied vibration frequencies and amplitudes, as shown in Figure 4.3.

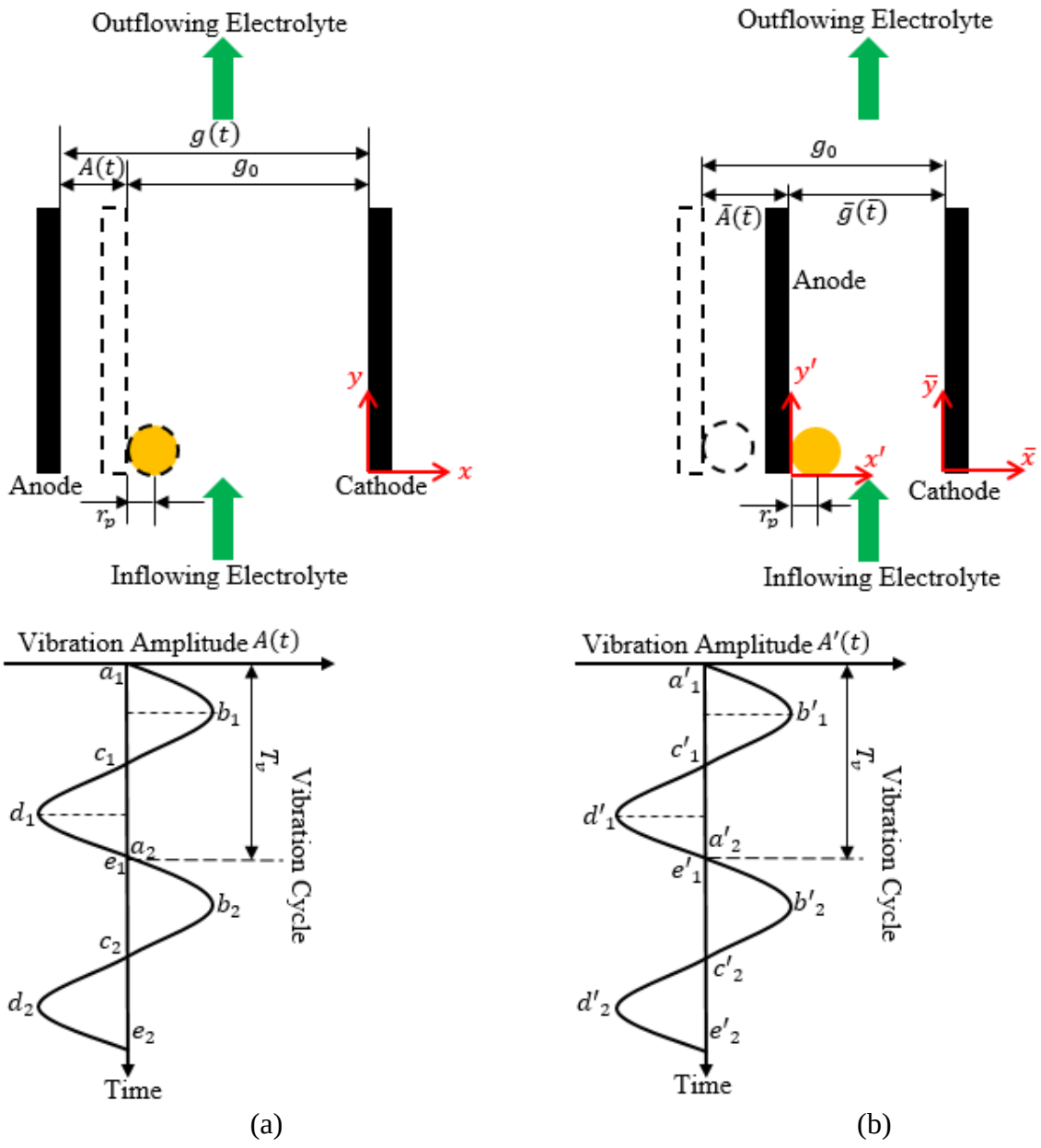

(a) (b)

Figure 4.3 Coordinate system in vibration assisted PECM.
(a) the anodic workpiece moves away from the cathodic electrode; (b) the anodic workpiece moves toward to the cathodic electrode.

As shown in Figure 4.3a, for vibration cycle i ($i = 1,2,3, \dots, n$), the segments from b_i to c_i and from c_i to d_i mean that the anodic workpiece moves away from the cathodic

electrode. During the 1st cycle with period T_v, segment from b_1 to d_1 can be interpreted as:

$$\frac{T_v}{4} \le t \le \frac{3T_v}{4} \Rightarrow \frac{(4\times 1)-3}{4}T_v \le t \le \frac{(4\times 1)-1}{4}T_v \tag{4.38}$$

During the 2nd cycle, segment from b_2 to d_2 can be interpreted as:

$$\frac{5T_v}{4} \le t \le \frac{7T_v}{4} \Rightarrow \frac{(4\times 2)-3}{4}T_v \le t \le \frac{(4\times 2)-1}{4}T_v \tag{4.39}$$

Similarly, during the ith cycle, the segment from b_i to d_i can be interpreted as:

$$\frac{4i-3}{4}T_v \le t \le \frac{4i-1}{4}T_v \tag{4.40}$$

The vibration period and frequency relate by:

$$T_v = \frac{1}{f} \tag{4.41}$$

Thus, segments from b_i to d_i can be labeled as:

$$\left(\frac{4i-3}{4}\right)\frac{1}{f} \le t \le \left(\frac{4i-1}{4}\right)\frac{1}{f} \quad i = 1,2,3,\cdots \tag{4.42}$$

When anodic workpiece moves away from the cathodic electrode, the gap between the anode and the cathode is increasing. The origin of the xy coordinate system locates at the cathodic electrode's surface. At $t = 0$, the location of the anodic surface is illustrated as the dotted line, and the gap between the anode and the cathode is g_0. At time t ($\frac{4i-3}{4f} \le$

$t \leq \frac{4i-1}{4f}$ $i = 1,2,3,\cdots)$, the anodic workpiece moves at a distance of $A(t)$ with the reference of its initial location, and $A(t)$ is defined as:

$$A(t) = A_v \sin(2\pi f t) \tag{4.43}$$

For segment from b_i to c_i, $A_v \sin(2\pi f t) > 0$, that is, the anodic workpiece moves from the minimum gap location to its initial location, the gap between the anode surface and cathode surface is increasing but it is smaller than its initial gap g_0, and can be written as:

$$g(t) = g_0 - |A(t)| = g_0 - A_v \sin(2\pi f t) \tag{4.44}$$

For segment from c_i to d_i, $A_v \sin(2\pi f t) < 0$, that is, the anodic workpiece moves from its initial location to the maximum gap location, the gap between the anode surface and cathode surface is increasing and it is larger than its initial gap g_0, and can be written as:

$$g(t) = g_0 + |A(t)| = g_0 - A_v \sin(2\pi f t) \tag{4.45}$$

Therefore, combine Equations (4.44) and (4.45), for segments from b_i to d_i, the gap between the anode surface and cathode surface $g(t)$ is defined as:

$$g(t) = g_0 - A_v \sin(2\pi f t) \tag{4.46}$$

Assume at every time, the electrolyte flow follows laminar flow pattern, that is, the electrolyte flow speed equals zero at both the cathodic electrode and the anodic workpiece surfaces. Then, the boundary conditions for Equation (4.37) are:

$$v = 0 \text{ at } x = 0 \text{ (Cathode surface) and} \tag{4.47}$$

$$v = 0 \text{ at } x = -|g(t)| = -g_0 + A_v \sin(2\pi f t) \text{ at anode surface} \tag{4.48}$$

The 2nd order differentiation Equation (4.37) has the general solution form:

$$v(x,t) = \frac{1}{2\mu}\frac{dp}{dy}x^2 + C_1 x + C_2 \tag{4.49}$$

By substituting the boundary conditions from Equations (4.47) and (4.48) into Equation (4.49), the constants C_1 and C_2 are:

$$C_1 = \frac{1}{2\mu}\frac{dp}{dy}g(t) = \frac{1}{2\mu}\frac{dp}{dy}[g_0 - A_v \sin(2\pi f t)] \tag{4.50}$$

$$C_2 = 0 \tag{4.51}$$

Then, Equation (4.49) becomes:

$$v(x,t) = \frac{1}{2\mu}\frac{dp}{dy}[x^2 + |g(t)|x] = \frac{1}{2\mu}\frac{dp}{dy}\{x[x + g_0 - A_v \sin(2\pi f t)]\} \tag{4.52}$$

Since a particle with a radius r_p releases at the anode surface at time t_1,

$$\frac{4i-3}{4f} \le t_1 < t \le \frac{4i-1}{4f} \quad i = 1,2,3,\cdots \tag{4.53}$$

where i is the number of vibration cycle.

Figure 4.3 shows the particle center location is:

$$x_p = -|g(t_1)| + r_p = -g_0 + A_v \sin(2\pi f t_1) + r_p \tag{4.54}$$

Assuming the particle's flow speed is equal to the electrolyte flow speed at the particle center, then the particle's flow speed V_p becomes:

$$V_p(t) = v\big(x_p, t\big) = v(-|g(t_1)| + r_p, t) \tag{4.55}$$

Combine Equations (4.52) and (4.55), then Equation (4.55) becomes:

$$\begin{aligned}
V_p(t) = v(x,t) &= v\big(-|g(t_1)| + r_p, t\big) \\
&= \frac{1}{2\mu}\frac{dp}{dy}\{x[x + |g(t)|]\} \\
&= \frac{1}{2\mu}\frac{dp}{dy}\big[-|g(t_1)| + r_p\big]\big[-|g(t_1)| + r_p + g(t)\big] \\
&= \frac{1}{2\mu}\left(-\frac{dp}{dy}\right)\big[|g(t_1)| - r_p\big]\big[r_p + |g(t)| - |g(t_1)|\big] \\
&= \frac{1}{2\mu}\left(-\frac{dp}{dy}\right)\big[g_0 - A_v \sin(2\pi f t_1) - r_p\big]\big[r_p + g_0 \\
&\qquad - A_v \sin(2\pi f t) - g_0 + A_v \sin(2\pi f t_1)\big] \\
&= \frac{1}{2\mu}\left(-\frac{dp}{dy}\right)\big[g_0 - A_v \sin(2\pi f t_1) - r_p\big]\big[r_p + A_v \sin(2\pi f t_1) \\
&\qquad - A_v \sin(2\pi f t)\big]
\end{aligned} \tag{4.56}$$

In this study, $g_0 \approx 300$ μm, $A_v \leq 10$ μm, r_p range from 2~10 μm, $\left[r_p + A_v \sin(2\pi f t_1)\right] \ll g_0$, then:

$$g_0 \approx g_0 - r_p - A_v \sin(2\pi f t_1) \tag{4.57}$$

Equation (4.56) becomes:

$$V_p(t) = \frac{1}{2\mu}\left(-\frac{dp}{dy}\right) g_0\{r_p + A_v[\sin(2\pi f t_1) - \sin(2\pi f t)]\} \tag{4.58}$$

Consider two vibrations with same vibration amplitude A_v and different vibration frequencies f_1 and f_2 with $f_2 > f_1$, as shown in Figure 4.4. At time t_1 (particle release from the anodic workpiece), both vibrations away from its initial location with a distance d_0. At time t, vibration 1 with f_1 vibration frequency moves away from its initial location with a distance d_{f1}, and vibration 2 with f_2 vibration frequency moves away from its initial location with a distance d_{f2}. Clearly:

$$\left|d_0 - d_{f2}\right| > \left|d_0 - d_{f1}\right|, \text{ or} \tag{4.59}$$

$$|\sin(2\pi f_2 t) - \sin(2\pi f_2 t_1)| > |\sin(2\pi f_1 t) - \sin(2\pi f_1 t_1)| \tag{4.60}$$

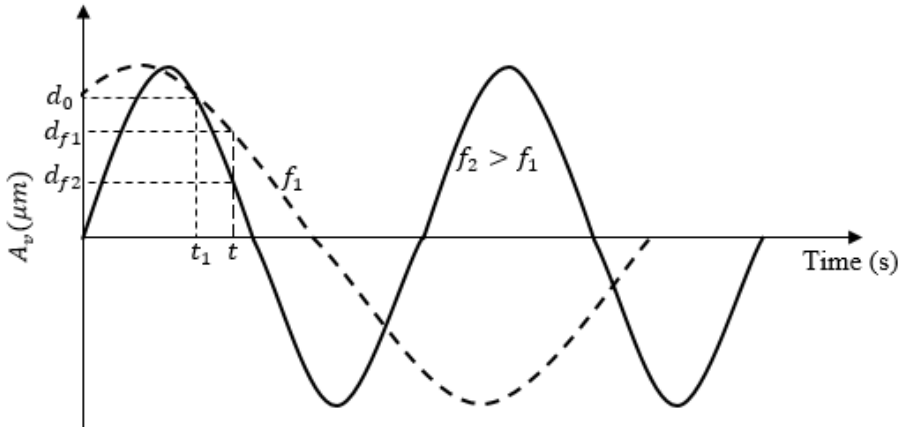

Figure 4.4 Comparison of vibration with different vibration frequencies.

For a vibration assisted PECM, with increasing of the vibration amplitude A_v or vibration frequency f, the particle flushing speed V_p in Equation (4.58) increases, therefore, the convection rate increases. In addition, since the particle flushing away speed is larger than that without vibration ($A_v = 0$), the concentration of particles in the double-diffusion layer also decreases which also improves the diffusion rate.

4.2.3 Anode Moves Toward Cathode

As shown in Figure 4.3b, for vibration cycle i ($i = 1,2,3, \dots, n$), the segments from a'_i to b'_i and from d'_i to e'_i mean that the anodic workpiece moves toward the cathodic electrode. During the 1st cycle with period T_v, the segment from a'_1 to b'_1 can be interpreted as:

$$0 \le t \le \frac{T_v}{4} \Rightarrow \frac{(4 \times 1) - 4}{4} T_v \le t \le \frac{(4 \times 1) - 3}{4} T_v \tag{4.61}$$

and the segment from d'_1 to e'_1 can be interpreted as:

$$\frac{3T_v}{4} \leq \bar{t} \leq T_v \Rightarrow \frac{(4 \times 1) - 1}{4} T_v \leq \bar{t} \leq \frac{(4 \times 1)}{4} T_v \tag{4.62}$$

During the 2nd cycle, the segment from a'_2 to b'_2 can be interpreted as:

$$T_v \leq \bar{t} \leq \frac{5T_v}{4} \Rightarrow \frac{(4 \times 2) - 4}{4} T_v \leq \bar{t} \leq \frac{(4 \times 2) - 3}{4} T_v \tag{4.63}$$

and the segment from d'_2 to e'_2 can be interpreted as:

$$\frac{7T_v}{4} \leq \bar{t} \leq 2T_v \Rightarrow \frac{(4 \times 2) - 1}{4} T_v \leq \bar{t} \leq \frac{(4 \times 2)}{4} T_v \tag{4.64}$$

Similarly, during the i^{th} cycle, the segment from a'_i to b'_i can be interpreted as:

$$\frac{4i - 4}{4} T_v \leq \bar{t} \leq \frac{4i - 3}{4} T_v \tag{4.65}$$

and the segment from d'_i to e'_i can be interpreted as:

$$\frac{4i - 1}{4} T_v \leq \bar{t} \leq \frac{4i}{4} T_v \tag{4.66}$$

Therefore, at ith cycle, the segments from a'_i to b'_i and from d'_i to e'_i can be interpreted as:

$$\frac{4i - 4}{4} T_v \leq \bar{t} \leq \frac{4i - 3}{4} T_v; \quad \frac{4i - 1}{4} T_v \leq \bar{t} \leq \frac{4i}{4} T_v; \quad i = 1,2,3, \ldots \tag{4.67}$$

Since, $T_v = 1/f$, thus, the time for the anodic workpiece moves toward the cathodic electrode can be written as:

$$\frac{4i-4}{4f} \le \bar{t} \le \frac{4i-3}{4f}; \quad \frac{4i-1}{4f} \le \bar{t} \le \frac{i}{f}; \quad i = 1,2,3,\cdots \tag{4.68}$$

When the anodic workpiece moves toward the cathodic electrode, the gap between the anode and cathode is decreasing (segments from a'_i to b'_i and from d'_i to e'_i, as in Figure 4.3b). For segments from a'_i to b'_i, $A_v \sin(2\pi f\bar{t}) > 0$, that is, the anodic workpiece moves from its initial location to the minimum gap location, the gap between the anode surface and cathode surface is decreasing and it is smaller than its initial gap g_0, and can be written as:

$$g(\bar{t}) = g_0 - |\bar{A}(\bar{t})| = g_0 - A_v \sin(2\pi f\bar{t}) \tag{4.69}$$

For segments from d'_i to e'_i, $A_v \sin(2\pi f\bar{t}) < 0$, that is, the anodic workpiece moves from the maximum gap location to its initial location, the gap between the anode surface and cathode surface is decreasing but it is larger than its initial gap g_0, and can be written as:

$$g(\bar{t}) = g_0 + |\bar{A}(\bar{t})| = g_0 - A_v \sin(2\pi f\bar{t}) \tag{4.70}$$

Therefore, at time $\bar{t}$ (from Equation (4.68)), the gap between the anode surface and cathode surface $\bar{g}(\bar{t})$ can be expressed as:

$$g(\bar{t}) = g_0 - A_v \sin(2\pi f\bar{t}) \tag{4.71}$$

Similarly, Equation (4.37) for the anodic workpiece moves away from the cathodic electrode is rewritten for the anodic workpiece moves toward the cathodic electrode:

$$\frac{dp}{d\bar{y}} = \mu \frac{d^2\bar{v}}{d\bar{x}^2} \tag{4.72}$$

Another local coordinate system $x'y'$ located at the surface of the anodic workpiece surface is constructed (Figure 4.3b). Equation (4.72) is also valid in the $x'y'$ coordinate system, that is:

$$\frac{dp}{dy'} = \mu \frac{d^2v'}{dx'^2} \tag{4.73}$$

Assume at every time, the electrolyte flow follows laminar flow pattern, that is, electrolyte flow speed is equal to zero at both the cathodic electrode and the anodic workpiece surfaces. Then, the boundary condition for Equation (4.73) at anode surface:

$$v' = 0 \text{ at } x' = 0 \tag{4.74}$$

Since changing coordinate system does not change the distance between the cathode surface and anode surface ($|g'(t')| = |\bar{g}(\bar{t})|$), then the boundary condition for Equation (4.73) at cathode surface in the $x'y'$ coordinate system is:

$$\begin{aligned} v' = 0 \text{ at } x' = |g'(t')| = |\bar{g}(\bar{t})| &= g_0 - A_v \sin(2\pi f \bar{t}) \\ &= g_0 - A_v \sin(2\pi f t') \end{aligned} \tag{4.75}$$

Follow previous derivation, the differential Equation (4.73) has the general solution form:

$$v'(x', t') = \frac{1}{2\mu}\frac{dp}{dy'}x'^2 + C'_1 x' + C'_2 \tag{4.76}$$

Combine with new boundary condition Equations (4.74) and (4.75) to obtain the following expressions for C'_1 and C'_2:

$$C'_1 = -\frac{1}{2\mu}\frac{dp}{dy'}|g'(t')| = -\frac{1}{2\mu}\frac{dp}{dy'}[g_0 - A_v \sin(2\pi f t')] \tag{4.77}$$

$$C'_2 = 0 \tag{4.78}$$

Then, Equation (4.76) becomes:

$$v'(x', t) = \frac{1}{2\mu}\frac{dp}{dy}\{x'^2 - [g_0 - A_v \sin(2\pi f t')]x'\} \tag{4.79}$$

The vibration of the anodic workpiece in this case pushes the particle along the x' direction while keeping particle in contact with the anodic workpiece. Let the particle radius to be r_p, then the particle center location is always:

$$x'_p = r_p \tag{4.80}$$

Assuming the particle's flow speed is equal to the electrolyte flow speed at the particle center, then the particle's flow speed V'_p becomes:

$$V'_p(t') = v'(x'_p, t') = v'(r_p, t') \tag{4.81}$$

and

$$\frac{4i-4}{4f} \le t' < t \le \frac{4i-3}{4f}; \quad \frac{4i-1}{4f} \le t' < t \le \frac{i}{f}; \quad i = 1,2,3,\cdots \tag{4.82}$$

Combine Equations (4.79) and (4.81), Equation (4.81) becomes:

$$\begin{aligned} V'_p(r_p, t') &= v'(x'_p, t') = v'(r_p, t') \\ &= \frac{1}{2\mu}\frac{dp}{dy}\{x'^2 - [g_0 - A_v \sin(2\pi f t')]x'\} \\ &= \frac{1}{2\mu}\left(-\frac{dp}{dy}\right)\{x'[-x' + g_0 - A_v \sin(2\pi f t')]\} \\ &= \frac{1}{2\mu}\left(-\frac{dp}{dy}\right) r_p\left[-r_p + g_0 - A_v \sin(2\pi f t')\right] \end{aligned} \tag{4.83}$$

In this investigation, $g_0 \approx 300$ μm, $A_v \leq 10$ μm, r_p ranges from 2~10 μm, thus $\left[-r_p - A_v \sin(2\pi f t_1)\right] \ll g_0$, then:

$$g_0 - r_p + A_v \sin(2\pi f t') \approx g_0 \tag{4.84}$$

Then, Equation (4.83) becomes:

$$V'_p(t') \approx \frac{1}{2\mu}\left(-\frac{dp}{dy}\right) r_p g_0 \tag{4.85}$$

Therefore, for a vibration assisted PECM, when the anode moves toward cathode, a particle always contacts with the anode surface, the effects of vibration amplitude and vibration frequency on the particle flushing speed are insignificant. However, since the resistance of electrolyte layer is reduced due to the smaller value of IEG, more anodic atoms are ionized.

5 SIMULATION MODEL DEVELOPMENT

Referring to Equations (3.3) and (3.4), the ECM process for steel would form the iron hydroxide by-products that need to be flushed away. The by-products were assumed to be spherical particles with the dimensions to be measured experimentally. This section shows two simulations on how multiple particles and a single particle are being flushing away between a cathodic electrode and an anodic workpiece.

i) The Star CCM+ software simulates how multiple particles dispersed in the continuous phase flow in a vibration assisted pulsed ECM. This software includes a discrete element model (DEM) that simulates and calculates the particle trajectory and their interactions with the environment.

ii) The ANSYS Fluent software simulates how a single particle move in a vibration assisted pulsed ECM. This software calculates the discrete phase trajectory using a Lagrangian formulation that includes the discrete phase inertia, hydrodynamic drag and gravity force, for both steady and unsteady flow. In theoretical analysis, the particle flushing speed was approximately equal to the fluid flow speed for simplification. However, in Fluent simulation, average particle's flushing speed will ultimately be calculated. Detailed modeling of a single particle flow is included in Appendix A. However, the Fluent software is incapable of dealing with the particle-particle interactions in a simulation domain.

iii) The effects of vibration frequencies and vibration amplitudes on particle's average flushing speed are also simulated using the ANSYS Fluent software.

Define:

a_r	Particle acceleration along the radial direction (m/s^2)
A_v	Anodic workpiece vibration amplitude (μm)
B	Magnetic flux density (Wb/m^2)
f	Vibration frequency (Hz)
F_b	Buoyance force (N)
F_c	Force generated in the armature coil (N)
F_d	Drag force (N)
F_r	Total force along the radial direction (N)
g	Inter-electrode gap (μm)
g_0	Inter-electrode gap at time $t = 0$ (μm)
G	Gravity force (N)
I	Current (A)
I_{max}	Maximum driven current for armature coil (A)
K_1	Physical constant
L_a	Arc length of a simulation domain (μm)
L_c	Length of conductor in the gap (mm)
m_A	Mass attached on armature coil (kg)
m_p	Mass of particle (g)
r_p	Particle radius (μm)
r_{pi}	Particle injection rate (times/s)
T	Electrolyte temperature (℃)

T_v	Vibration period time (s)
V_e	Average electrolyte flow speed (m/s)
V_F	Fluid phase flow velocity (m/s)
V_w	Workpiece moving speed (μm/s)
w_t	Electrode tube thickness (μm)
x	Location of workpiece relative to the fixed origin (μm)
φ	Angle between particle and horizontal reference (°)

5.1 Multiple Particles Simulation

A schematic illustration of a horizontal vibration ECM in the x_0y_0 plane is shown in Figure 5.1. The tubular cathodic electrode outside diameter is ϕ9.5 mm and the tube wall thickness is 300 μm. The electrolyte, which flowed inside the cathodic electrode, flushed away the by-products from the workpiece surface. A single by-product (represented as a particle), whose free body diagram in the y_0z_0 plane is shown in Figure 5.2. This particle, locates between the anodic workpiece and the tubular cathodic electrode and forms an angle φ with the horizontal axis, and is subjected to gravity force G, buoyance force F_b, and drag force F_d in the flowing electrolyte. Due to the axisymmetric feature of the cathodic electrode, the drag force is in a radial direction away from the tube center. When projecting all forces in the radial direction:

$$F_r = F_d - (G - F_b)\sin\varphi = m_p a_r \tag{5.1}$$

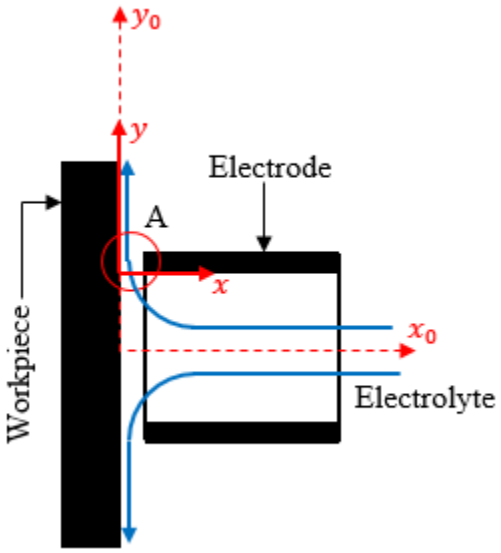

Figure 5.1 Front view of the cathodic electrode and the anodic workpiece in the x_0y_0 plane.

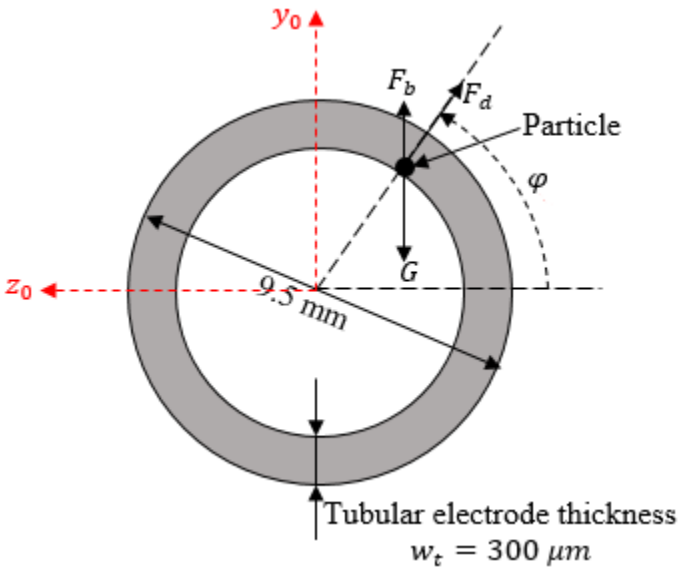

Figure 5.2 Free-body diagram of a particle in the y_0z_0 plane.

Since the solid particle density is higher than the density of the electrolyte, the buoyance force of this particle is always smaller than its gravity force, thus the minimum value of

the radial direction force is equal to $F_d - (G - F_b)$ when $\varphi = \pi/2$, and the maximum value of this force is equal to $F_d + (G - F_b)$ when $\varphi = 3\pi/2$. The location at $\varphi = \pi/2$ is the hardest location for a reaction particle to be flushed away from and is chosen for the simulation domain, and is illustrated as A in Figure 5.1. The enlarged view of the location A in Figure 5.1 is illustrated in Figure 5.3. Define the xy coordinate system to be located at the bottom left corner of the simulation zone and translates along the anodic workpiece vibration.

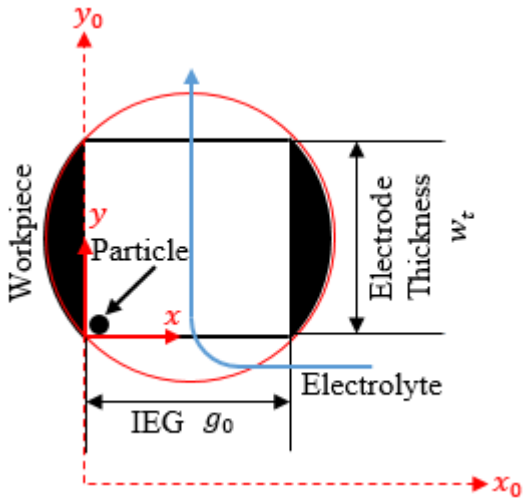

Figure 5.3 Enlarged view of simulation location in the x_0y_0 plane.

The Star CCM+ software simulates the process of capturing the particle-particle interaction in a multiple particles fluid-particle flow system. As shown in Figure 5.4 and Figure 5.5, in the Star CCM+ simulation, the flow domain is located at $\varphi = \pi/2$ and the interested simulation domain is a rectangular solid with the dimensions of $g_0 \times w_t \times L_a$.

During the simulation, particles with the radius of r_p are continuously injected at four different locations (x_{ij}, y_{ij}, z_{ij}), where $i = \mathrm{I}, \mathrm{II}, \mathrm{III}, \mathrm{IV}$, which are the injection location numbers, and j is the sub-simulation step. The y coordinate for location I & II is arbitrarily chosen to be 50 µm, and that for locations III & IV to be 0 µm. Similarly, the z coordinate for locations I & III is 5 µm and that for II & IV is -5 µm. In addition, y and z coordinates are fixed but the x coordinate will be changed as the simulation continues.

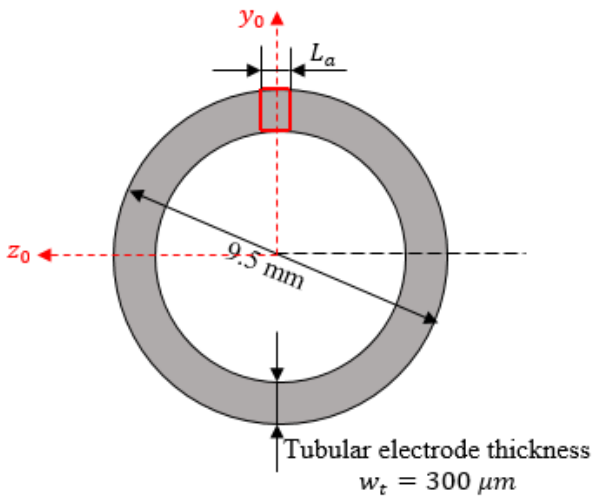

Figure 5.4 Illustration of flow domain in the $y_0 z_0$ plane for the Star CCM+ software.

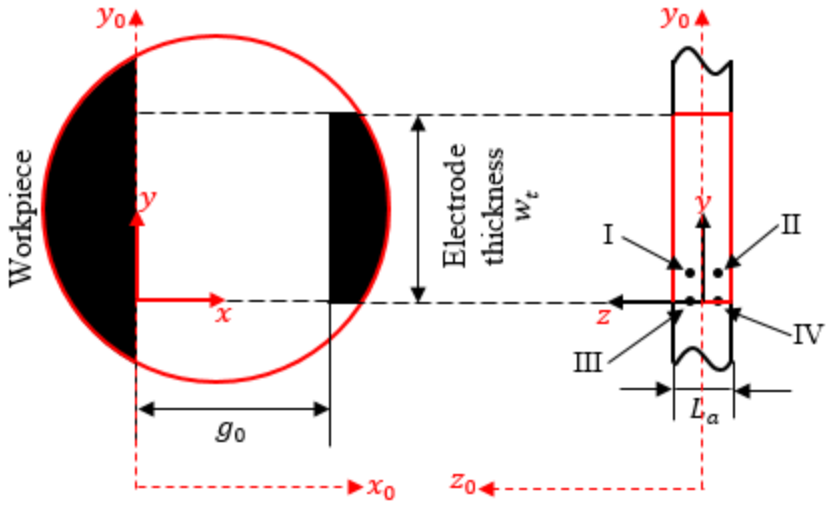

Figure 5.5 Particle injection locations in fluid domain.

To include the workpiece vibration, an enlarged simulation domain is used in Star CCM+ software, as shown in Figure 5.6. A coarse grid domain is used to calculate the fluid flow, and an overset mesh domain with fine mesh and $L_a = 20$ µm width is used to capture the movement of the workpiece. The calculated values from both coarse mesh and fine mesh are transmitted through a linear interpolation. The electrolyte flows into the simulation domain through the "Inlet" surface at a speed of V_F. The workpiece vibration follows a sine wave (Figure 5.7a) and is estimated as a triangular wave (Figure 5.7b).

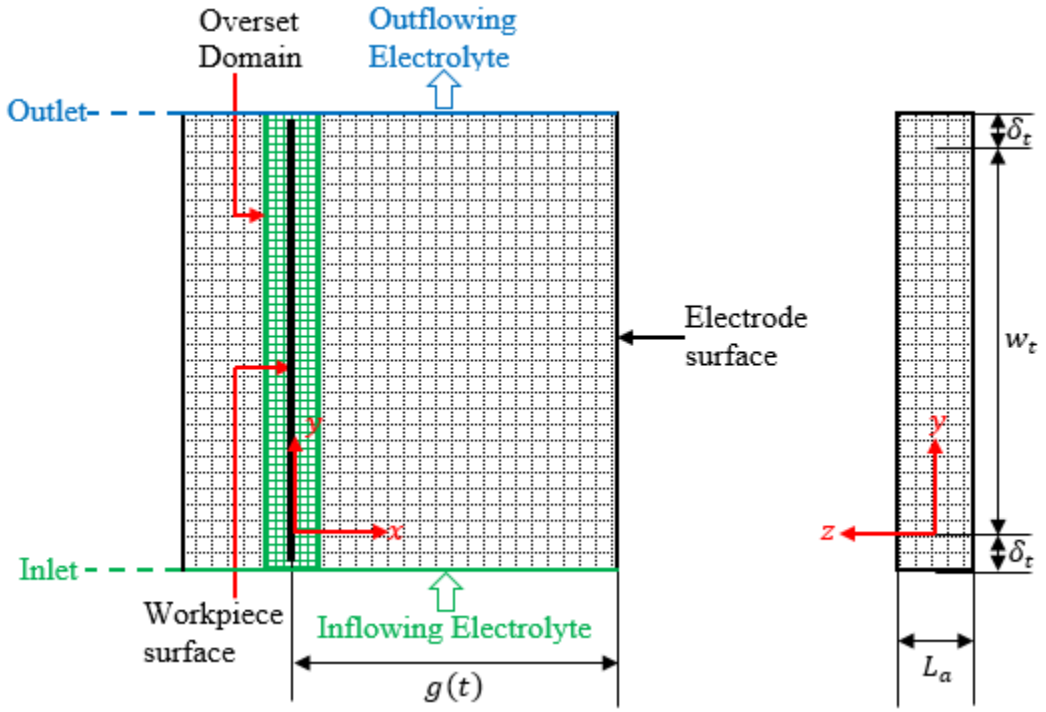

Figure 5.6 Illustration of the Star CCM+ simulation domain.

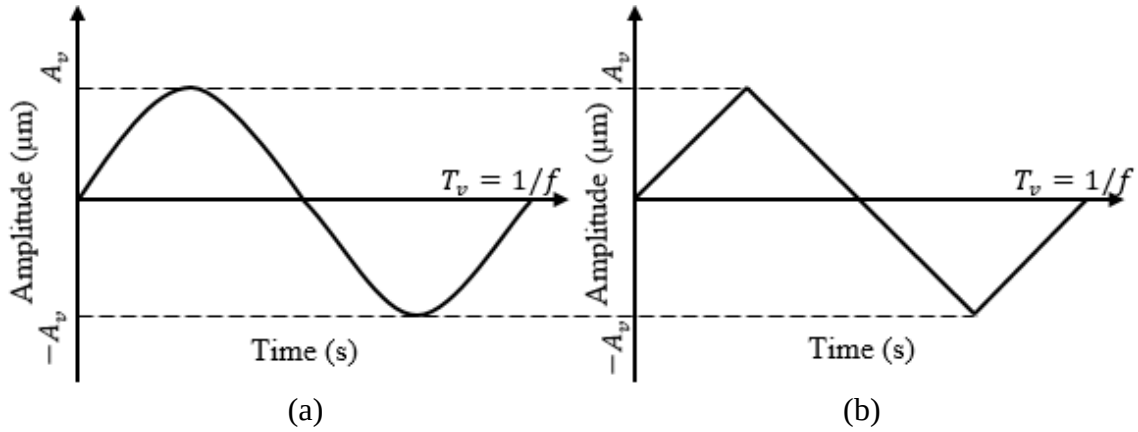

Figure 5.7 (a) Sine wave (b) Approximation of sine wave in Star CCM+.

Since the workpiece vibration frequency is f and vibration amplitude is A_v, the workpiece moving speed is equal to the slope of the triangular wave:

$$V_w = \frac{A_v}{T_v/4} = \frac{A_v}{1/4f} = 4fA_v \tag{5.2}$$

To observe the particle movement, the simulation zone (Figure 5.6b) is divided by equals segments with the length of 50 μm, as shown in Figure 5.8. Figure 5.8a is a color bar which demonstrates the particle residence time in the simulation domain. Figure 5.8b is the simulation domain. Four green points, I, II, III and IV, represent the particle injection locations. In the simulation, the particle injection rate is r_{pi} (times/s), vibration amplitude and vibration frequency are set to the highest value since this combination yields the best flushing speed, i.e., 40 Hz vibration frequency and 10 μm vibration amplitude. Other simulation parameters are identical to the experiment conditions. The summary of parameters used in the Star CCM+ multiple particles simulation is listed in Table 5.1.

.

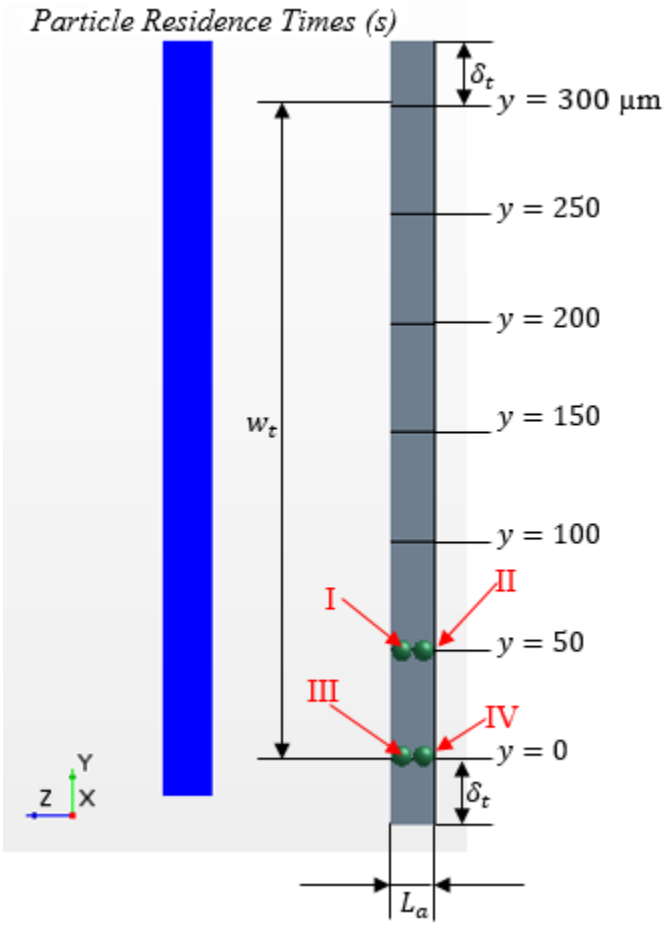

(a) (b)

Figure 5.8 Illustration of workpiece and particle injection locations in the Star CCM+ software simulation domain.

Table 5.1 Multiple particles simulation parameters

Variables	Values
Vibration frequency f (Hz)	40
Vibration amplitude A_v (μm)	10.0
Electrolyte flow speed V_e (m/s)	4.0
Electrode wall thickness w_t (μm)	300
Flow domain arc length L_a (μm)	20
Particle injection rate r_{pi} (times/s)	10^6
Initial electrode gap g_0 (μm)	300

In the ECM, particles are always released from the workpiece surface, but the particle injection locations are changing continuously. To simplify the simulation, a vibration cycle is divided into 20 equal time intervals, as shown in Figure 5.9. At each time interval, injection locations in the y-direction are kept constant.

When the anodic workpiece moves away from the cathodic electrode, during the time interval 0-1, the workpiece moves from x_0 to $-x_1$, as shown in Figure 5.10a, the particles (represented as green circle "a" and green box "b") are injected from its initial x location (x_0). When the anodic workpiece reaches the $-x_1$ and continues move to $-x_2$ (segment from 1 to 2), the new particles (represented as red triangle "c" and red hexagon "d") are injected at location $-x_1$. Similarly, for time interval 2-3, 3-4, 4-5, 15-16, 16-17, 17-18,

18-19 and 19-20, particles are injected at locations $-x_2$, $-x_3$, $-x_4$, x_5, x_4, x_3, x_2 and x_1 respectively.

After segment from 4 to 5, the anodic workpiece reverses move toward the cathodic electrode, during the time interval 5-6, the workpiece moves from $-x_5$ to $-x_4$, as shown in Figure 5.10b, the particles (represented as blue circle "e" and blue box "f") are injected form its ending x location $(-x_4)$. When the workpiece reaches the $-x_4$ and continues move to $-x_3$ (segment from 6 to 7), the particles (represented purple triangle "g" and purple hexagon "h") are injected at location $-x_3$. Similarly, for time intervals 7-8, 8-9, 9-10, 10-11, 11-12, 12-13, 13-14 and 14-15, the particles are rejected at locations $-x_2$, $-x_1$, x_0, x_1, x_2, x_3, x_4, x_5, respectively.

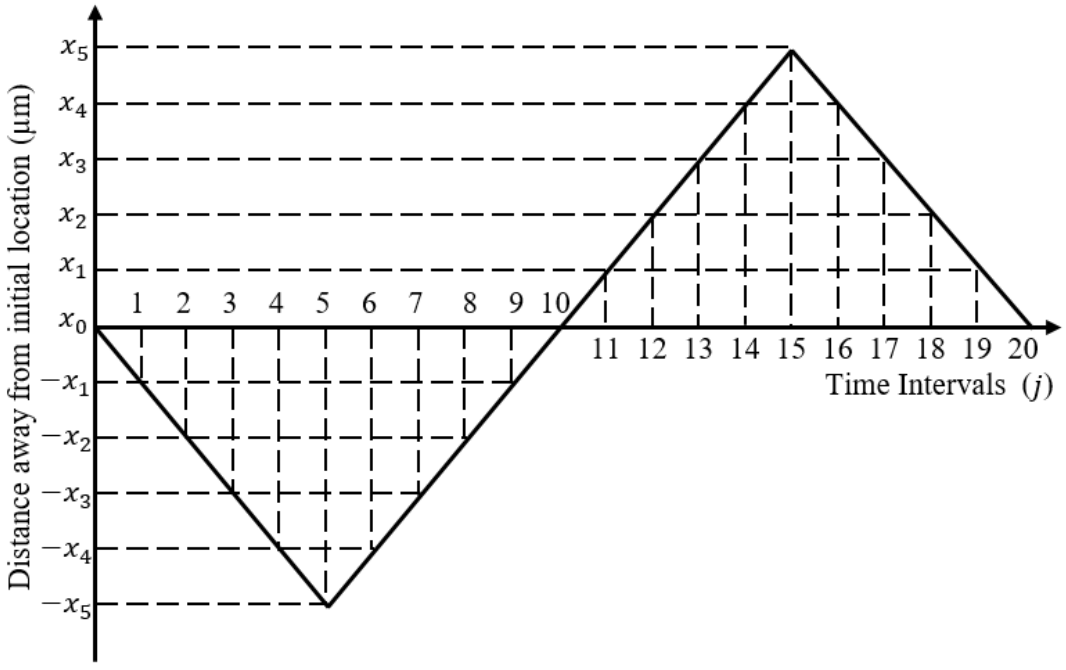

Figure 5.9 Illustration of simulation time intervals.

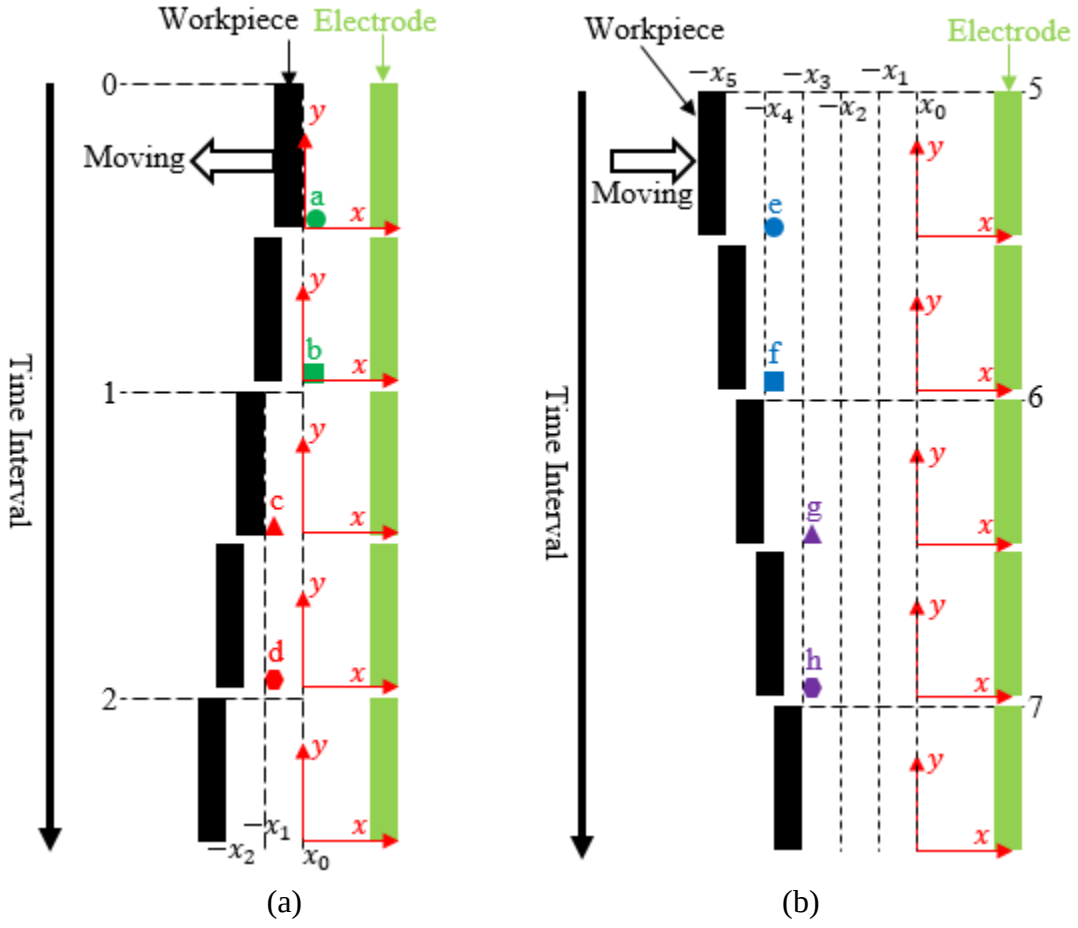

Figure 5.10 Illustration of particle injection location in Star CCM+ simulation.

For the time interval 0-1 in Figure 5.9, since vibration frequency is 40 Hz, the vibration period time is $T_v = 1/40\ s = 0.025$ s, and each time interval is $T_v/20 = 0.00125\ s = 1.25\ ms$. In addition, due to the vibration amplitude of 10 μm, each increment in the x direction is $A_v/5 = 2$ μm. Moreover, the 2 μm particle diameter (shown latter in experiment section) is released from the anodic workpiece surface, x coordinate is fixed at 1 μm for the time from 0-1.25 ms, as shown in Figure 5.11.

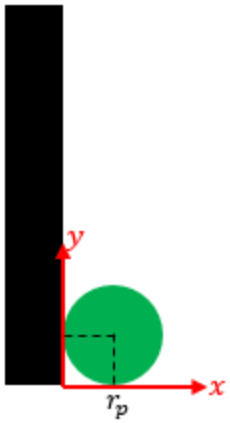

Figure 5.11 Illustration of $x-$ coordinate of particle injection location.

The y coordinates for particle injection locations I & II are 50 μm during vibration and that for III & IV locations are 0 μm. The z coordinates for particle injection locations I & III are 5 μm during vibration and that for III & IV locations are -5 μm. Thus, for the time interval 0-1.25 ms, the location I coordinate is $(x, y, z) = (1, 50, 5)$ μm, the location II coordinate is (1, 50, -5) μm, the location III coordinate is (1, 0, 5) μm, and the location IV coordinate is (1, 0, -5) μm, as shown in the first row in Table 5.2. For time interval 1-2 (Figure 5.9), that is, from 1.2-2.5 ms, the yz coordinates all the same and the x coordinate is changed to -1, that is, the location I, II, III and IV coordinates are (-1, 50, 5) μm, (-1, 50, -5) μm, (-1, 0, 5) μm and (-1, 0, -5) μm, as shown in second row in Table 5.2. The detailed particle rejection locations' coordinates are listed in Table 5.2.

The simulation results of Star CCM+ will be illustrated in later sections and they will be compared with the results simulated by ANSYS Fluent for a single particle flow.

Table 5.2 List of particle injection coordinates.

Simulation Time (ms)	Location I (μm) (x_{1j}, y_{1j}, z_{1j})	Location II (μm) (x_{2j}, y_{2j}, z_{2j})	Location III (μm) (x_{3j}, y_{3j}, z_{3j})	Location IV (μm) (x_{4j}, y_{4j}, z_{4j})
0 – 1.25	(1, 50, 5)	(1, 50, -5)	(1, 0, 5)	(1, 0, -5)
1.25 –2.50	(-1, 50, 5)	(-1, 50, -5)	(-1, 0, 5)	(-1, 0, -5)
2.50 – 3.75	(-3, 50, 5)	(-3, 50, -5)	(-3, 0, 5)	(-3, 0, -5)
3.75 – 5.00	(-5, 50, 5)	(-5, 50, -5)	(-5, 0, 5)	(-5, 0, -5)
5.00 – 6.25	(-7, 50, 5)	(-7, 50, -5)	(-7, 0, 5)	(-7, 0, -5)
6.25 – 7.50	(-7, 50, 5)	(-7, 50, -5)	(-7, 0, 5)	(-7, 0, -5)
7.50 – 8.75	(-5, 50, 5)	(-5, 50, -5)	(-5, 0, 5)	(-5, 0, -5)
8.75 – 10.00	(-3, 50, 5)	(-3, 50, -5)	(-3, 0, 5)	(-3, 0, -5)
10.00 – 11.25	(-1, 50, 5)	(-1, 50, -5)	(-1, 0, 5)	(-1, 0, -5)
11.25 – 12.50	(1, 50, 5)	(1, 50, -5)	(1, 0, 5)	(1, 0, -5)
12.50– 13.75	(3, 50, 5)	(3, 50, -5)	(3, 0, 5)	(3, 0, -5)
13.75 – 15.00	(5, 50, 5)	(5, 50, -5)	(5, 0, 5)	(5, 0, -5)
15.00 – 16.25	(7, 50, 5)	(7, 50, -5)	(7, 0, 5)	(7, 0, -5)
16.25 – 17.50	(9, 50, 5)	(9, 50, -5)	(9, 0, 5)	(9, 0, -5)
17.50 – 18.75	(11, 50, 5)	(11, 50, -5)	(11, 0, 5)	(11, 0, -5)
18.75 – 20.00	(11, 50, 5)	(11, 50, -5)	(11, 0, 5)	(11, 0, -5)
20.00 – 21.25	(9, 50, 5)	(9, 50, -5)	(9, 0, 5)	(9, 0, -5)
21.25 – 22.50	(7, 50, 5)	(7, 50, -5)	(7, 0, 5)	(7, 0, -5)
22.50 – 23.75	(5, 50, 5)	(5, 50, -5)	(5, 0, 5)	(5, 0, -5)
23.75 – 25.00	(3, 50, 5)	(3, 50, -5)	(3, 0, 5)	(3, 0, -5)

5.2 Single Particle Simulation

Referring to the previous Figure 5.3, the wall thickness of the cathodic electrode is w_t and the initial distance between the cathodic electrode and the anodic workpiece is g_0. Hence, the simulation zone is a rectangular domain with a dimension of $w_t \times g_0$. The electrolyte inward flowing speed is V_e in this simulation. In the simulation, the workpiece vibrates along the x direction with the varied vibration amplitude A_v and vibration frequency f.

The workpiece vibration follows the sine wave:

$$x = -A_v \sin(2\pi f t) \tag{5.3}$$

In the beginning, the particle center is located at the lower left corner (Figure 5.3) with particle initial velocity of 0 m/s. Vibration frequencies are 20, 30 and 40 Hz and vibration amplitudes are 5, 7.5 and 10 μm as in experiments. Varied electrolyte flow rates are 2, 3 and 4 m/s. Experiment conditions in the simulation are summarized in Table 5.3. A simulation procedure will be stopped when the y-coordinate of the particle center is larger than the electrode wall thickness w_t, i.e. when the particle is flushed away from the electrode surface.

Table 5.3 Boundary conditions in single particle simulation.

Variables	Values
Vibration frequency f (Hz)	20, 30, 40
Vibration amplitude A_v (μm)	5.0, 7.5, 10.0
Electrolyte flow speed V_e (m/s)	2.0, 3.0, 4.0
Particle diameter (μm)	2, 3, 4, 5, 6, 7, 8, 9, 10
Electrode wall thickness w_t (μm)	300

To investigate the influence of the vibration frequency, vibration amplitude, electrolyte flow speed, particle size and particle locations on the average flushing speed, a series of simulations are conducted:

i) The first series of simulations are used to build a relationship between the experimental results and the simulation results. Three input levels for three variables are set (Table 5.3). Thus, the total number of simulation runs is $3^3 = 27$.

ii) The second series of simulations are used to theoretically investigate the maximum flushing speed for the experimental system. The electrolyte flow speed is fixed at 4 m/s, and input current for vibration table is fixed at its maximum value (7 A). Since the force generated in the armature coil is always defined by Equation (5.4) [75]:

$$F_c = K_1 B L_c I (2.54)^2 \tag{5.4}$$

For a sine wave current, the transient current is:

$$I = I_{max} \sin(2\pi f t) \tag{5.5}$$

Then, the generated force is:

$$F_c = K_1 B L_c I_{max} (2.54)^2 \sin(2\pi f t) \tag{5.6}$$

According to Newton's second law, the driving force of the vibration is calculated by taking derivative of Equation (5.3):

$$F_{dv} = m_A \ddot{x} = m_A A_v 4\pi^2 f^2 \sin(2\pi f t) \tag{5.7}$$

$$F_c = F_{dv} \tag{5.8}$$

Combining Equations (5.6) -(5.8), the relation between vibration frequency and vibration amplitude for given input current yields:

$$A_v f^2 = \frac{K_1 B L_c (2.54)^2}{4\pi^2 f^2 m_A} I_{max} = constant \tag{5.9}$$

The corresponding vibration frequency and vibration amplitude are listed in Table 5.4.

iii) The third series of simulations are used to investigate the effect of particle size on the average flushing speed. The remain parameters are fixed at the combinations which yield maximum average flushing speed from second

series of simulations' results, i.e. $V_e = 4$ m/s, $A_v = 10$ μm and $f = 40$ Hz. Particle sizes are ranged from 2 μm to 10 μm.

The discrete phase formulation used by ANSYS Fluent software is based on the assumption that the discrete phase is sufficiently dilute so that the particle-particle interactions and the effects of the particle volume fraction on the continuous phase are negligible [76]. In practice, these issues imply that the discrete phase must be present at a low volume fraction, namely, less than 10-12%. This limitation is also known as particle volume fraction limitation.

In additions to volume fraction limitation, the following limitations are also apparent for the discrete-phase method [76].

i) Limitation on modeling continuous suspensions of particles;

ii) Limitation on modeling particle rotation;

iii) Limitation on using the DPM with other ANSYS Fluent models;

iv) Limitation on using the hybrid parallel method;

v) Limitation on using the Lagrangian Wall Film Model

Table 5.4 Corresponding vibration amplitude and frequency for maximum input power.

Vibration Frequency (Hz)	Vibration Amplitude (μm)
10	160.00
20	40.00
30	17.80
40	10.00
50	6.40
60	4.44
70	3.26
80	2.50
90	1.98
100	1.60
110	1.32
120	1.11
130	0.95
140	0.82
150	0.71
175	0.52
200	0.40
500	0.065
1000	0.016
5000	0.00064
10000	0.00016

6 EXPERIMENTS [1]

6.1 Experiment set-up

To carry out this investigation, a unique laboratory horizontal vibration-assisted pulsed ECM system was developed and shown in Figure 6.1.

This ECM system has the abilities of controlled electrolyte flow, controlled vibration frequency and amplitude, controlled square pulsed DC output and programmable tool feeding. The developed system consists of various sub-components, e.g. micro workpiece vibration unit, controllable pulsed DC system, programmable feeding system, electrolyte circulation system, and ECM cell with flash guard, etc. The main sub-components of the ECM system (Figure 6.1) are listed in Table 6.1 and are detailed in Appendix B. Equipment used in this experiment detail are illustrated in Appendix B.

1. Part of the data reported in this chapter is reprinted from “Flushing Enhancement with Vibration and Pulsed Current in Electrochemical Machining” by Zhujian Feng, Jesus Manuel Orona-Hinojos, Pedro Perez-Villanueva, Paul Lomeli, and Wayne Nguyen Hung, 2017, International Journal of Engineering Materials and Manufacture, 2(4), 67-85, Copyright [2017] by Name of Deer Hill Publishing.

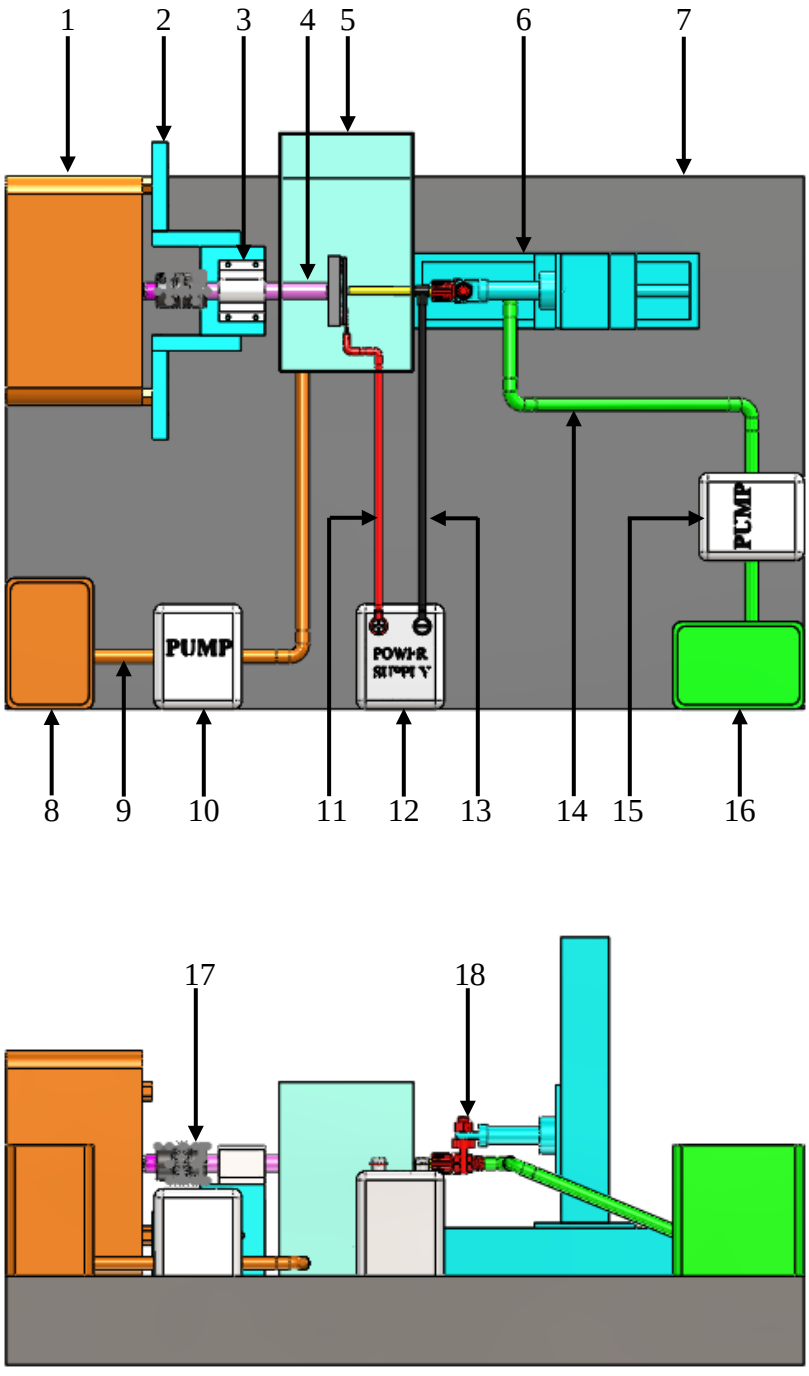

Figure 6.1 Front and top views of the horizontal ECM system.

Table 6.1 ECM set-up components.

1	Labworks electrodynamic shaker	10	Longer WT600-2J peristaltic pump
2	Bearing housing	11	Positive electric wire (to workpiece)
3	Linear bearing	12	Everlast 255EXT power supply
4	Stainless steel shaft	12	Negative electric wire (to electrode)
5	ECM cell with flash guard housing	14	Fresh-electrolyte tube
6	3-axis Velmex positioner	15	Longer WT600-2J peristaltic pump
7	Granite table	16	Fresh-electrolyte container
8	Used-electrolyte container	17	Shaft coupling
9	Used-electrolyte tube	18	Cathodic electrode holder

6.2 Experiments

Appendix B shows details of experimental equipment. In this study, the constant concentration of potassium bromide (KBr, 1mol/L) was selected as electrolyte. Each experimental run was started with electrolyte temperature in the range 21-29°C. Temperature of the electrolyte was measured and recorded by OMEGA HH374 4-channel data logger thermometer. Electrolyte conductivity, measured before each run using the Hannah HI 8733 conductivity meter, was in the range of 111-121 mS/cm. During experimental, fresh electrolyte was pumped from fresh electrolyte container (#16, Figure 6.1) and flowed inside the cathodic electrode (#4, Figure 6.1). After machining, used electrolyte in the ECM cell (#5, Figure 6.1) was pumped out and stored in used electrolyte

container (#8, Figure 6.1). Although the metallic by-products in used electrolyte could be filtered using centrifugal method in small quality, the settling method was used for a large quantity of used electrolyte. In the latter method the used electrolyte, mixed with metal debris and by-products, was stored overnight so that the heavy metallic and salt-byproduct would be settled at the contained bottom. The clear electrolyte at the top was pump back to the fresh electrolyte container (#16, Figure 6.1) using a Longer WT600-2J peristaltic pump (#15, Figure 6.1) and reused for subsequent experiment if its conductivity was still comparable with that of the fresh electrolyte.

Stainless steel tubes (ϕ9.5 mm OD, 0.3 mm thick, #4 in Figure 6.1) were selected as cathodic electrode. About 13 mm ends were commercially coated with Teflon to form a nonconductive layer of 0.02 mm thick on both outside and inside diameters. The coated ends were carefully sanded off using 600-grit abrasive paper to make the cathodic electrode tube conductive.

The emphasis on fuel economy and passenger safety had led to a remarkable increase in the usage of high strength low alloy (HSLA) steel in automobile application. The ECM was selected to machine holes on HSLA steels, such as Domex 550 steel. The chemical compositions of 1018 steel and Domex 550MC HSLA steel are slight different (Table 6.2), but the cumulative specific removal rate for these alloys are almost the same, as listed in Equation (6.1) and (6.2). Physical and mechanical properties of the 2 steels are shown in Table 6.3. Therefore, in this investigation, the 1018 steel, instead expensive Domex

550MC HSLA steel, was milled to rectangular workpiece ($50 \times 60 \times 3.5$ mm) and substituted for the ECM experiments.

Table 6.2 Chemical composition of 1018 steel and Domex 550MC HSLA steel. [77]

Materials	Mass %
1018 steel	98.8-99.3 Fe, 0.14-0.2 C, 0.6-0.9 Mn
Domex 550MC	97.5 Fe, 1.80 Mn, 0.12 C, 0.1 Si, 0.15 Ti, 0.2 V

Table 6.3 Physical and mechanical properties of 1018 steel.
*Estimated values from similar alloys [78]
** Estimated values from similar alloys [77]

Properties	1018 steel	Domex 550MC
Density (g/cm^3)	7.87	8.13
Hardness (Brinell)	126	550
Melting temperature (°C)	1450-1510	1520
Shear strength (MPa)	330	371
Tensile strength (MPa)	440	660
Specific heat (J/g/°C)	0.486	0.434
*Thermal conductivity (W/m°K)	53.6	41
*Thermal diffusivity (mm^2/s)	14.7	1.6
** Electrical resistivity (Ωm)	15.9×10^{-8}	17×10^{-8}

$$C_{Domex} = \sum_{i=1}^{n} C_i \times w_i = 3.63 \times 10^{-2} \frac{mm^3}{As} \quad (6.1)$$

$$C_{1018} = \sum_{i=1}^{n} C_i \times w_i = 3.67 \times 10^{-2} \frac{mm^3}{As} \quad (6.2)$$

The higher peak current leads to a higher MRR but it also increases the possibility of sparks which can damage the cathodic electrode and the anodic workpiece. To avoid potential spark damage, peak current was limited to 26 A in this study and current frequency was set to 500 Hz since a high current frequency produced a high MRR [11]. Vibration frequency and vibration amplitude were chosen as variables to investigate their influence on flushing condition, listed in Table 6.4.

Table 6.4 Vibration frequency and vibration amplitude in experiments.

#	Vibration Frequency (Hz)	Vibration Amplitude (μm)
1	0	0
2	20	5.00
3	20	7.50
4	20	10.00
5	30	5.00
6	30	7.50
7	30	10.00
8	40	5.00
9	40	7.50
10	40	10.00
11	60	4.44
12	80	2.50

The TENMA 72-6202 multimeter was used to measure the conductivity between the cathodic electrode and the anodic workpiece. The Velmex computer controlled positioner was used to set the initial inter-electrode gap. At first, the multimeter was used to find the location of the cathodic electrode where in contact with the anodic workpiece since the resistance between the cathodic electrode and the anodic workpiece dropped to 0 (IEG = 0). After that, the cathodic electrode moved back 0.3mm and controlled by the Velmex

positioner. In this investigation, a constant feed rate was set to 15μm/s and the cathodic electrode traveled a distance of 2.5 mm.

After ECM'ed, all samples were rinsed and cleaned with water in an ultrasonic bath for 1 minute and then dried with compressed air. All samples were positioned in a grass beaker in the bath with ECM'ed holes facing down to facilitate removal of residual particles from the hole. The Alicona Infinite Focus 3D profiler, was used to analyze the ECM'ed machined depth, surface finish and wall taper angle.

The settled by-products, were collected and washed with distilled water 10 times to remove the dissolved potassium bromide. Two samples of by-products were prepared for SEM and EDX. The sample for SEM was one drop of by-products solution placed on the titanium plate and dried in air. Thin Au-Pd layer was sputtered coated on the surface of the titanium and specimens. The Tescan Vega 3 SEM was used to capture the surface image of the by-products. The ECM sediment was washed, dried, and deposited on a carbon tape. The Zeiss EDX was used to analysis the by-products compositions.

7 RESULTS AND DISCUSSIONS[1]

In this section, the effects of vibration amplitude and vibration frequency on average flushing speed are illustrated with simulation results. Identification of the ECM by-products, hole profile, relationship between average flushing speed, and machining depth/taper angle are also demonstrated.

7.1 By-products

The SEM image of the ECM by-products is shown in Figure 7.1. Although the particles are coagulated to different shapes, the single particles have different sizes in the range 0.5-4 μm. It is assumed for simplicity that the particle is spherical with average size of ~2 μm. An EDX spectrum on dried particles on carbon tape (Figure 7.2) suggests that the by-products are iron hydroxide, since iron, carbon and oxygen are dominating elements. Elements of the KBr electrolyte are absent after the by-products are repeatedly rinsed in deionized water.

1. Part of the data reported in this chapter is reprinted from "Flushing Enhancement with Vibration and Pulsed Current in Electrochemical Machining" by Zhujian Feng, Jesus Manuel Orona-Hinojos, Pedro Perez-Villanueva, Paul Lomeli, and Wayne Nguyen Hung, 2017, International Journal of Engineering Materials and Manufacture, 2(4), 67-85, Copyright [2017] by Name of Deer Hill Publishing.

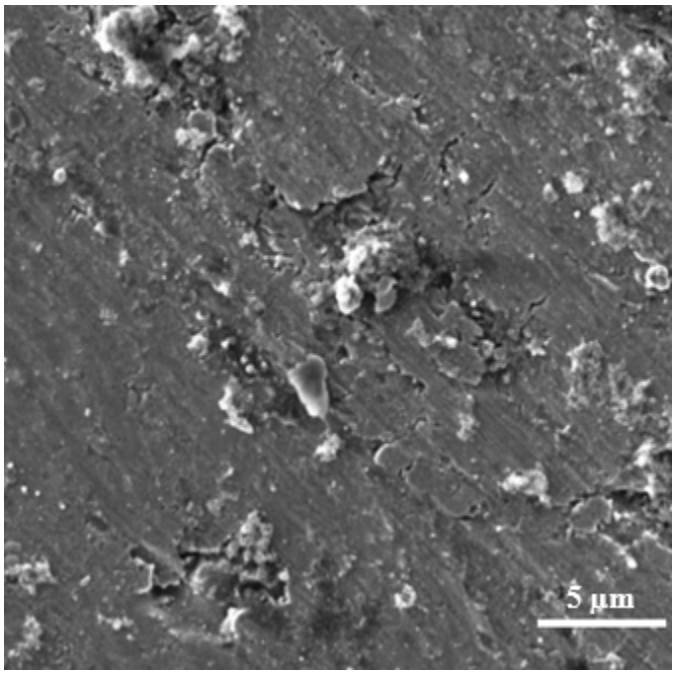

Figure 7.1 SEM image of the dried ECM by-products on a titanium plate.

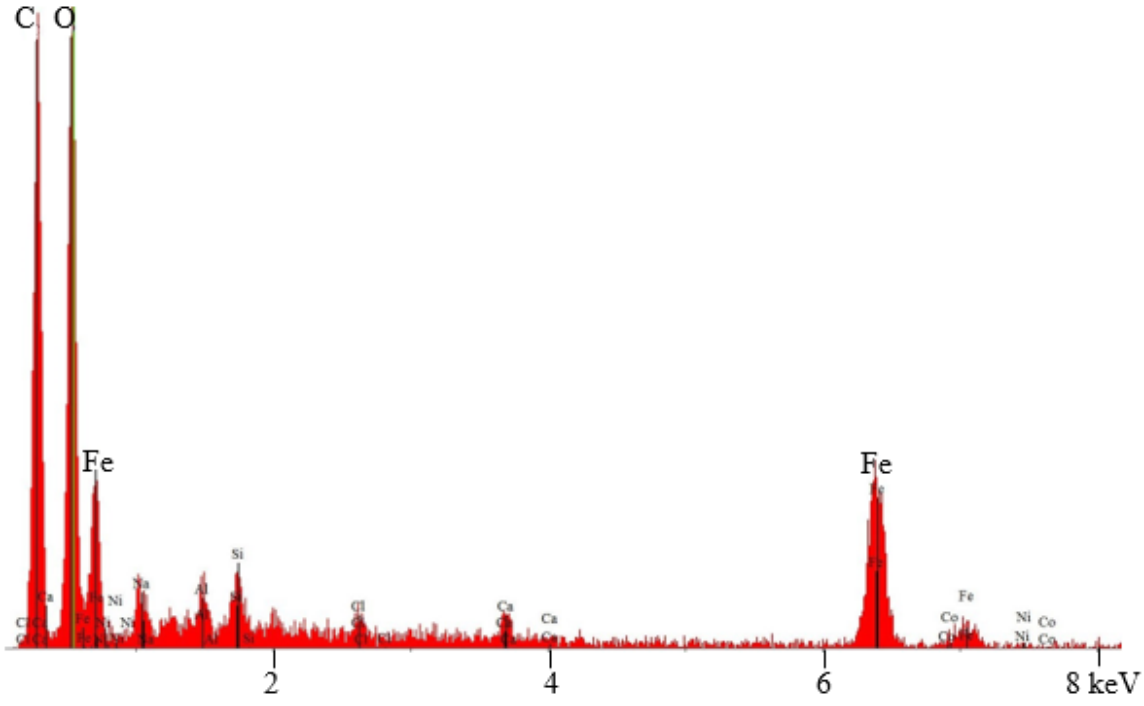

Figure 7.2 EDX spectrum of the ECM by-products on carbon tape.

7.2 Multiple Particles Interaction by Star CCM+ Simulations

Figure 7.3 illustrates the initial conditions of the simulation. The color bar demonstrates the “Particle Residence Time”. Figure 7.3a shows the anodic workpiece in the yz plane. Four green points, I, II, III and IV, represent the particle injection locations (referring to the previous Figure 5.5 and Table 5.2). The enlarged view of location A is shown in Figure 7.3b. Figure 7.3c is the side view of Figure 7.3b in the xy plane.

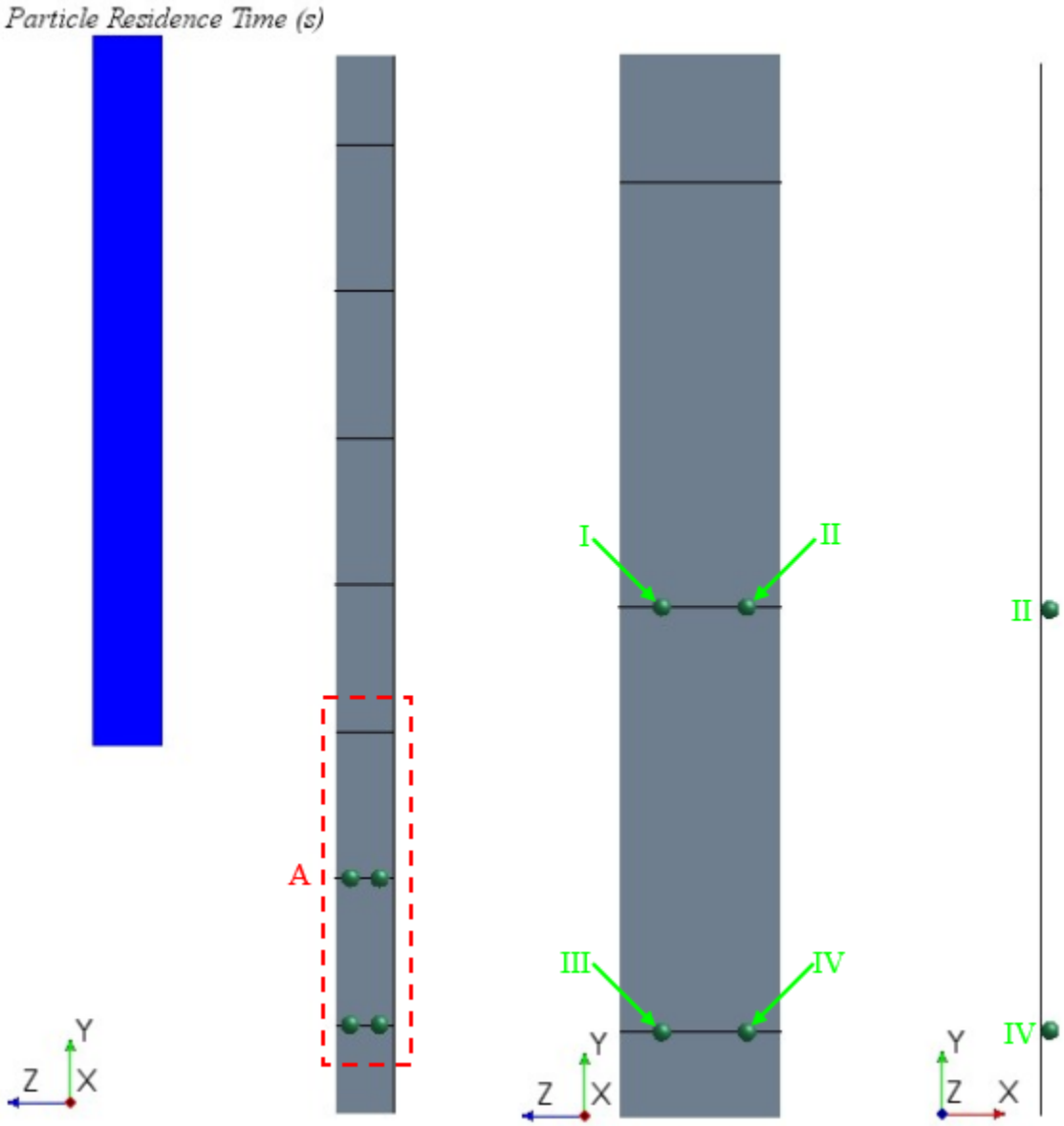

Figure 7.3 The Star CCM+ simulation results at $t_0 = 0$ µs.
(a) workpiece in the xy plane; (b) enlarged view of section A; and (c) side view of (b) in the yz plane

In this section, $P_{X,i}(t_j)$ is introduced to represent the particle's location in simulation domain.

where

$X = I, II, III, IV$: particle injection location

$i = 1,2,3, \dots, n$: particle injection order

$j = 1,2,3, \dots, n$: injection time.

For example, $P_{IV,1}(t_1)$, represents the 1st particle released at location IV and its location at time t_1. For simplification, only the right side (locations II & IV) is presented since there is no interaction of particles releasing from II and IV locations with these from I and III locations. At time $t_1 = 1\ \mu s$, $P_{IV,1}(t_1)$ is rejected and its location is illustrated in Figure 7.4. Figure 7.4 also demonstrates that the particle is contact with the anodic workpiece's surface, since particle is released from the workpiece's surface.

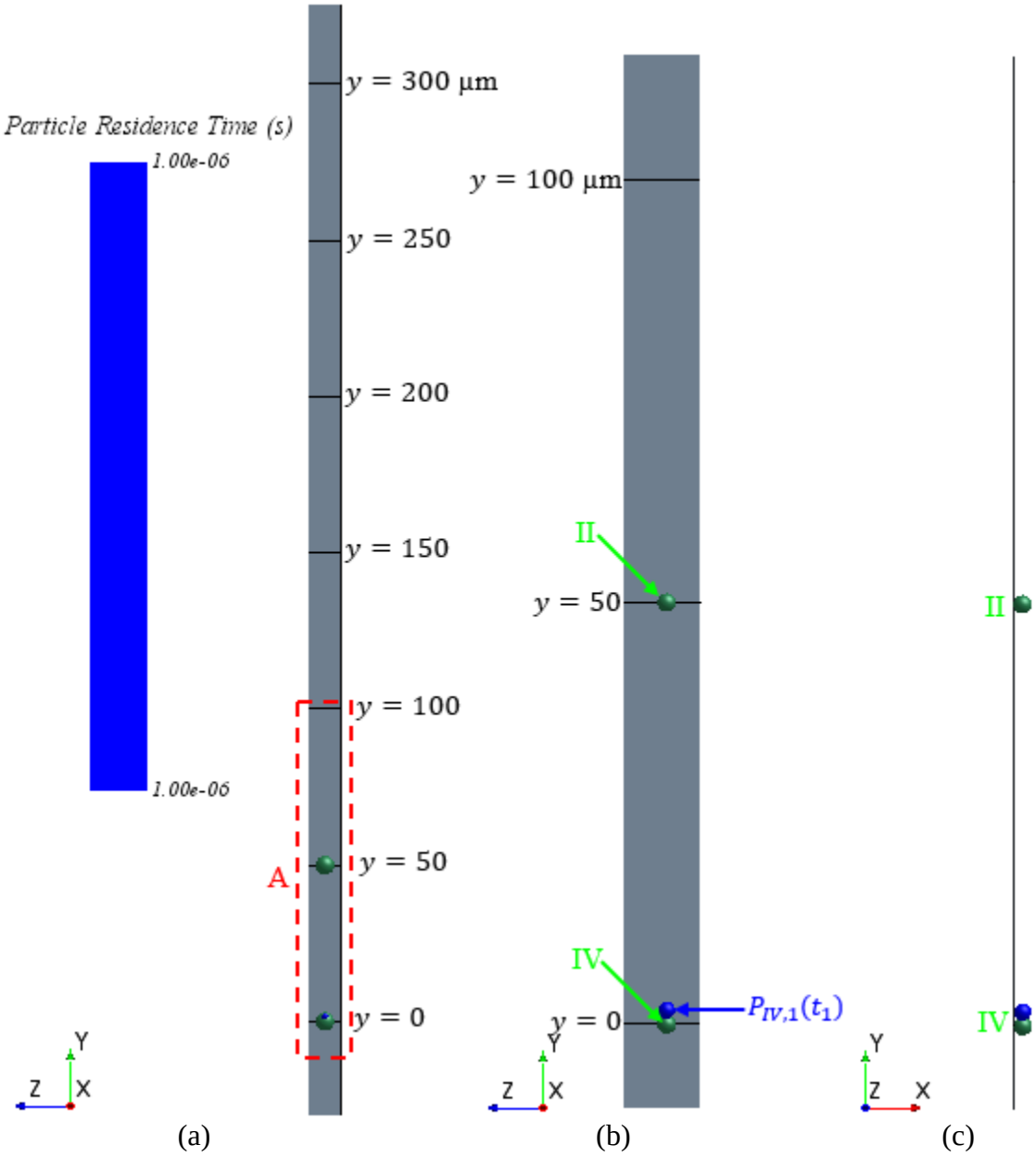

Figure 7.4 The Star CCM+ simulation results at $t_1 = 1$ µs.
(a) workpiece in the xy plane; (b) enlarged view of section A; and (c) side view of (b) in the yz plane

Particle $P_{IV,2}$ is injected into simulation domain at time $t_2 = 71$ μs, represented as $P_{IV,2}(t_2)$ in Figure 7.5. At this time, particle $P_{IV,1}$'s location is represented as $P_{IV,1}(t_2)$ and also illustrated in Figure 7.5. Similarly, particle $P_{IV,3}$ is injected at location IV at time $t_3 = 81$ μs, represented as $P_{IV,3}(t_3)$ in Figure 7.6.

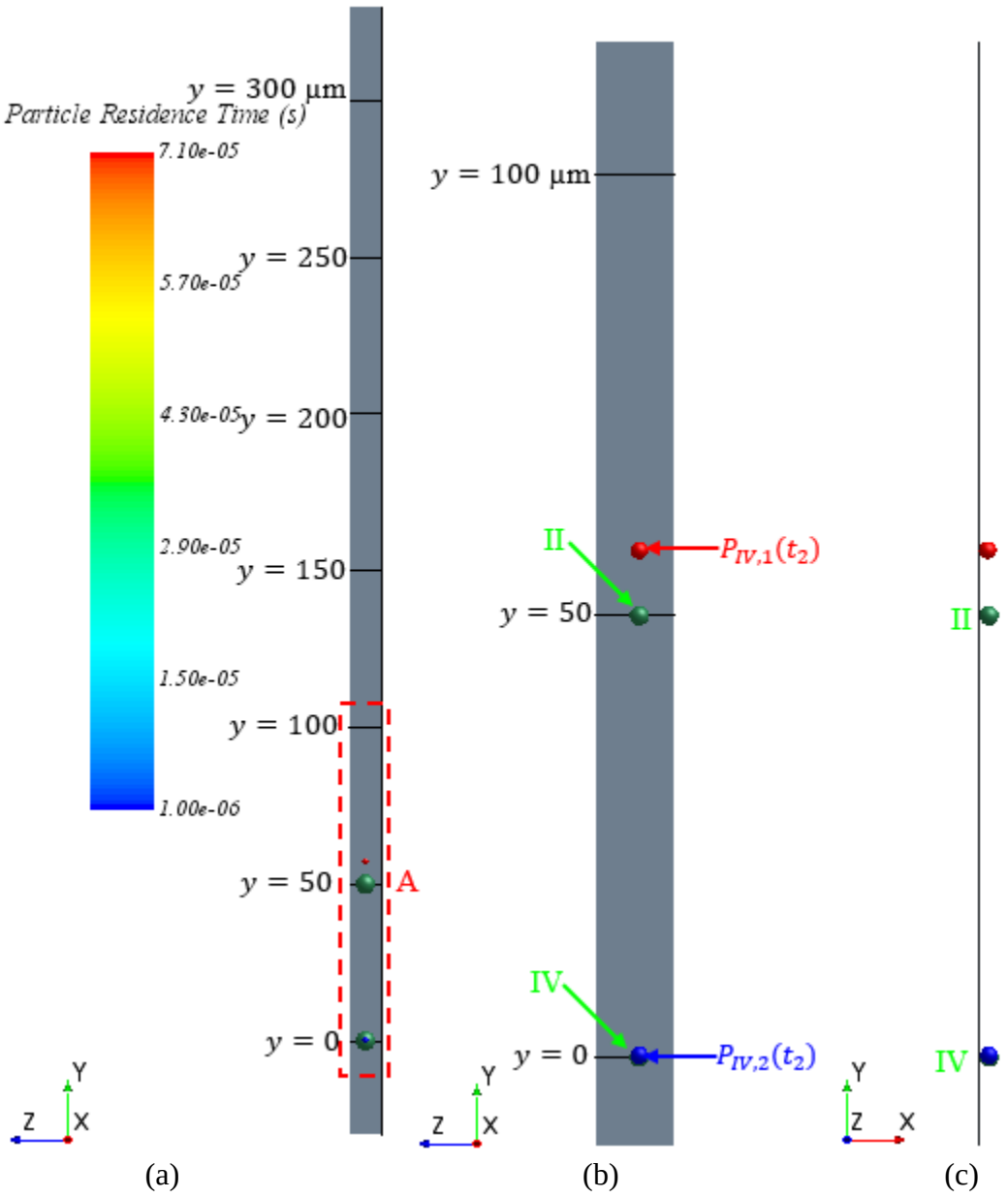

Figure 7.5 The Star CCM+ simulation results at $t_2 = 71$ µs.
(a) workpiece in the xy plane; (b) enlarged view of section A; and (c) side view of (b) in the yz plane

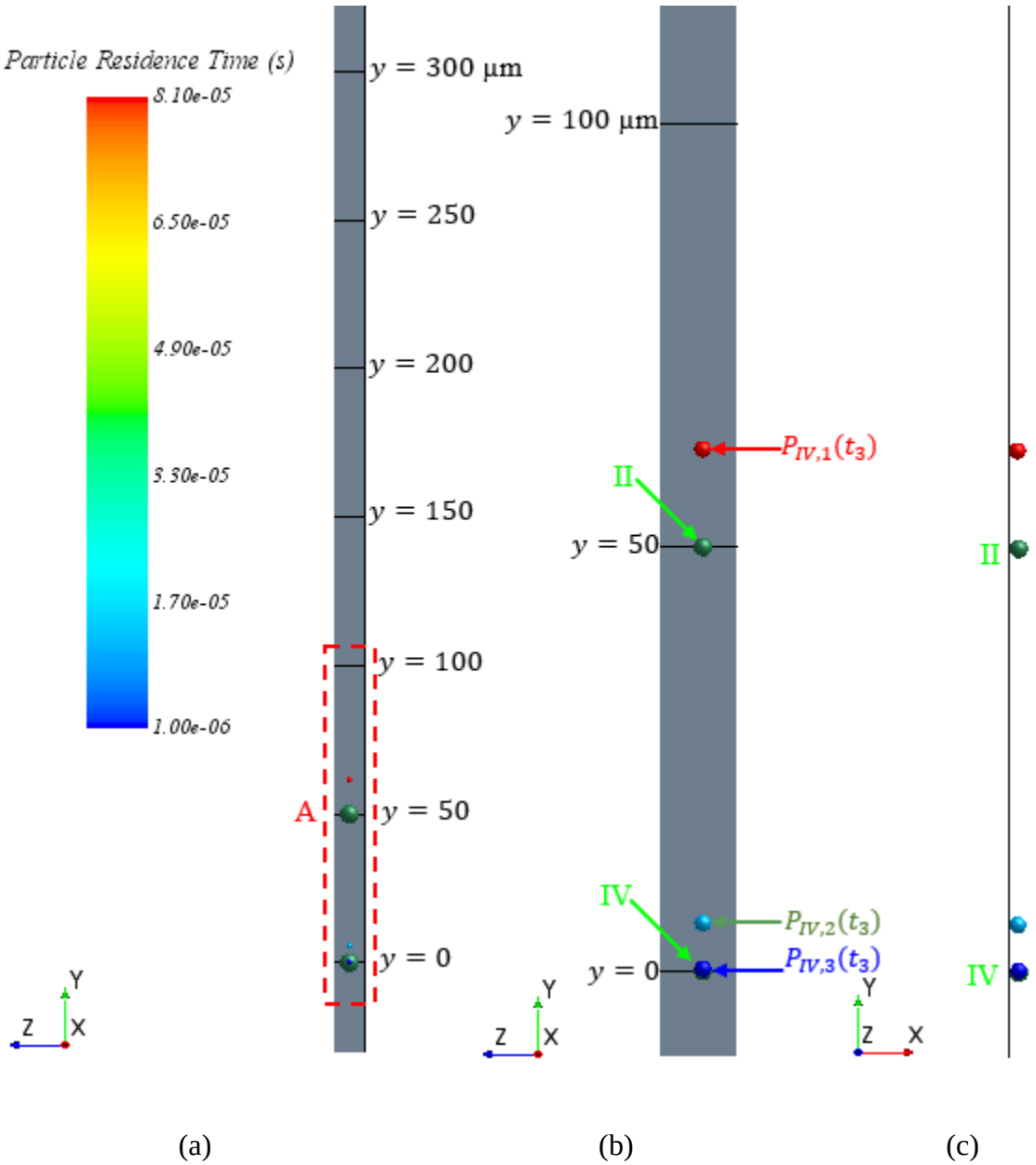

(a) (b) (c)

Figure 7.6 The Star CCM+ simulation results at $t_3 = 81$ µs.
(a) workpiece in the xy plane; (b) enlarged view of section A; and (c) side view of (b) in the yz plane

The enlarged views of same location A (Figures 7.3 - 7.6) in the yz plane at time $t_4 = 91$ µs, $t_5 = 141$ µs and $t_6 = 151$ µs are shown in Figure 7.7. Particle $P_{II,4}$, $P_{II,5}$ and $P_{II,6}$ are injected from location II at $t_4 = 91$ µs, $t_5 = 141$ µs and $t_6 = 151$ µs, respectively.

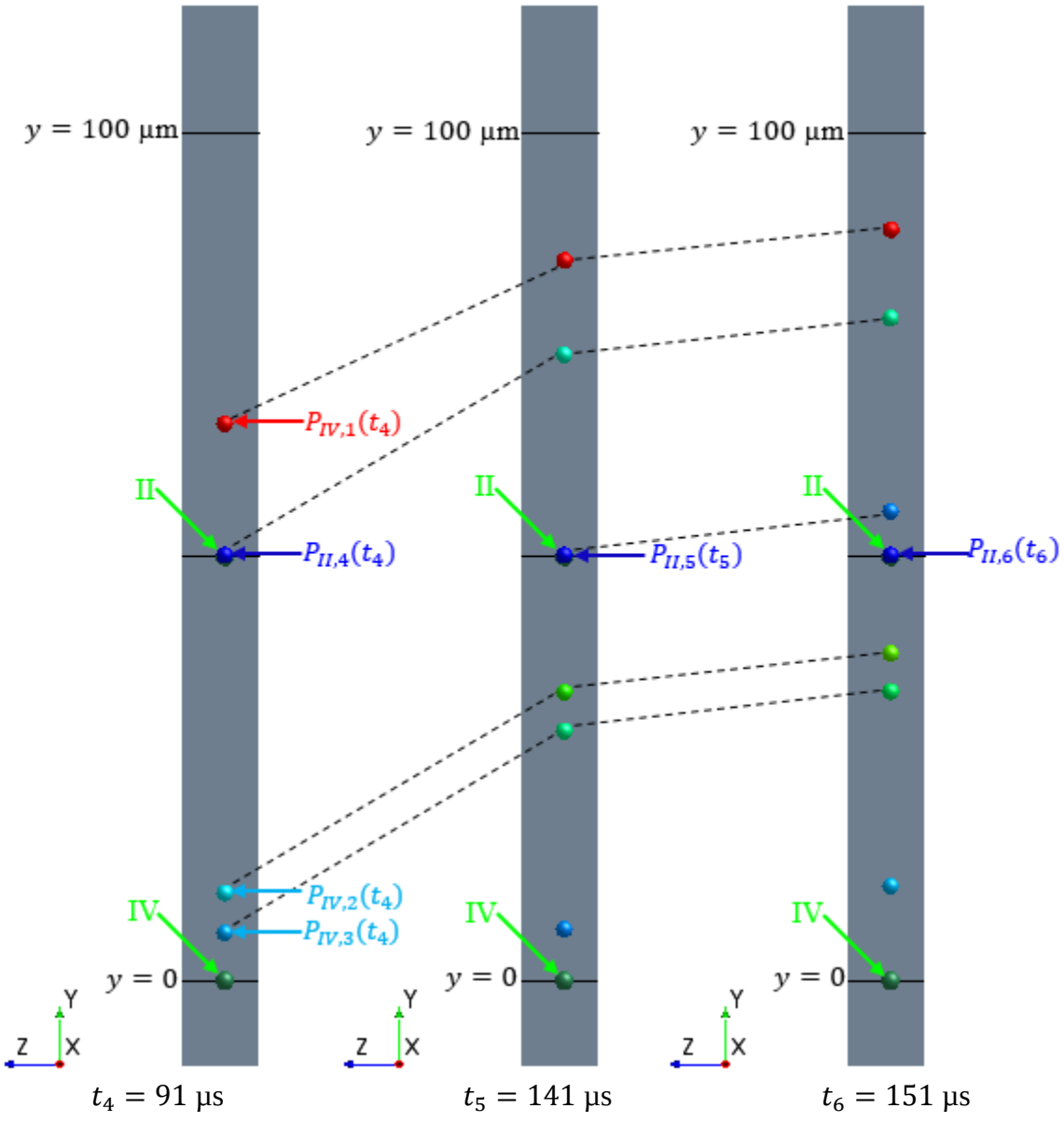

Figure 7.7 The Star CCM+ simulation results at $t_4 = 91$ µs, $t_5 = 141$ µs and $t_6 = 151$ µs.

At time $t_7 = 211$ µs, the last interested particle $P_{II,7}$ is injected at location II, as shown in Figure 7.8. Particles $P_{X,1-7}$'s location are represented as $P_{IV,1}(t_7)$, $P_{IV,2}(t_7)$, $P_{IV,3}(t_7)$, $P_{II,4}(t_7)$, $P_{II,5}(t_7)$, $P_{II,6}(t_7)$ and $P_{II,7}(t_7)$ and are shown in Figure 7.8.

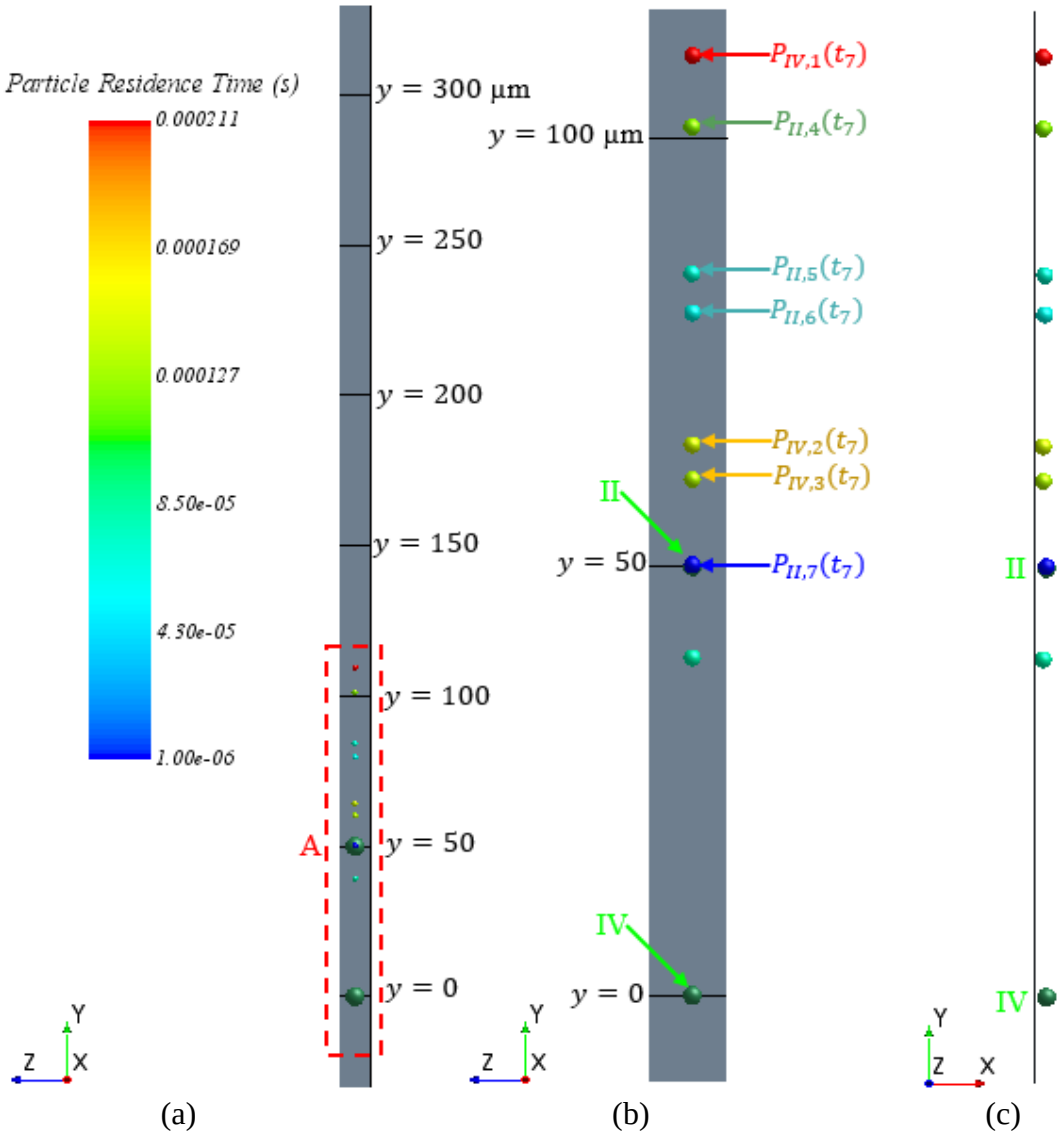

Figure 7.8 The Star CCM+ simulation results at $t_7 = 211$ µs.
(a) workpiece in the xy plane; (b) enlarged view of section A; and (c) side view of (b) in the yz plane

As simulation continues, at $t_8 = 272$ µs, there is collision between the particles $P_{II,7}$ and $P_{IV,3}$, as shown in Figure 7.9.

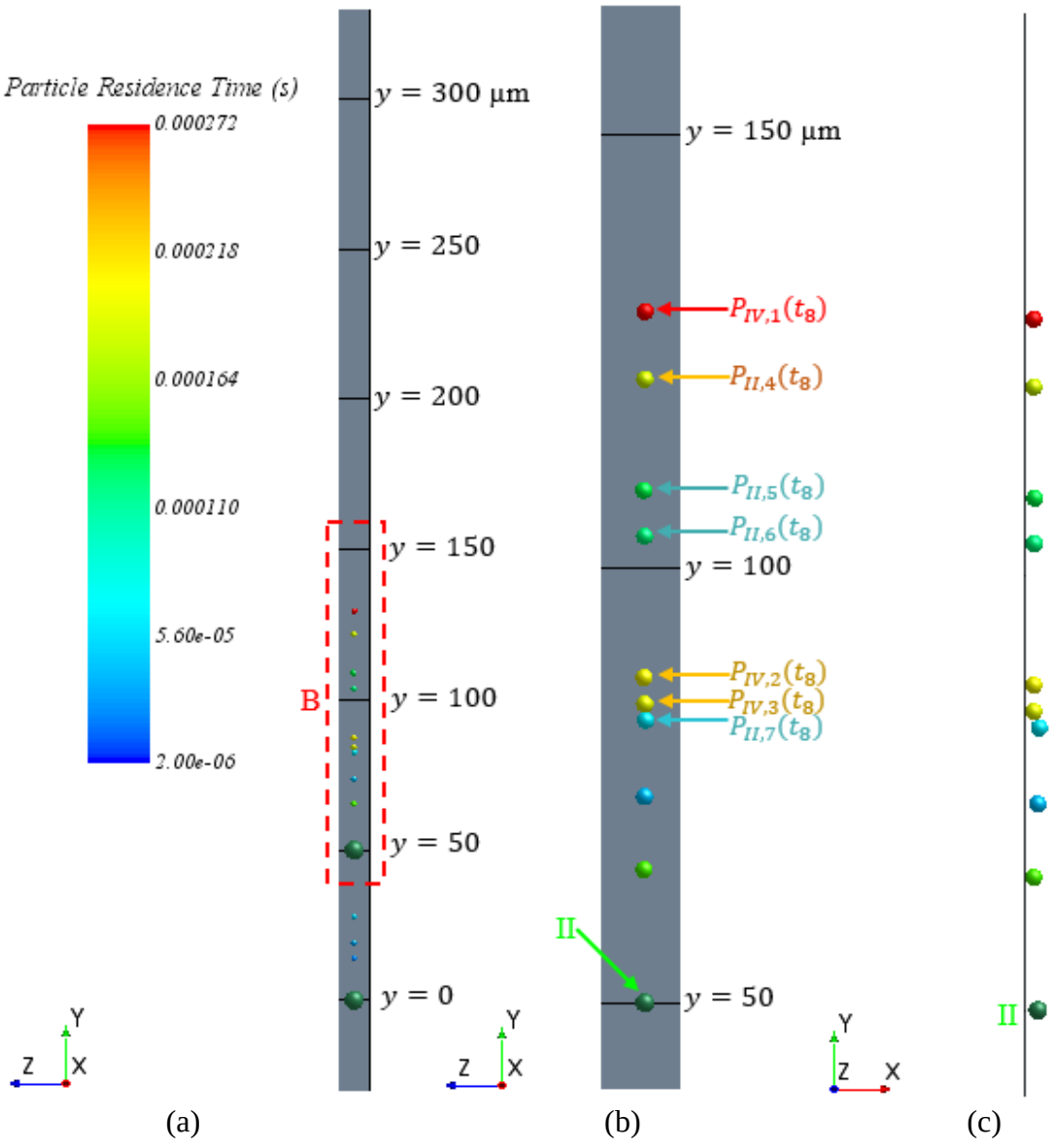

Figure 7.9 The Star CCM+ simulation results at $t_8 = 272$ µs.
(Collision of $P_{II,7}(t_8)$ and $P_{IV,3}(t_8)$)
(a) workpiece in the xy plane; (b) enlarged view of section B; and (c) side view of (b) in the yz plane

Figure 7.10 illustrates the particle collisions between particle $P_{IV,2}$, $P_{IV,3}$ and $P_{II,7}$ in the xy plane at location B (in previous Figure 7.9).

- At time $t_8 = 272$ μs, the particle $P_{II,7}$ impacts the particle $P_{IV,3}$. After the collision, the particle $P_{IV,3}$ obtains an acceleration along the y-direction and the flow speed along y-direction is increased. The particle $P_{II,7}$ obtains an acceleration along the x-direction and it moves toward the cathodic electrode, while it continue moves along y-direction due to the drag effect of the fluid.
- At time $t_9 = 280$ μs, the particle $P_{IV,3}$ impacts the particle $P_{IV,2}$. After the collision, particles $P_{IV,3}$ and $P_{IV,2}$ will combined and move together. The particle $P_{II,7}$'s speed along the y-direction is increasing due high electrolyte flow speed.
- At time $t_{10} = 287$ μs, there are collisions occur between particle $P_{IV,2}$, $P_{IV,3}$ and $P_{II,7}$ and the particle $P_{II,7}$ passes the particle $P_{IV,3}$.
- At time $t_{11} = 291$ μs, the particle $P_{II,7}$ passes the particle $P_{IV,2}$, and continue passes the particle $P_{II,6}$.
- At time $t_{12} = 322$ μs, the particle $P_{II,7}$ impacts the particle $P_{II,5}$ and continue moves along the y-direction.
- At time $t_{13} = 353$ μs, the particle $P_{II,7}$ has already passed the particle $P_{II,4}$ and the simulation results are shown in Figure 7.11.

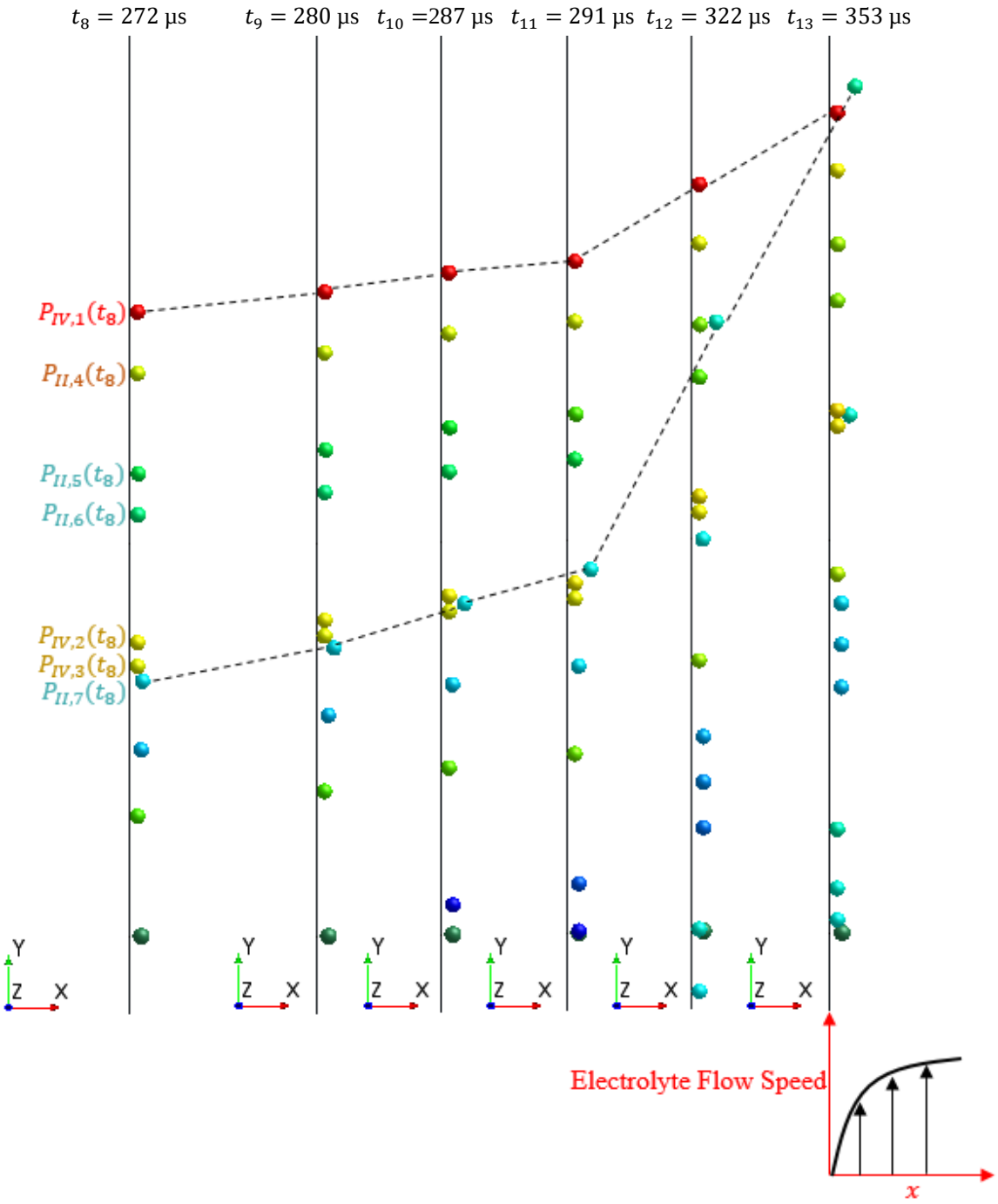

Figure 7.10 Illustration of particle collisions at location B from $t_8 = 272$ μs to $t_{13} = 353$ μs.

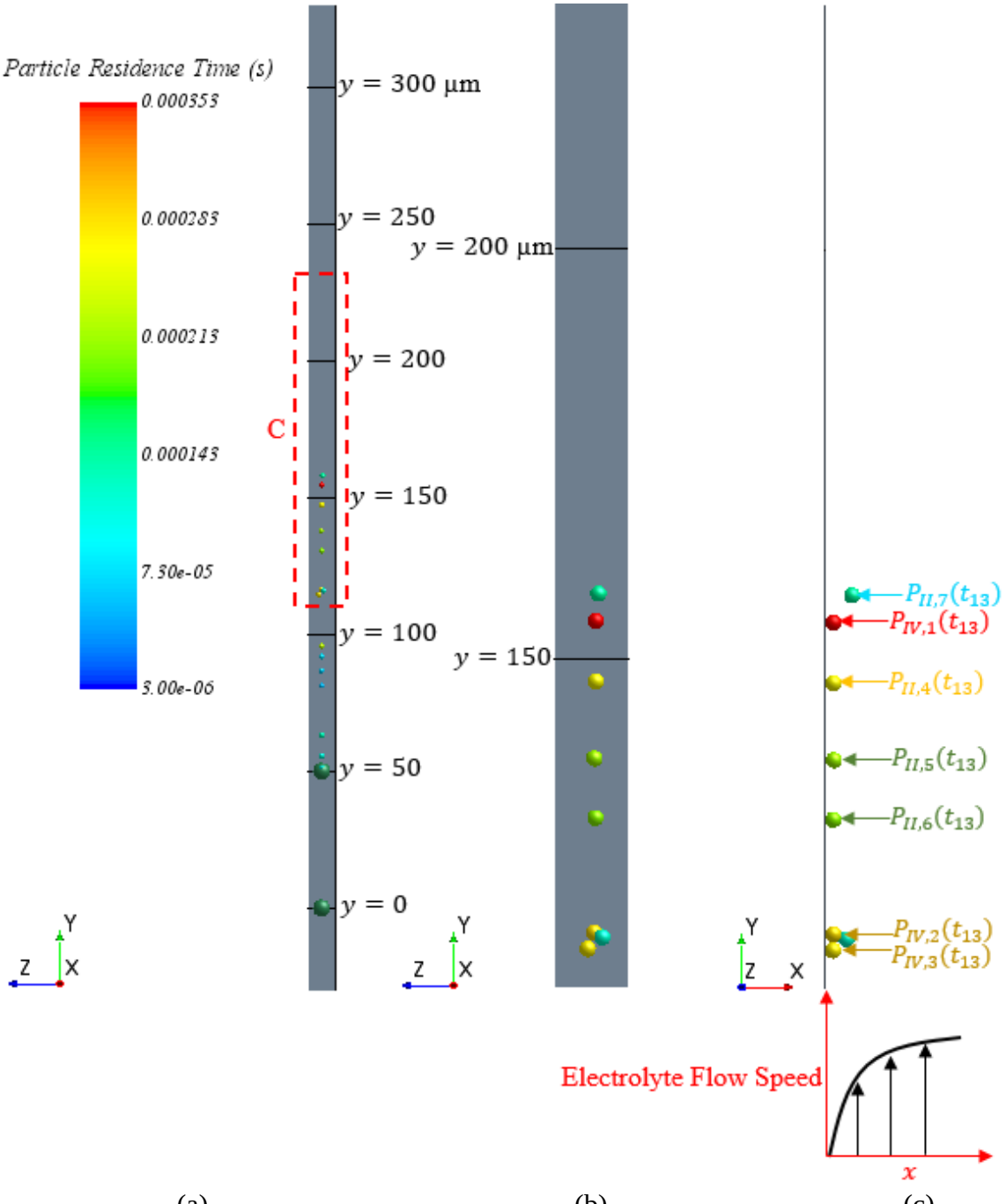

(a) (b) (c)

Figure 7.11 The Star CCM+ Simulation results at $t_{13} = 353$ µs.
(a) workpiece in the xy plane; (b) enlarged view of section C; and (c) side view of (b) in the yz plane

Figure 7.12 demonstrates the particle $P_{II,7}$ flushing process in the domain of location C (in previous Figure 7.11) from $t_{13} = 353$ μs to $t_{15} = 430$ μs. Clearly, the flushing speed of particle $P_{II,7}$ is greater than the particle $P_{IV,1}$'s flushing speed since the distance between the particle $P_{II,7}$ and the anodic workpiece is larger than the distance between the particle $P_{IV,1}$ and the anodic workpiece. The locations of the particles $P_{X,1-7}$ at $t_{13} = 353$ μs are represented as $P_{X,1-7}(t_{13})$ respectively and are illustrated in Figure 7.12.

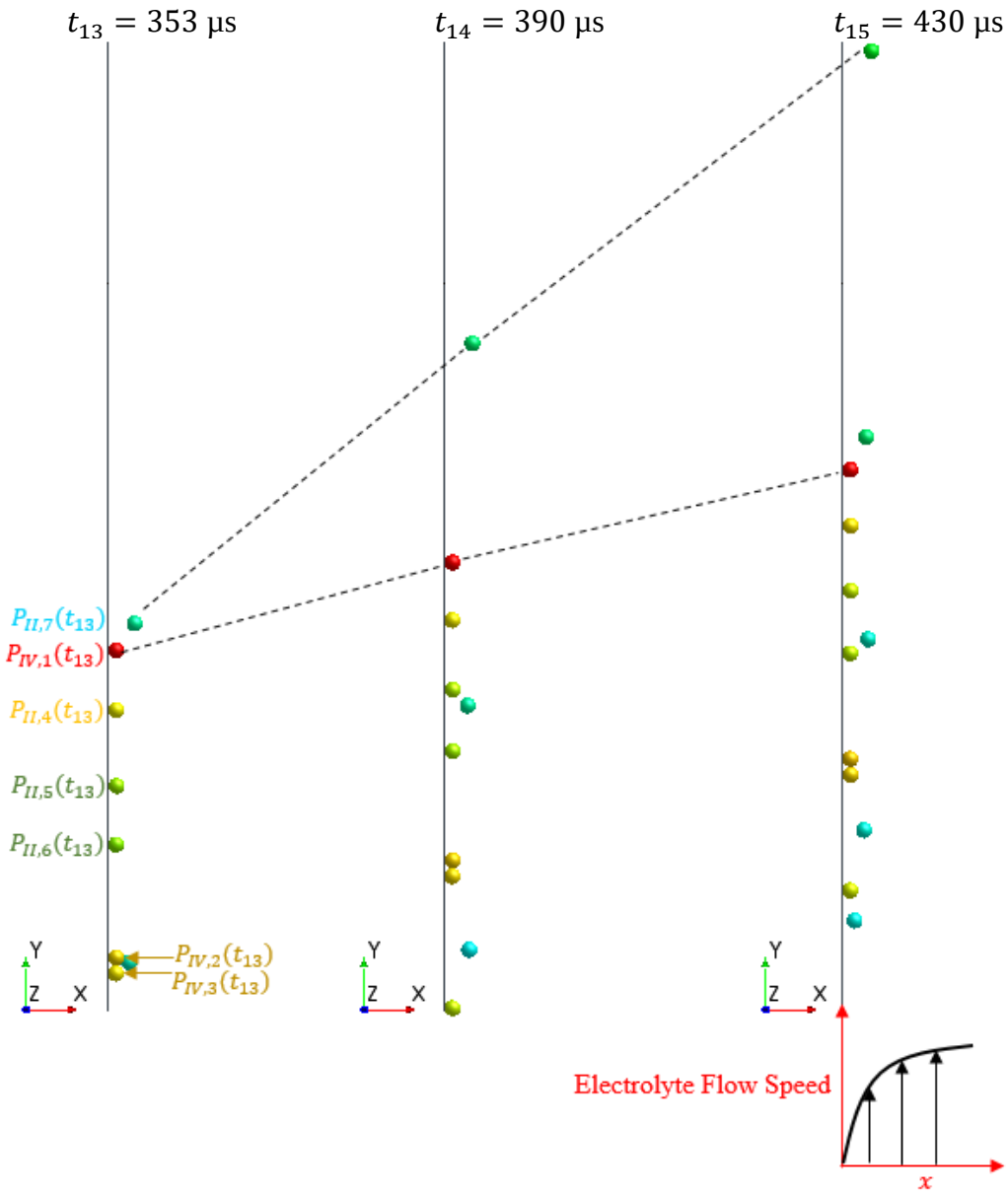

Figure 7.12 Particle $P_{II,7}$ flow process in location C from t_{13} = 353 μs to t_{15} = 430 μs

At time t_{16} = 512 μs, the y coordinate of $P_{II,7}$ is larger than 300 μm, which means that the particle is flushed away from the interested simulation domain. The simulation results are shown in Figure 7.13.

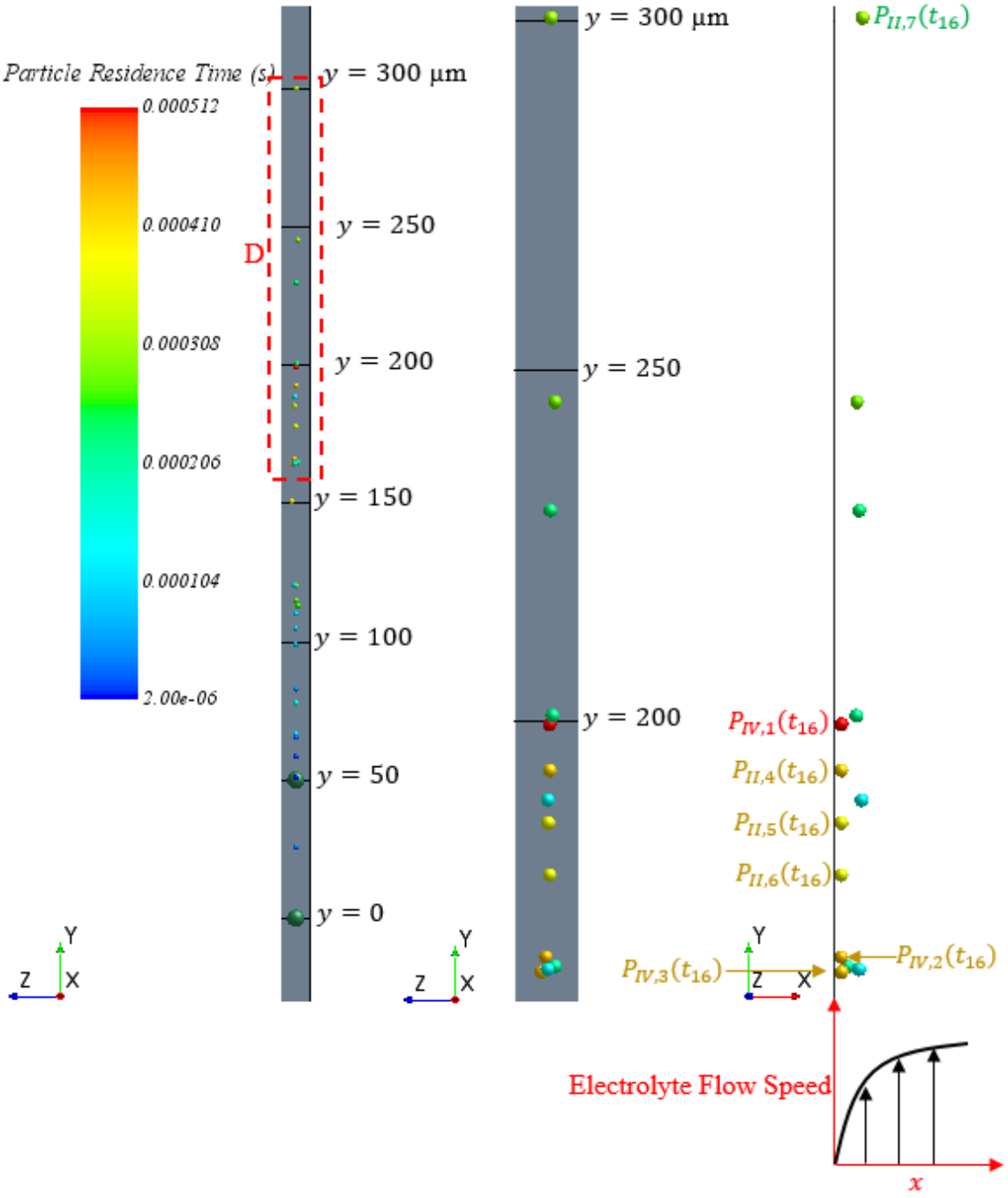

(a) (b) (c)

Figure 7.13 The Star CCM+ simulation results at $t_{16} = 512$ µs.
(a) workpiece in the xy plane; (b) enlarged view of section C; and (c) side view of (b) in the yz plane

Figure 7.14 illustrates the particles $P_{X,1-6}$ flushing process from $t_{16} = 512$ μs to $t_{19} = 850$ μs at location D.

- At time $t_{16} = 512$ μs, particle $P_{IV,2}$ obtains an acceleration along the x - direction due to a collision and then its speed is larger than the particle $P_{IV,3}$'s speed. Hence, these two particles are separated and move independently.
- At time $t_{19} = 940$ μs, the particle P_1's y - coordinate is larger than 300 μs, as shown in Figure 7.15. There is no interaction of particles releasing from II and IV locations with these from I and III locations. Thus, it is reasonable to use the right side of the workpiece to analysis the multiple particles flushing process.

The average flushing speed of the particle $P_{IV,1}$ is:

$$V_{ave} = \frac{300\ \mu m}{940\ \mu s} = 0.319\ m/s \tag{7.1}$$

In the following section, a single particle flushing away process will be simulated using the ANSYS Fluent software. This Star CCM+ simulation results will be compared with the Fluent simulation results.

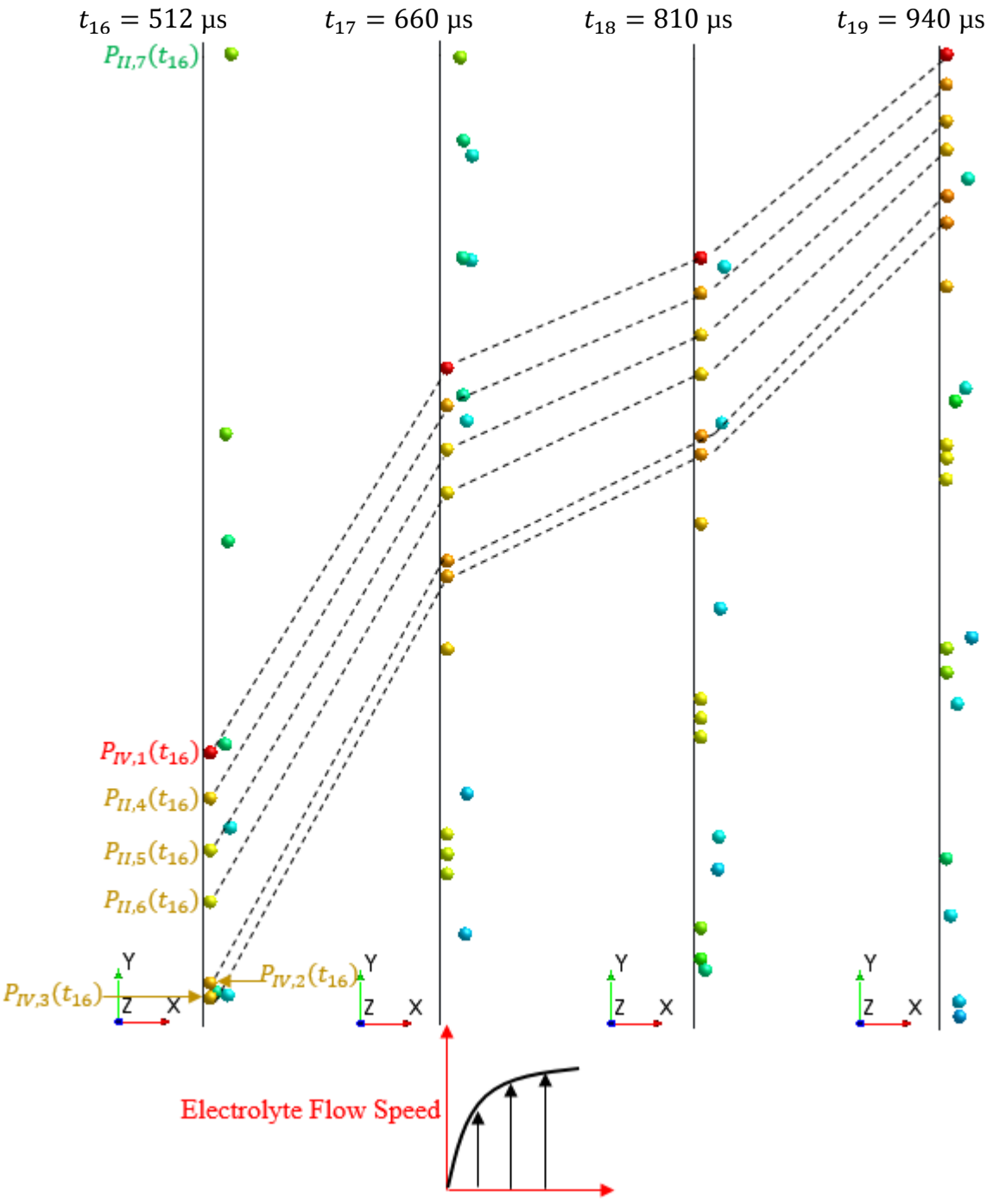

Figure 7.14 The Star CCM+ simulation results from $t_{16} = 512$ µs to $t_{19} = 940$ µs

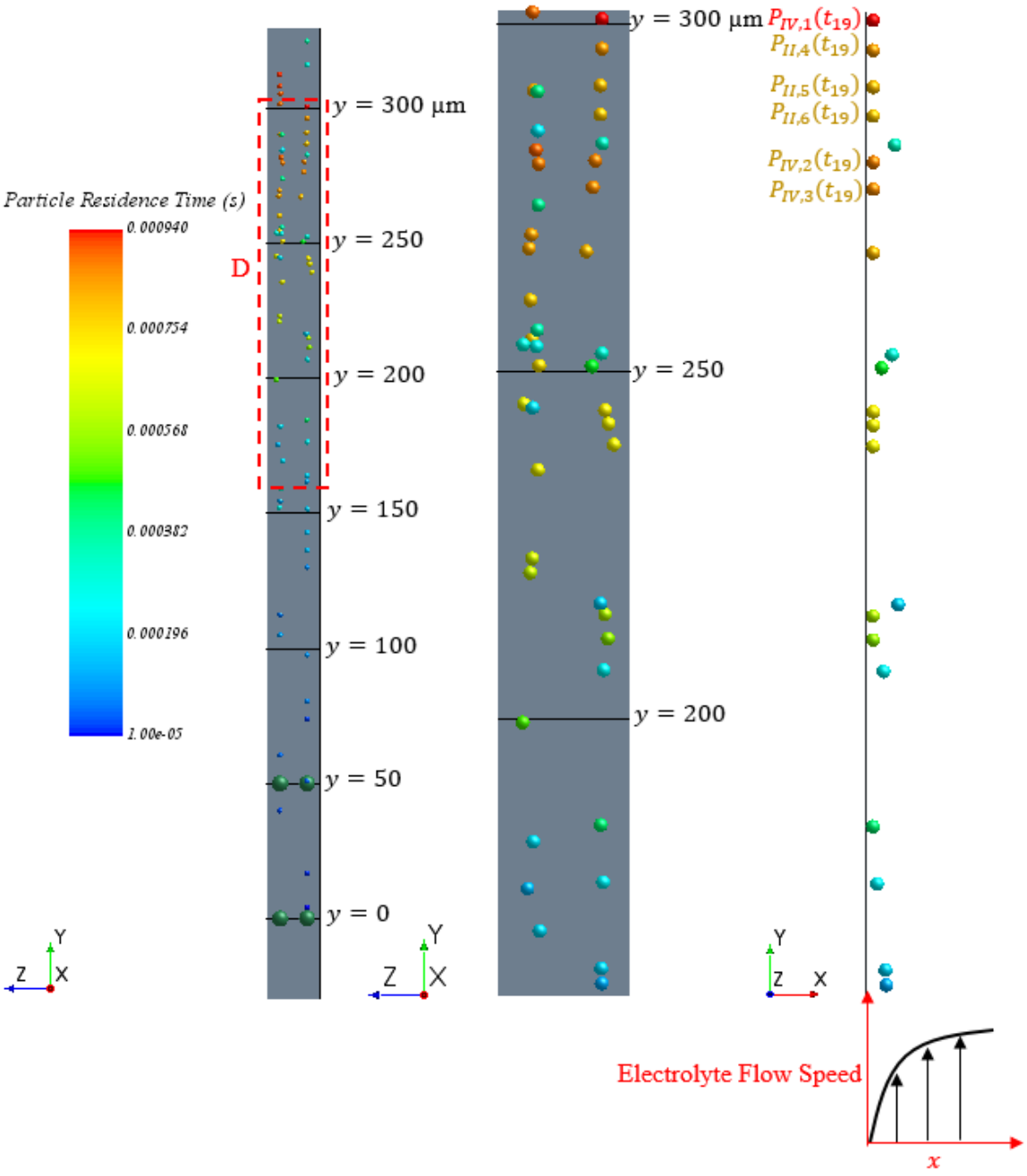

(a) (b) (c)

Figure 7.15 The Star CCM+ simulation results at $t_{19} = 940$ µs.
(Particles releasing at 4 locations: I, II, III, and IV)
(a) workpiece in the xy plane; (b) enlarged view of section D; and (c) side view of (b) in the yz plane

7.3 Simulation of Average Flushing Speeds by ANSYS Fluent Simulations

Recall that the simulation cell is $g_0 \times w_t = 300 \times 300$ µm (Figure 7.16a), and a simulation will be terminated if the y-coordinate of a particle center is larger than 300 µm. A typical particle moves along the y-direction is shown in Figure 7.16b. Average flushing speed, V_{ave}, is defined as the secant slope of particle path:

$$V_{ave} = \frac{\text{particle travel distance}}{\text{time}} = \frac{300\ \mu m}{756\ \mu s} = 0.396\ m/s \tag{7.2}$$

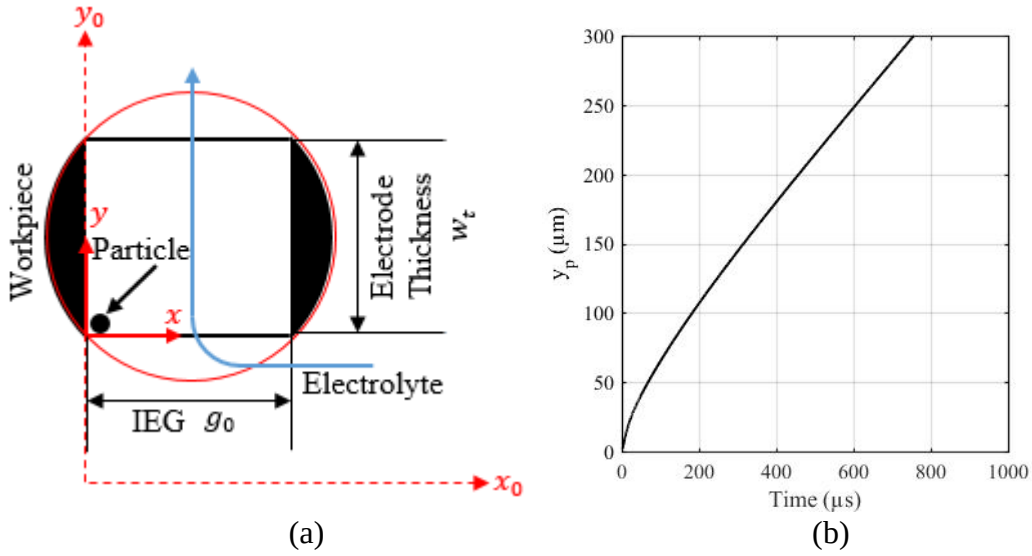

(a) (b)

Figure 7.16 Particle movement in the y-direction.
(Simulation with ANSYS Fluent at f = 40 Hz, $A_v = 10$ µm and $V_e = 4$ m/s)

Recall that the average flushing speed of a particle was simulated by the Star CCM+ to be 0.319 m/s, which is close to that the single particle simulation result $V_{ave} = 0.396 m/s$ at

40 Hz vibration frequency and 10 μm vibration amplitude. Therefore, it is reasonable to use the single particle to simulate the particle movement in the IEG.

The effect of vibration frequency on average flushing speed at $I_{vibration} = 7A$ is shown in Figure 7.17. The average flushing speed decreases with increasing vibration frequency. Neglecting the effect of the workpiece vibration on the particle movement along the cathodic electrode x-direction, the distance between workpiece and the particle center is given in Equation (7.3) and illustrated in Figure 7.18.

$$d_g = -A_v \sin(2\pi f t) + r_p \tag{7.3}$$

where

d_g: Gap between particle and workpiece surface ($\geq r_p$) (μm)

A_v: Vibration amplitude (μm)

f: Vibration frequency (Hz)

r_p: Particle diameter (μm)

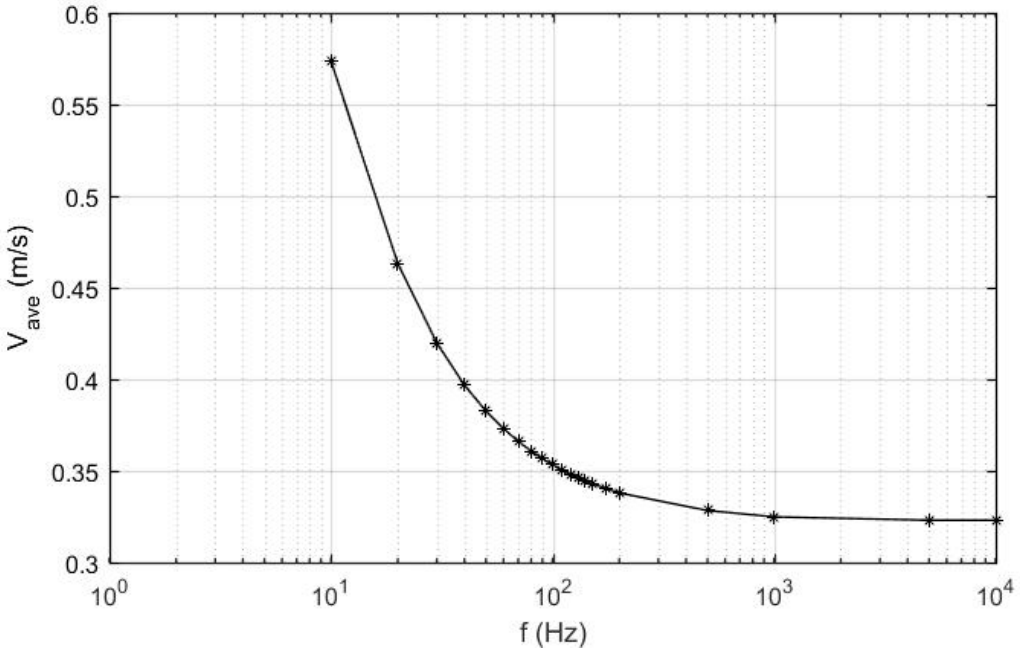

Figure 7.17 Effect of vibration frequency on average flushing speed.
(Simulation with ANALYS Fluent at $I_{vibration} = 7A$)

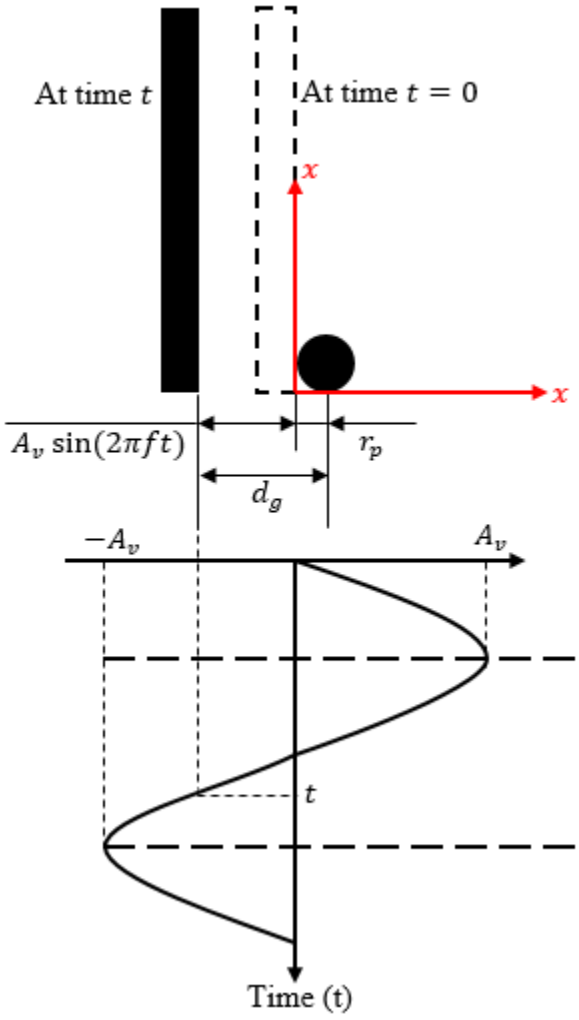

Figure 7.18 Illustration of the distance between particle center and workpiece surface.

As shown in Figure 7.17, $I_{vibration}$ is fixed at 7 A, the average flushing speed decreases from 0.5736 m/s ($f = 10$ Hz, $A_v = 160$ μm) to 0.3231 m/s ($f = 10{,}000$ Hz, $A_v = 0.16$ nm) when vibration frequency increases from 10 Hz to 10,000 Hz. For fixed vibration current or constant vibration power, the vibration amplitude and vibration frequency follow the relationship $A_v f^2 =$ constant B (from Equation (5.9)), and Equation (7.3) becomes:

$$d_g = -B\frac{\sin(2\pi ft)}{f^2} + r_p \tag{7.4}$$

Equation (7.4) suggests that the distance between particle center and workpiece d_g decreases drastically with increasing vibration frequency f. Therefore, for fixed current on vibration generator, a high vibration frequency would lead to a smaller gap, lower drag force and lower average flushing speed, as shown in Figure 7.17.

The relationship between particle size and average flushing speed is shown in Figure 7.19. As the particle radius increase from 1 μm to 3 μm, the average flushing speed increases from 0.29 to 2.77 m/s. However, continue increase particle size to 5 μm, the average flushing speed changes slightly, from 2.77 to 3.08 m/s. This is because the gap d_g in Equation (7.3) increases with an increasing of particle radius. Larger gap results in higher drag force and higher average flushing speed.

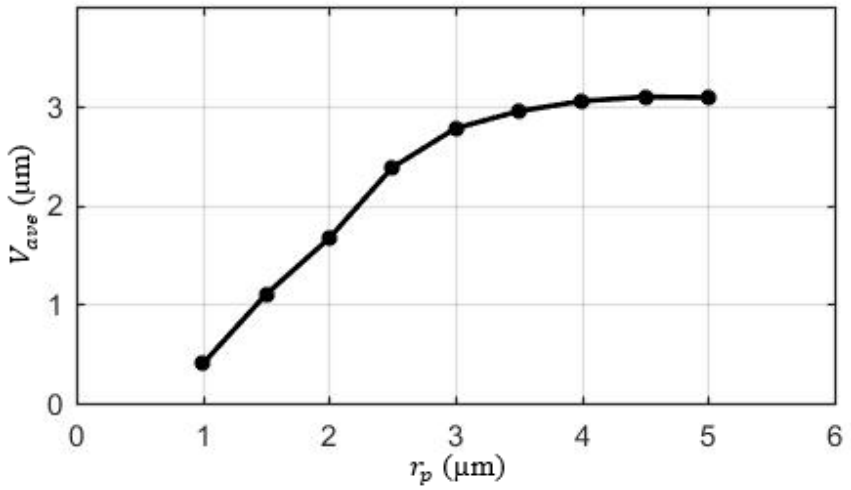

Figure 7.19 Relationship between average flushing speed and particle radius. (Simulation with ANASYS Fluent at f = 40 Hz and A_v = 10 μm and V_e = 4 m/s)

This simulation results were confirmed with experiment results conducted by Liu [69]. For a preset machining parameter combination (4 μm, 6 μm and 8 μm vibration amplitude, $\phi 160$ μm tungsten cathodic electrode with 5 μm insulate layer, 321 stainless steel workpiece with 0.5 mm thickness, 5 wt% $NaNO_3$ + 0.8 wt% EDTA-Na_2 electrolyte, 6 V voltage with 50% duty cycle, 2 KHz pulsed voltage and 15.6 μm IEG), after obtaining the maximum MRR at a 50 Hz, the MRR decreased with increasing of vibration frequency, as shown in previous Figure 3.34.

7.4 Hole Profile

The electrical field strength between a circular cathodic electrode and a flat plate can be derived [79] and schematically show in Figure 7.20. The highest field strength is along a circular ring directly below the tubular cathodic electrode; the field strength is diminishing outward and away from the tube wall, but is additive to form a pronounced peak at the tubular cathodic electrode center. The result is the strong current directly below the cathodic electrode, an average current in the central region, and a weaker stray current at positions away from the cathodic electrode. The presence of an insulating coating on the cathodic electrode side significantly reduces the stray current to improve the ECM efficiency. The resulted hole profile is captured by Alicona Infinite Focus and shown in Figure 7.21.

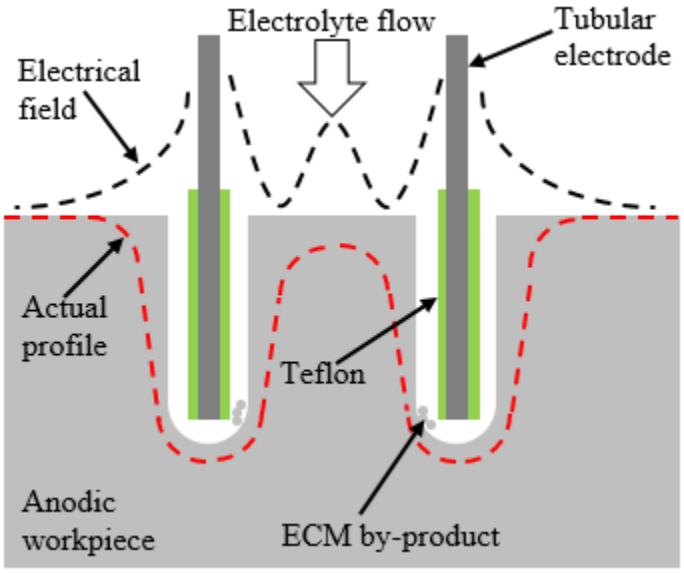

Figure 7.20 Electrical field around a tubular cathodic electrode.

Figure 7.21 Resulted profile of an ECM'ed hole.

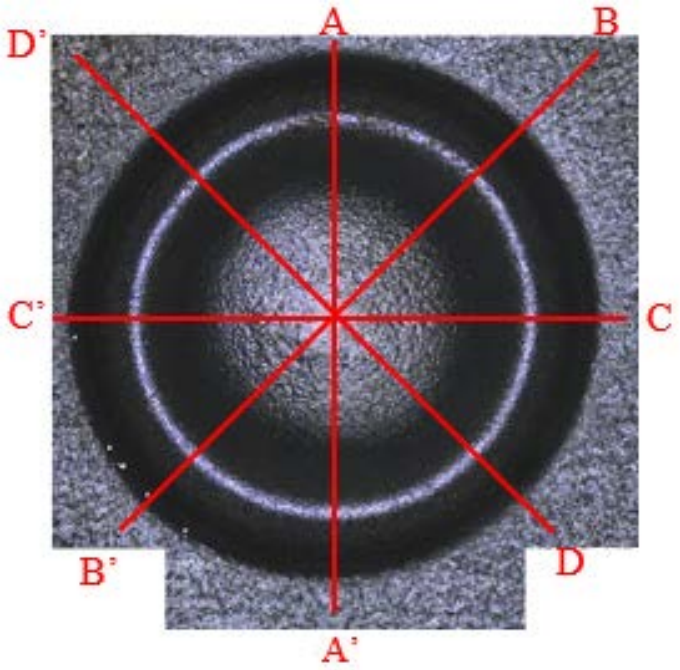

Figure 7.22 Typical 3D profile of an ECM'ed hole.
($f = 20$ Hz; $A_v = 10$ μm; $V_F = 4$ m/s)

The resulted hole profile now can be explained. Significant material is removed directly below the cathodic electrode while the corner and center position of a hole are rounded off due to weaker stray current. The agglomerated by-products particles, which collected in a small gap between the cathodic electrode and the anodic workpiece, interfere with the ion transport mechanism if they are not effectively flushed away. However, the flushed particles in fast flowing electrolyte would erode and enlarge the overcut of the ECM'ed profile, and round off the sharp entrance corners.

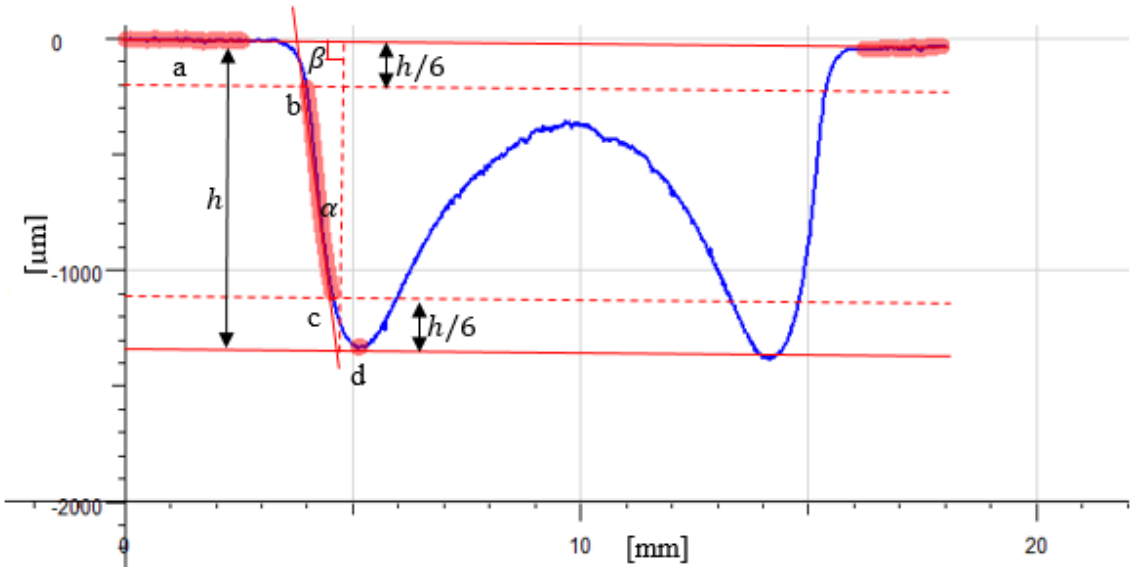

Figure 7.23 Cross-section view of an ECM's profile.
($f = 20$ Hz; $A_v = 10$ µm; $V_F = 4$ m/s)

Figure 7.22 shows a typical 3D profile measurement of an ECM'ed profile using the Alicona system, from which a cross sectional view can be constructed and analyzed (Figure 7.23). Eight locations, 45° apart, were measured for quality assessment and repeatability (Figure 7.22). The vertical distance h between top and bottom surface (a-d) is the machining depth. Neglecting the transitional curves ab and cd, the slope of line bc can be constructed which defines the corresponding hole taper angle α for quality comparison.

7.4.1 Machining Depths

The effects of vibration amplitude on average flushing speed and machining depth are demonstrated in Figure 7.24. At every vibration frequency (20 Hz, 30 Hz, and 40 Hz), a

higher vibration amplitude causes faster average flushing speed and deeper machining depth. When vibration amplitude increases from 5 µm to 10 µm, the average flushing speeds increase by 5.5% (0.3423 - 0.3610 m/s), 7.8% (0.3517 - 0.3790 m/s) and 10.0% (0.3608 - 0.3968 m/s) at respective frequency. Consequently, machining depths increase by 4% (1282 - 1336 µm), 3.7% (1311 - 1360 µm) and 20% (1319 - 1584 µm) at corresponding frequency.

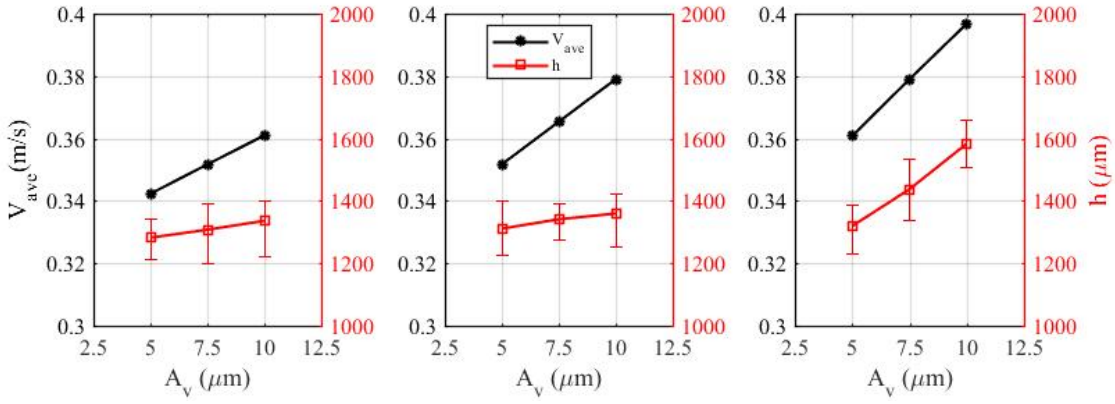

(a) $f = 20$ Hz (b) $f = 30$ Hz (c) $f = 40$ Hz

Figure 7.24 Effect of vibration amplitude on average flushing speed and machining depth.

The effects of vibration frequency on average flushing speed and machining depth are illustrated in Figure 7.25. At every vibration amplitude (5, 7.5, and 10 µm), a higher vibration frequency leads to faster average flushing speed and deeper machining depth. When vibration frequency increases from 20 to 40 Hz, the average flushing speeds increase by 5.4% (0.3423 - 0.3608 m/s), 7.8% (0.3517 - 0.3790 m/s) and 9.9% (0.3610 - 0.3968 m/s), at respective vibration amplitude. Improving of flushing speed changes

machining depths by 2.9 % (1282 - 1319 µm), 9.9% (1308 - 1437 µm) and 18.6% (1336 - 1584 µm), respectively.

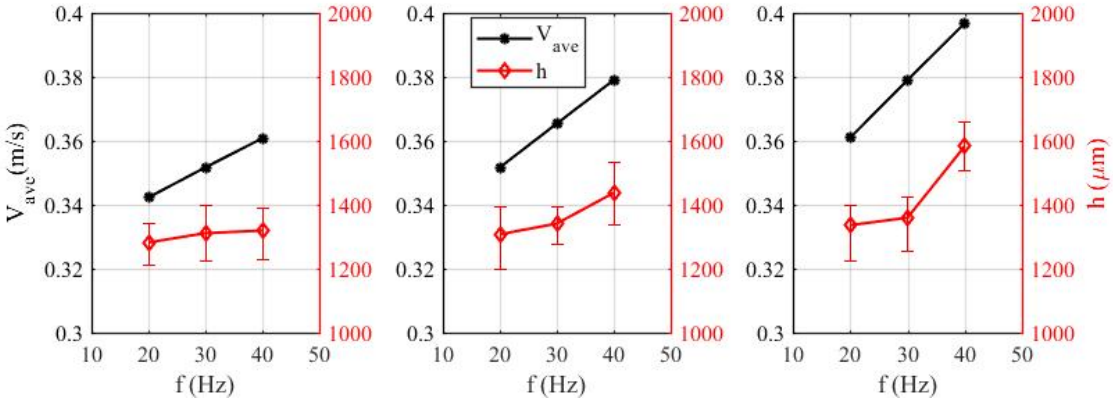

(a) $A_v = 20$ Hz (b) $A_v = 30$ Hz (c) $A_v = 40$ Hz

Figure 7.25 Effect of vibration frequency on average flushing speed and machining depth.

The relationship between average flushing speed and machining depth is shown in Figure 7.26. Due to the limitation of power supply to the vibration system, the input current can be adjusted up to 7 A at frequency $<$ 40 Hz with fixed 10 µm amplitude. This maximum current of 7 A must be maintained at frequency higher than 40 Hz with adjustable amplitudes. Simulation for frequency below and above 40 Hz shows the peak flushing average at 40 Hz while similar trend is seen for the hole depth data. There is a clear correlation between average flushing speed and machining depth.

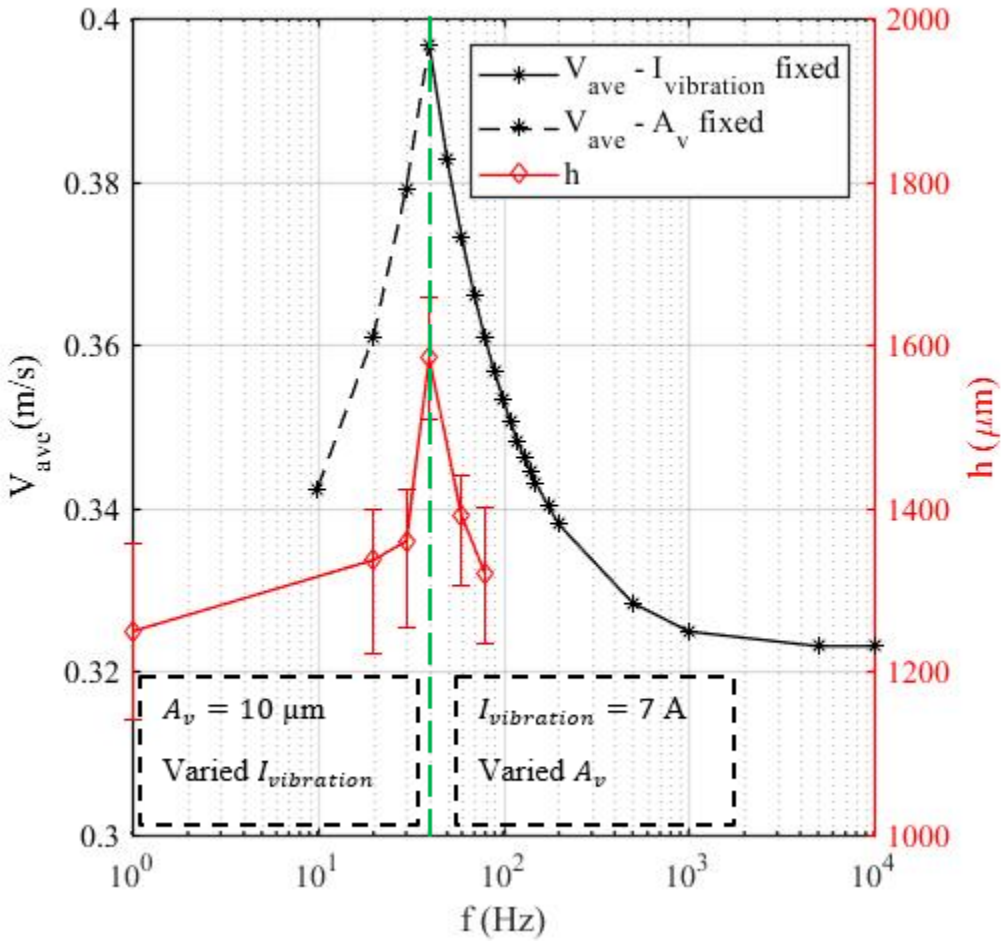

Figure 7.26 Relationship between average flushing speed and machining depth.

Low frequency vibration of workpiece enhances flushing speed, enhances ion transport rate and leads to more effective machining rate. Similar results were also reported by other publication [69]. This study used $\phi 160$ µm tungsten cathodic electrode with 5 µm insulate layer, 321 stainless steel anodic workpiece with 0.5 mm thickness, 5 wt% $NaNO_3$ + 0.8 wt% EDTA-Na_2 electrolyte, 6 V voltage with 50% duty cycle, 2 KHz pulsed voltage and 15.6 µm IEG, 3-14 µm vibration amplitude, and 50-200 Hz vibration frequency. It concluded that:

i) At any vibration amplitude (4, 6, and 8 μm), the MRR increased when increasing vibration frequency from 0 Hz to 50 Hz. However, the MRR dropped when increasing frequency further to 200 Hz.

ii) At any vibration frequency (50 Hz and 100 Hz), the MRR increased with increasing vibration amplitude in the range 0-8 μm. The maximum MRR was obtained when vibrating at 8 μm amplitude for any vibration frequency.

The maximum machining depth, therefore the highest MRR, in this study was obtained at 40 Hz workpiece vibration frequency compared to 50 Hz in other study [69]. The simulation study indicated that a higher flushing speed was expected at lower frequency (Figure 7.17), therefore, a lower frequency with larger vibration amplitude could lead to an optimal MRR. The upper bound for increasing vibration amplitude was the critical inter-electrode distance at which damaging sparks would occur due to electrical discharging. The trends from simulation and experimental data can be explained.

i) At either higher vibration frequency or vibration amplitude, more ions and by-products particles starting at the workpiece surface would be pushed toward the advancing cathodic electrode in the first half cycle, when the workpiece is reversed during the second half cycle, theses ions and particles -- physically are away from the solid workpiece surface - are subjected to higher shear and swept away in the electrolyte flow.

ii) When the ions and by-products are effectively swept away from the workpiece

surface, fresh electrolyte can be replenished to accelerate the electrochemical reactions and result in a deeper hole and a faster removal rate.

7.4.2 Taper angle

The effects of vibration amplitude on average flushing speed and taper angle are illustrated in Figure 7.27. At every vibration frequency (20, 30, and 40 Hz), a higher vibration amplitude leads to faster flushing speed and smaller taper angle – therefore, straighter and sharper hole profile. When vibration amplitude increases from 5.0 to 10.0 µm, the taper angles decreases by 8.7% (31.92 - 29.15°), 12.8% (29.32 - 25.56°) and 43.4% (29.28 - 16.57°), at respective vibration frequency.

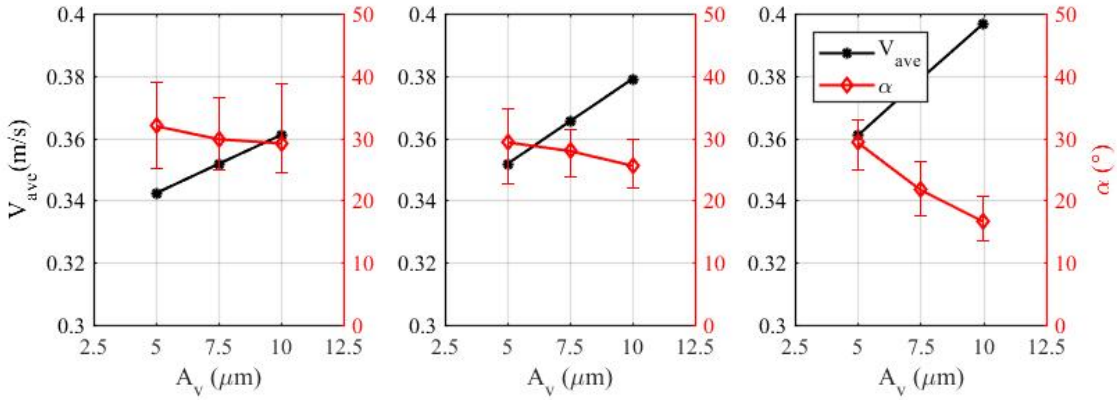

(a) $f = 20$ Hz (b) $f = 30$ Hz (c) $f = 40$ Hz

Figure 7.27 Effect of vibration amplitude on average flushing speed and taper angle.

The effects of vibration frequency on average flushing speed and taper angle are illustrated in Figure 7.28. At every vibration amplitude (5, 7.5, and 10 µm), a higher vibration frequency leads to a smaller taper angle. When vibration frequency increases from 20 to

40 Hz, the taper angles decrease by 3.4% (31.92 - 29.28°), 27.3% (29.81 - 21.67°) and 43.2% (29.15 - 16.57°) at corresponding vibration amplitude.

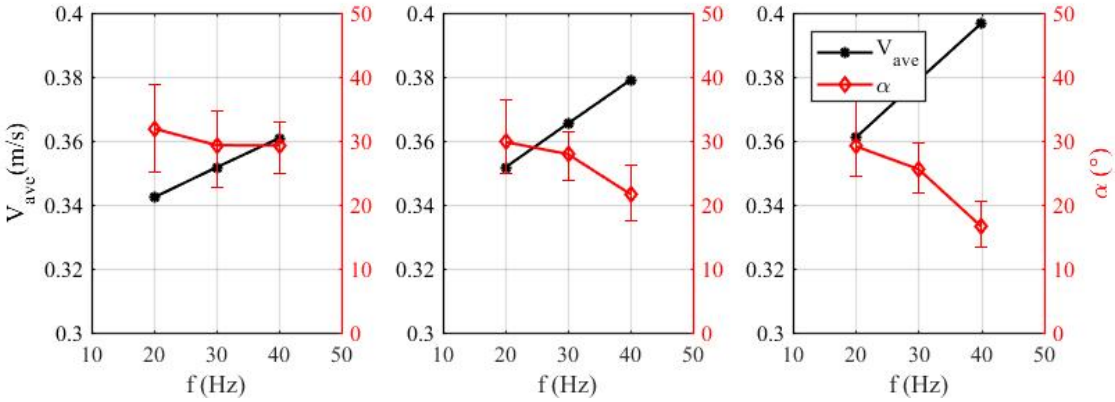

(a) $A = 5.0$ µm (b) $A = 7.5$ µm (c) $A = 10.0$ µm

Figure 7.28 Effect of Vibration frequency on average flushing speed and taper angle.

Simulation and experimental data suggest a negative correlation between average flushing speed and taper angle Figure 7.29. Authors from a different study [15] reported a similar trend on hole shape after ECM (using brass tube cathodic electrode with $\phi 8$ mm outer diameter and $\phi 3.5$ mm inner diameter, 20 g/L NaCl electrolyte, 6 L/min electrolyte flow rate, 1 mm/min cathodic electrode feed rate, 18 V applied voltage and 50 Hz vibration frequency); the conicity (slope of a cone) decreased from 3.95 to 3.25% when vibration amplitude increased from 20 to 100 µm. This trend can also be explained qualitatively:

i) Vibration of workpiece leads to a higher flushing speed that breaks up agglomerated groups of by-products into smaller chunks of particles.

ii) The smaller chunks forming between two electrodes then travel up the wall of hole and out (Figure 7.20 and Figure 7.21). The smaller coalesced particles would erode the wall less and result in smaller taper angle and sharper hole profile.

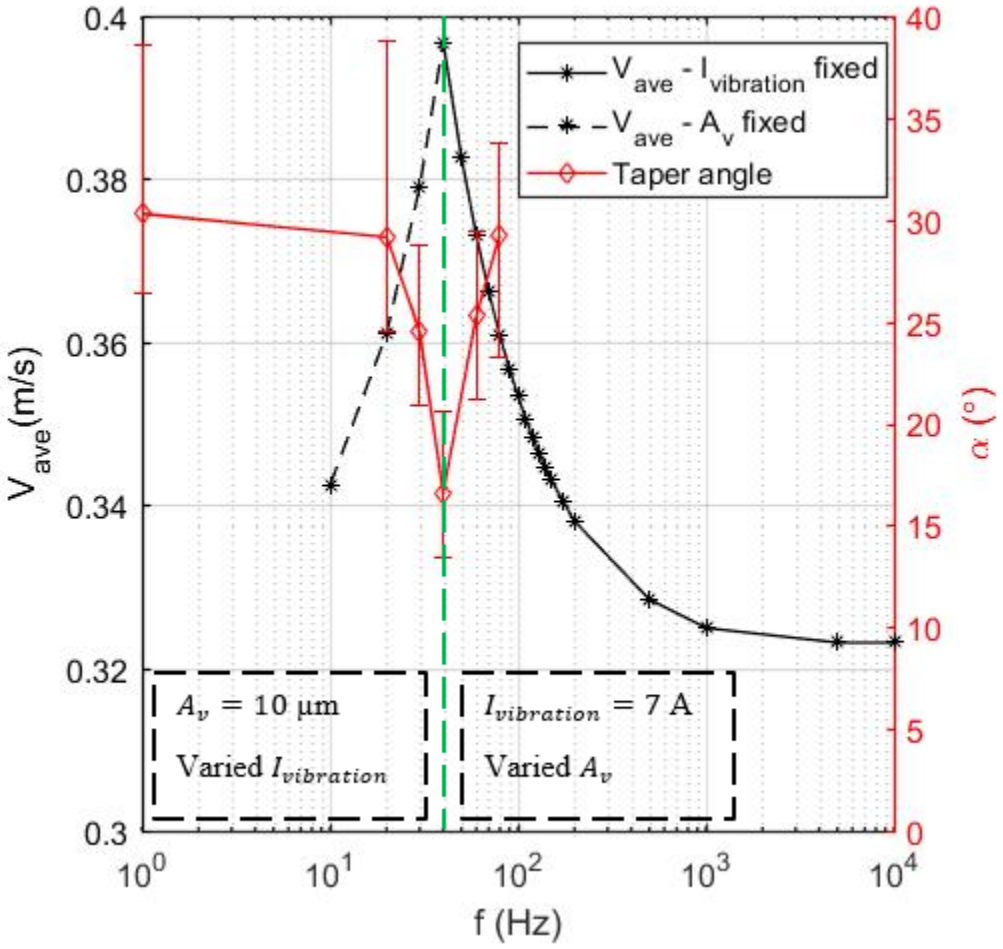

Figure 7.29 Relationship between average flushing speed and hole taper angle.

8 CONCLUSIONS AND RECOMMENDATIONS

This research theoretical investigated the mechanism of the vibration assisted pulsed ECM. ANSYS fluent and Star CCM+ are used to simulate how the ion hydroxide by-product being flushing away in the vibration assisted pulsed ECM. The simulation results and the experimental data for ECM'ing 1018 steel with pulsed current and low frequency vibration were performed on a horizontal ECM system. The dissertation shows that:

i) Theoretical analysis reveals a higher MRR will be obtained when short pulse voltage applied.

ii) In the vibration assisted ECM, theoretical analysis reveals that particle flushing speed will increase when the anodic workpiece moves away from the cathodic electrode, hence reduce the concentration of ions in double layer and leads to a larger diffusion rate and a higher MRR. On the other side, when the anodic workpiece moves toward the cathodic electrode, the resistance between the cathodic electrode and the anodic workpiece decreases, hence leads to higher potential available across the IEG and result in a higher MRR.

iii) Iron hydroxide particle with an average size of $\phi 2$ μm was the resulted by-products.

iv) Simulations of the motion of a single particle using computational fluid dynamic are performed to track the particle motion and speed between two electrodes. Flushing of the by-products is characterized by calculating of particle flushing speed when it exits inter-electrode gap. The maximum

flushing speed of ~0.4 m/s was calculated for workpiece vibration frequency of 40 Hz at 10 μm vibration amplitude.

v) Simulation results suggest that a higher flushing speed can be obtained below 40 Hz if vibrating amplitude larger than 10 μm is possible without initiating damaging sparks.

vi) Experimental results suggest high flushing speed of the by-product leads to deeper and sharper an ECM profiles. More particles are pushed away from the workpiece surface during the first half of a vibrating cycle, and they are swept away by electrolyte flow during the cycle's second half.

Future work should be focused on following aspects:

i) Implement the pulsed and horizontal vibration assisted ECM on Domex 550 HSLA steel to compare with investigating results for 1018 steels.

ii) This study utilizes hollow electrodes for high aspect ratio ECM. For low aspect ratio application, it is desirable to extend the simulation using a solid cathodic electrode on an anodic workpiece.

iii) Unisize spherical particles were used in this study, further study should consider the interactions between different shapes and different size of by-product particles.

iv) Since the ionization process and flow affect by temperature, future works should consider the effect of temperature and vibration on ECM results.

REFERENCES

1. Feng, Z., et al., *Flushing Enhancement with Vibration and Pulsed Current in Electrochemical Machining.* International Journal of Engineering Materials and Manufacture, 2017. **2**(4): p. 67-85.

2. Lee, E.S., *Machining Characteristics of the Electropolishing of Stainless Steel (STS316L).* International journal of Advanced Manufactural Technology, 2000. **16**: p. 591-599.

3. McGeough, J.A., *Principles of electrochemical machining*. 1974, London: Chapman and Hall.

4. Feng, Z., et al. *Energy Comparative Study for Mechanical Punching, Electrical-Discharge Machining and Electro-Chemical Machining*. in *5th International Welding, Industrial Engineering and Manufacturing Congress*. 2015. Saltillo, Coahuila, Mexico.

5. Feng, Z., J. Patel, and E. Granda, *Process selection for energy efficiency*, in *American Society for Engineering and Education (ASEE) conference*. 2015: Seattle, Washington, USA.

6. Zhou, C.D., et al., *Electrochemical Machining for Hard Passive Alloys with Pulse Reverse Current.* Transactions of NAMRI/SME, 1997. **XXV**(147-159).

7. Datta, M. and D. Landolt, *Electrochemical machining under pulsed current conditions.* Electrochimica Acta, 1981. **26**(7): p. 899-907.

8. Rajurkar, K.P., et al., *Study of Pulse Electrochemical Machining Characteristics.* CIRP Annals - Manufacturing Technology, 1993. **42**(1): p. 231-234.

9. Rajurkar, K.P., et al., *Modelling and Monitoring Interelectrode Gap in Pulse Electrochemical Machining.* CIRP Annals - Manufacturing Technology, 1995. **44**(1): p. 177-180.

10. Acharya, B.R., C.P. Mohanty, and S.S. Mahapatra, *Multi-objective Optimization of Electrochemical Machining of Hardened Steel Using NSGAII.* Procedia Engineering, 2013. **51**: p. 554-560.

11. Feng, Z., E. Granda, and W. Hung, *Experimental Investigation of Vibration-Assisted Pulsed Electrochemical Machining.* Procedia Manufacturing, 2016. **5**: p. 798-814.

12. Munda, J. and B. Bhattacharyya, *Investigation Into Electrochemical Micromachining (EMM) Through Response Surface Methodology Based Approach.* The International Journal of Advanced Manufacturing Technology, 2008. **35**(7-8): p. 821-832.

13. Rajurkar, K.P. and D. Zhu, *Improvement of Electrochemical Machining Accuracy by Using Orbital Electrode Movement.* CIRP Annals - Manufacturing Technology, 1999. **48**(1): p. 139-142.

14. Munda, J., M. Malapati, and B. Bhattacharyya, *Control of Micro-Spark and Stray-Current Effect during EMM Process.* Journal of Materials Processing Technology, 2007. **194**(1-3): p. 151-158.

15. Ebeid, S.J., et al., *Towards Higher Accuracy for ECM Hybridized with Low-Frequency Vibrations Using the Response Surface Methodology.* Journal of Materials Processing Technology, 2004. **149**(1-3): p. 432-438.

16. Fan, Z.-W., L.-W. Hourng, and C.-Y. Wang, *Fabrication of tungsten microelectrodes using pulsed electrochemical machining.* Precision Engineering, 2010. **34**(3): p. 489-496.

17. Hewidy, M.S., et al., *Electrochemical Machining Under Orbital Motion Conditions.* Journal of Materials Processing Technology, 2001. **109**: p. 339-346.

18. Zhu, D. and H.Y. Xu, *Improvement of Electrochemical Machining Accuracy by Using Dual Pole Tool.* Journal of Materials Processing Technology, 2002. **129**(1-3): p. 15-18.

19. Wang, D., et al., *Reduction of stray corrosion by using iron coating in NaNO3 solution during electrochemical machining.* The International Journal of Advanced Manufacturing Technology, 2014. **76**(5-8): p. 1365-1370.

20. Kozak, J., *Mathematical models for computer simulation of electrochemical machining processes.* Journal of Materials Processing Technology, 1998. **76**(1–3): p. 170-175.

21. Bhattacharyya, B., et al., *Influence of Tool Vibration on Machining Performance in Electrochemical Micro-Machining of Copper.* International Journal of Machine Tools and Manufacture, 2007. **47**(2): p. 335-342.

22. Hewidy, M.S., et al., *Modelling the performance of ECM assisted by low frequency vibrations.* Journal of Materials Processing Technology, 2007. **189**(1-3): p. 466-472.

23. Natsu, W., T. Ikeda, and M. Kunieda, *Generating complicated surface with electrolyte jet machining.* Precision Engineering, 2007. **31**(1): p. 33-39.

24. Natsu, W., S. Ooshiro, and M. Kunieda, *Research on generation of three-dimensional surface with micro-electrolyte jet machining.* CIRP Journal of Manufacturing Science and Technology, 2008. **1**(1): p. 27-34.

25. Zeng, Y.-B., et al., *Enhancement of mass transport in micro wire electrochemical machining.* CIRP Annals - Manufacturing Technology, 2012. **61**(1): p. 195-198.

26. Shin, H.S., B.H. Kim, and C.N. Chu, *Analysis of the side gap resulting from micro electrochemical machining with a tungsten wire and ultrashort voltage pulses.* Journal of Micromechanics and Microengineering, 2008. **18**(7): p. 075009.

27. Wang, S., *Investigation on wire electrochemical cutting with micro-tool vibration.* Journal of Mechanical Engineering, 2010. **46**(13): p. 172-178.

28. Bhuyan, B.K. and V. Yadava, *Experimental modeling and multi-objective optimization of traveling wire electrochemical spark machining (TW-ECSM) process.* Journal of Mechanical Science and Technology, 2013. **27**(8): p. 2467-2476.

29. Lee, C.-L., et al., *Electrochemical Grooving of Si Wafers Using Catalytic Wire Electrodes in HF Solution.* Journal of The Electrochemical Society, 2009. **156**(2): p. H134.

30. Wang, S., et al., *Micro wire electrochemical machining with an axial electrolyte flow.* The International Journal of Advanced Manufacturing Technology, 2011. **63**(1-4): p. 25-32.

31. Wang, W., et al., *Abrasive electrochemical multi-wire slicing of solar silicon ingots into wafers.* CIRP Annals - Manufacturing Technology, 2011. **60**(1): p. 255-258.

32. Zhu, D., K. Wang, and N.S. Qu, *Micro Wire Electrochemical Cutting by Using In Situ Fabricated Wire Electrode.* CIRP Annals - Manufacturing Technology, 2007. **56**(1): p. 241-244.

33. Kurita, T., et al., *Mechanical/electrochemical complex machining method for efficient, accurate, and environmentally benign process.* International Journal of Machine Tools and Manufacture, 2008. **48**(15): p. 1599-1604.

34. Kurita, T. and M. Hattori, *A study of EDM and ECM/ECM-lapping complex machining technology.* International Journal of Machine Tools and Manufacture, 2006. **46**(14): p. 1804-1810.

35. Zhu, D., et al., *Precision Machining of Small Holes by the Hybrid Process of Electrochemical Removal and Grinding.* CIRP Annals - Manufacturing Technology, 2011. **60**(1): p. 247-250.

36. Pajak, P.T., et al., *Modelling the aspects of precision and efficiency in laser-assisted jet electrochemical machining (LAJECM).* Journal of Materials Processing Technology, 2004. **149**(1-3): p. 512-518.

37. Pajak, P.T., et al., *Precision and efficiency of laser assisted jet electrochemical machining.* Precision Engineering, 2006. **30**(3): p. 288-298.

38. Shin, H.S., et al., *Analysis of machining characteristics in electrochemical etching using laser masking.* Applied Surface Science, 2011. **258**(5): p. 1689-1698.

39. Qian, S. and F. Ji, *Investigation on the Aluminum-Alloy Surface with Micro-Pits Array Generating by through Double Mask Electrochemical Machining*, in *AASRI International conference on Industrial Electronics and Application (IEA2015)*. 2015, Atlantis Press.

40. Patel, J.B., et al., *Quality enhancement with ultrasonic wave and pulsed current electrochemical machining.* Procedia Manufacturing, 2017. **10**: p. 662-673.

41. Pa, P.S., *Electrode form design of large holes of die material in ultrasonic electrochemical finishing.* Journal of Materials Processing Technology, 2007. **192-193**: p. 470-477.

42. Skoczypiec, S., *Research on ultrasonically assisted electrochemical machining process.* The International Journal of Advanced Manufacturing Technology, 2010. **52**(5-8): p. 565-574.

43. Rajurkar, K.P., M.M. Sundaram, and A.P. Malshe, *Review of Electrochemical and Electrodischarge Machining.* Procedia CIRP, 2013. **6**: p. 13-26.

44. Deconinck, D., S.V. Damme, and J. Deconinck, *A temperature dependent multi-ion model for time accurate numerical simulation of the electrochemical machining process. Part II: Numerical simulation.* Electrochimica Acta, 2012. **69**: p. 120-127.

45. Deconinck, D., S. Van Damme, and J. Deconinck, *A temperature dependent multi-ion model for time accurate numerical simulation of the electrochemical machining process. Part I: Theoretical basis.* Electrochimica Acta, 2012. **60**: p. 321-328.

46. Alder, G.M., D. Clifton, and F. Mill, *A direct analytical solution to the tool design problem in electrochemical machining under steady state conditions.* Proceedings of the Institution of Mechanical Engineers, Part B: Journal of Engineering Manufacture, 2000. **214**(8): p. 745-750.

47. Prentice, G.A. and C.W. Tobias, *Simulation of Changing Electrode Profiles.* Journal of The Electrochemical Society, 1982. **129**(1): p. 78-85.

48. Moarrefzadeh, A., *Finite-Element Simulation of Dimensional Limitation of ECM Process.* International Journal of Multidisciplinary Sciences and Engineering, 2011. **2**(7): p. 39-43.

49. Purcar, M., et al., *3D electrochemical machining computer simulations.* Journal of Materials Processing Technology, 2004. **149**(1-3): p. 472-478.

50. Kozak, J., D. Gulbinowicz, and Z. Gulbinowicz, *The Mathematical Modeling and Computer Simulation of Pulse Electrochemical Micromachining.* Engineering Letters, 2008. **16**(4): p. 556-561.

51. Bortels, L., et al., *A user-friendly simulation software tool for 3D ECM.* Journal of Materials Processing Technology, 2004. **149**(1-3): p. 486-492.

52. Volgin, V.M. and A.D. Davydov, *Mass-transfer problems in the electrochemical systems.* Russian Journal of Electrochemistry, 2012. **48**(6): p. 565-569.

53. Minazetdinov, N.M., *A hydrodynamic interpretation of a problem in the theory of the dimensional electrochemical machining of metals.* Journal of Applied Mathematics and Mechanics, 2009. **73**(1): p. 41-47.

54. Minazetdinov, N.M., *A scheme for the electrochemical machining of metals by a cathode tool with a curvilinear part of the boundary.* Journal of Applied Mathematics and Mechanics, 2009. **73**(5): p. 592-598.

55. Ma, N., et al., *Pulse Electrochemical Finishing: Modeling and Experiment.* Journal of Materials Processing Technology, 2010. **210**(6-7): p. 852-857.

56. Wu, J., et al., *Study of a novel cathode tool structure for improving heat removal in electrochemical micro-machining.* Electrochimica Acta, 2012. **75**: p. 94-100.

57. Bhattacharyya, B. and J. Munda, *Experimental Investigation on the Influence of Electrochemical Machining Parameters on Machining Rate and Accuracy in Micromachining Domain.* International Journal of Machine Tools and Manufacture, 2003. **43**(13): p. 1301-1310.

58. Bhattacharyya, B. and S.K. Sorkhel, *Investigation for controlled ellectrochemical machining through response surface methodology-based approach.* Journal of Materials Processing Technology, 1999. **86**(1–3): p. 200-207.

59. Dhobe, S.D., B. Doloi, and B. Bhattacharyya, *Analysis of Surface Characteristics of Titanium During ECM.* International Journal of Machining and Machinability of Materials, 2011. **10**(4): p. 293-309.

60. Ayyappan, S. and K. Sivakumar, *Investigation of electrochemical machining characteristics of 20MnCr5 alloy steel using potassium dichromate mixed aqueous NaCl electrolyte and optimization of process parameters.* Proceedings of the

Institution of Mechanical Engineers, Part B: Journal of Engineering Manufacture, 2014.

61. Senthilkumar, C., et al., *Modelling and analysis of electrochemical machining of cast Al/20%SiCp composites.* Materials Science and Technology, 2010. **26**(3): p. 289-296.

62. Senthilkumar, C., G. Ganesan, and R. Karthikeyan, *ECM of Al/15% SiCP Composites Through a Response Surface Methology-Based Approach.* International Journal of Materials Research, 2012. **103**: p. 378-382.

63. Senthilkumar, C., G. Ganesan, and R. Karthikeyan, *Influence of Input Parameters on Characteristics of Electro Chemical Machining Process* International Journal of Applied Science and Engineering, 2013. **11**(1): p. 13-24.

64. Bhattacharyya, B., J. Munda, and M. Malapati, *Advancement in Electrochemical Micro-Machining.* International Journal of Machine Tools and Manufacture, 2004. **44**(15): p. 1577-1589.

65. Rajurkar, K.P., et al., *New Developments in Electro-Chemical Machining.* CIRP Annals - Manufacturing Technology, 1999. **48**(2): p. 567-579.

66. Mathew, R. and M.M. Sundaram, *Modeling and fabrication of micro tools by pulsed electrochemical machining.* Journal of Materials Processing Technology, 2012. **212**(7): p. 1567-1572.

67. Schuster, R., et al., *Electrochemical Micromachining.* Science, 2000. **289**(5476): p. 98-101.

68. Wang, W., et al., *Electrochemical drilling with vacuum extraction of electrolyte.* Journal of Materials Processing Technology, 2010. **210**(2): p. 238-244.

69. Liu, Z., et al., *Investigation of Material Removal Rate in Micro Electrochemical Machining with Lower Frequency Vibration on Workpiece.* International Journal of Machining and Machinability of Materials, 2013. **14**(1): p. 91-104.

70. Ruszaj, A., et al. *Electrochemical machining supported by electrode ultrasonic vibrations*. in *13th International Symposium for Electromachining, ISEM, Spain, May*. 2001.

71. Rebschläger, A., R. Kollmannsperger, and D. Bähre, *Video based Process Observations of the Pulse Electrochemical Machining Process at High Current Densities and Small Gaps.* Procedia CIRP, 2014. **14**: p. 418-423.

72. Ghoshal, B. and B. Bhattacharyya, *Vibration assisted electrochemical micromachining of high aspect ratio micro features.* Precision Engineering, 2015. **42**: p. 231-241.

73. Liu, Z., et al., *Electrochemical Micro Drilling of Stainless Steel with Tool Electrode Jump Motion.* Materials Science Forum, 2009. **626-627**: p. 333-338.

74. Bruggeman, A.G., *Physikalischer Konstanten Von Heterogenen Substanzen.* Annals of Physics, 1935. **24**: p. 636-664.

75. http://www.labworks-inc.com/all_products/shakers/general_purpose/et_132.htm.

76. ANSYS, *ANSYS Fluent Users Guide*. 2016.

77. http://www.nde-ed.org.

78. Kothandaraman, C. and S. Subramanyan, *Heat and Mass Transfer Data Book*. 8th Edition ed. 2013: New Academic Science.

79. Serway, R. and J. Jewett, *Physics for scientists and engineers with modern physics*. 2013: Nelson Education.

80. Zhu, H.P., et al., *Discrete particle simulation of particulate systems: Theoretical developments.* Chemical Engineering Science, 2007. **62**(13): p. 3378-3396.

81. Yu, A.B. and B.H. Xu, *Particle-scale modelling of gas-solid flow in fluidisation.* Journal of Chemical Technology & Biotechnology, 2003. **78**(2-3): p. 111-121.

82. Tsuji, Y., T. Kawaguchi, and T. Tanaka, *Discrete particle simulation of two-dimensional fluidized bed.* Powder Technology, 1993. **77**(1): p. 79-87.

83. Cundall, P.A. and O.D.L. Strack, *A Discrete Numerical Model for Granular Assemblies.* Geotechnique, 1979. **29**: p. 47-65.

84. Xiong, Y., M. Zhang, and Z. Yuan, *Three-dimensional numerical simulation method for gas–solid injector*. Powder technology, 2005. **160**(3): p. 180-189.

85. Li, Y., J. Zhang, and L.-S. Fan, *Numerical simulation of gas–liquid–solid fluidization systems using a combined CFD-VOF-DPM method: bubble wake behavior*. Chemical Engineering Science, 1999. **54**(21): p. 5101-5107.

86. Richardson, J., *Incipient fluidization and particulate systems*. 1971, American Press, London. p. 27-29.

87. Ergun, S. and A.A. Orning, *Fluid Flow through Randomly Packed Columns and Fluidized Beds.* Industrial & Engineering Chemistry, 1949. **41**(6): p. 1179-1184.

88. Choi, H.G. and D.D. Joseph, *Fluidization by lift of 300 circular particles in plane Poiseuille flow by direct numerical simulation.* Journal of Fluid Mechanics, 2001. **438**: p. 101-128.

89. Li, J. and M. Kwauk, *Exploring complex systems in chemical engineering—the multi-scale methodology*. Chemical Engineering Science, 2003. **58**(3): p. 521-535.

90. Morsi, S. and A. Alexander, *An investigation of particle trajectories in two-phase flow systems.* Journal of Fluid mechanics, 1972. **55**(02): p. 193-208.

91. Crowe, C.T., et al., *Multiphase flows with droplets and particles*. 2011: CRC press.

92. Anderson, T. and R. Jackson, *A fluid mechanical description of fluidized beds: Stability of the uniform state of fluidization.* I&EC Fundamentals, 1968. **7**: p. 12-21.

93. Roco, M., *Particulate two-phase flow*. Vol. 1002. 1993: Butterworth-Heinemann Boston, MA.

94. Mei, R., R.J. Adrian, and T.J. Hanratty, *Particle dispersion in isotropic turbulence under Stokes drag and Basset force with gravitational settling.* Journal of Fluid Mechanics, 1991. **225**: p. 481-495.

95. Reeks, M. and S. McKee, *The dispersive effects of Basset history forces on particle motion in a turbulent flow.* The Physics of fluids, 1984. **27**(7): p. 1573-1582.

96. Li, A. and G. Ahmadi, *Dispersion and deposition of spherical particles from point sources in a turbulent channel flow.* Aerosol science and technology, 1992. **16**(4): p. 209-226.

97. Saffman, P., *The lift on a small sphere in a slow shear flow.* Journal of fluid mechanics, 1965. **22**(02): p. 385-400.

98. Oesterle, B. and T.B. Dinh, *Experiments on the lift of a spinning sphere in a range of intermediate Reynolds numbers.* Experiments in Fluids, 1998. **25**(1): p. 16-22.

99. Tsuji, Y., T. Oshima, and Y. Morikawa, *Numerical simulation of pneumatic conveying in a horizontal pipe.* KONA Powder and Particle Journal, 1985. **3**: p. 38-51.

100. Rubinow, S. and J.B. Keller, *The transverse force on a spinning sphere moving in a viscous fluid.* Journal of Fluid Mechanics, 1961. **11**(03): p. 447-459.

101. Hu, H.H., *Direct simulation of flows of solid-liquid mixtures.* International Journal of Multiphase Flow, 1996. **22**(2): p. 335-352.

102. Pan, T.-W., et al., *Fluidization of 1204 spheres: simulation and experiment.* Journal of Fluid Mechanics, 2002. **451**: p. 169-191.

103. http://www.velmex.com/Products/XSlide/XSlide-motorized.html.

APPENDIX A

MODELING OF PARTICLE FLOW

Define:

a_1, a_2, a_3	Constants that apply over several ranges of R_e
A_p	Projected particle surface area (mm^2)
C_d	Particle-fluid drag coefficient
d_p	Particle diameter (m)
F'	Force (N)
F_b	Buoyance force (N)
F_d	Drag force (N)
$\overrightarrow{F_{ij}^{c}}$	Contact force acting on particle i by particle j (N)
$\overrightarrow{F_{i}^{f}}$	Particle-fluid interaction force on particle i (N)
$\overrightarrow{F_{i}^{g}}$	Gravitation force of particle i (N)
$\overrightarrow{F_{ik}^{nc}}$	Noncontact force acting on particle i by particle k or other sources (N)
F_x, F_y, F_z	Body force along the x, y, z direction respectively (N)
m_i	Mass of particle i (g)
M'	Momentum (kg · m/s)
p	Pressure (Pa)
Q'	Energy (J)
R_e	Reynold's number

u, v, w	Electrolyte flow speed at x, y, z direction respectively (m/s)
u', v', w'	Electrolyte flow speed at x', y', z' direction respectively (m/s)
$\vec{v}_i$	Translations velocity of particle i respectively (m/s)
$\vec{V}$	Relative fluid-particle velocity (m/s)
$\overrightarrow{V_F}$	Fluid phase flow velocity (m/s)
$\overrightarrow{V_p}$	Particle flow speed (m/s)
α	Under-relaxation factor for particles, default value is 0.9 for transient flow simulation with unsteady particle tracking, otherwise α is 0.5.
μ	Viscosity of the fluid (Pa·s)
ρ_e	Electrolyte density (g/mm^3)
ρ_F	Fluid density (g/mm^3)
ρ_p	Particle density (g/mm^3)
τ_r	Particle relaxation time
Ω	Relative fluid-particle angular velocity (rad/s)

This appendix details steps to simulate a particle flow between two electrodes in the ECM. Formulas are provided for computational fluid dynamic simulation using ANSYS Fluent software. Referring to Figure 5.1 to Figure 5.3, it is assumed that:

i) The simulation is simplified to a 2-dimension problem.

ii) The simulation location is the top most part of the horizontal ECM electrode-workpiece area.

iii) The iron hydroxide ECM by-products are assumed to be a spherical particle with $\phi 2$ μm diameter.

iv) There is no interaction among particles.

v) Although the electrolyte flow affects the particle, there is negligible effect of the particle to electrolyte flow.

In principle, for any particle-fluid flow system, the dynamic of fluid flow is characterized by i) the solution of Navier-Stokes equations for continuum fluid (primary phase), ii) the solution of Newton's equations of motion for discrete particles (second phase), and iii) initial and boundary conditions [80]. In this appendix, computation fluid dynamics – discrete element method (CFD-DEM) was used to capture the motion of discrete particles since its superior computational convenience when compared with direct numerical simulation – discrete element method (DNS-DEM) and capability to capture the particle physics as compared to two fluid method (TFM) [81]. In CFD-DEM coupling technique, the flow of primary phase (fluid) was determined by the CFD and the motion of second phase (particles) was obtained by solving Newton's equations of motion on a computational cell scale [82].

A.1 Governing Equations

For particle-fluid flow system, particle can have translational and rotational motion. During its movement, the particle may interact with its neighboring particles or walls and interact with its surrounding fluid, through which the momentum and energy are

exchanged. Such movement is not only by the forces and torques originated from its immediately neighboring particles and vicinal fluid, but is also affected by particles and fluids far away through the propagation of disturbance waves [80]. In DEM approach, we introduce a numerical time step which less than a critical value so that disturbance cannot propagate from the particle and fluid farther than its immediate neighboring particles and vicinal fluid [83]. For a coarse particle system, all the resultant forces on a particle can be determined exclusively from its interaction with the contacting particles and vicinal fluid. However, for a fine particle system, non-contact forces, such as van der Waals and electrostatic forces are also taken into consideration.

Since a particle is assumed to be spherical, only translational movement of the particle is considered in this study. The translational motion of discrete particles i with mass m_i follows Newton 2nd law:

$$m_i \frac{d\overrightarrow{v_i}}{dt} = \sum_j \overrightarrow{F_{ij}^c} + \sum_k \overrightarrow{F_{ik}^{nc}} + \overrightarrow{F_i^f} + \overrightarrow{F_i^g} \tag{A.1}$$

Non-contact forces, such as van der Waals force and capillary force, can be neglected since they have little influence on the flushing time. Contact force can also be eliminated since single particle involved in the simulation. Therefore, Equation (A.1) can be simplified to

$$m_i \frac{d\overrightarrow{v_i}}{dt} = \overrightarrow{F_i^f} + \overrightarrow{F_i^g} \tag{A.2}$$

Once the forces in Equation (A.2) are known, this equation can be readily solved numerically. Thus, the trajectories, velocities and transient forces in the system can be determined.

A.2 Particle-Fluid Interaction Forces

The surrounding fluid will interact with particle by generating various particle-fluid interaction forces (drag force), in addition to the buoyance force. For example, the translation of particle was driven by drag force and resisted by stagnant fluid. Thus, particle-fluid interaction forces must be properly considered [80]. Currently, lots of forces have been implemented in DEM simulation, such as drag force, pressure gradient force, unsteady force and lift forces [84, 85].

A.2.1 Fluid-Particle Interaction Drag Force

For a single sphere particle in a fluid, Newton's equation is used to determine the drag resistance force. The particle-fluid drag coefficient, C_d, is dependent upon Reynold's number, R_e, in addition to liquid properties. There are three regions: the Stoke's Law region, the transition region and Newton's law region.

In general, two methods have been used to determine particle-fluid drag fore. The first one is based on empirical correlations for either bed expansion [86] or bed pressure drop experiment [87]. The other method is based on numerical simulations at a microscale, where the technique used the direct numerical simulation [88]. The latter method, although rational, limited by the current computation capability. Currently the numerical studies

have been applied to relatively simple systems. Li and Kuipers [89] did a systematic investigate and quantify the difference among these correlations. Their results reveal that these correlations with similar predictive capability, although their accuracy may differ. In this study, the coefficient adopted from Morsi and Alexander's [90] result. Thus, the fluid-particle interaction drag force can be defied as

$$\overrightarrow{F_f} = \overrightarrow{F_d} + \overrightarrow{F_b} = m\frac{\overrightarrow{V_F} - \overrightarrow{V_p}}{\tau_r} - V_i\rho_F\vec{g} \tag{A.3}$$

$$\tau_r = \frac{\rho_p d_p^2}{18\mu}\frac{24}{C_d R_e} \tag{A.4}$$

$$R_e \equiv \frac{\rho_F d_p\left|\vec{V_p} - \overrightarrow{V_F}\right|}{\mu} \tag{A.5}$$

$$C_d = a_1 + \frac{a_2}{R_e} + \frac{a_3}{R_e} \tag{A.6}$$

A.2.2 Other Fluid-particle Interaction Forces

When the fluid involved is liquid rather than gas, other fluid-particle interaction forces also have been considered, which include the pressure gradient force, unsteady force and lift force [91]

i) Pressure Gradient Force

In general, the pressure gradient force includes both the buoyance force due to gravity and acceleration pressure gradient in fluid, defined as [92]

$$F_p = -V_p \frac{dp}{dx} = -V_p \rho \left(\vec{g} + \vec{V}_F \frac{d\vec{V}_F}{dx} \right) \tag{A.7}$$

It is general validity and all relevant contribution are included when dp/dx is evaluated from the fluid equation of motion.

ii) Virtual Mass Force and Basset Force

Unsteady mainly including the virtual mass force and Basset force. The virtual mass force relates to the force required to accelerate the surrounding fluid, and is also called the added mass because it is equivalent to adding a mass to a particle, is defined as [93]

$$\vec{F}_{vm} = C_{vm} \frac{\rho_F}{\rho_p} \left(\vec{V}_p \nabla \vec{V}_F - \frac{d\vec{V}_p}{dt} \right) \tag{A.8}$$

where C_{vm} is the virtual mass coefficient which typically has a value of 0.5. The virtual mass effect is significant when the second phase density is much small than the primary phase density (for example, for a transient bubble column).

The Basset force describes the force due to the lagging boundary layer development with changing relative velocity. It accounts for the viscous effects, and defined as [94, 95]

$$F_B = \frac{3}{2} d_p^2 \sqrt{\pi \rho_F \mu} \left[\int_0^t \frac{\left(\dot{\vec{V}}_F - \dot{\vec{V}}_p \right)}{\sqrt{t - t'}} dt' + \frac{\left(\vec{V}_F - \vec{V}_p \right)_0}{\sqrt{t}} \right] \tag{A.9}$$

The virtual mass and Basset force are not important when the density of the fluid is much lower than the density of the particle. In this investigation, these forces are neglected.

iii) Saffman Lift Force and Magnus Lift Force

The lift force, including Saffman lift force and Magnus lift force, on a particle due to the rotation of the particle. The Saffman lift force, or life due to shear, can also be include in the additional force term as an option. The lift force used is from Li and Ahmadi [96] which is a generation of the expression provided by Saffman [97]

$$\vec{F}_S = \frac{2K\nu^{1/2}\rho d_{ij}}{\rho_p d_p (d_{lk} d_{kl})^{1/4}} \left(\vec{v}_F - \vec{v}_p\right) \tag{A.10}$$

where K=2.594 and d_{ij} is the deformation tensor. This form of the lift force is intended for small particle Reynolds numbers and is recommended only for sub-micron particles. Thus, this force is neglected in this investigation.

On the other hand, the Magnus force, or rotational lift force, is caused by a pressure differential along a particle surface resulting from the velocity differential due to rotation. For high Reynolds number, the Magnus force F_{RL} is scaled by a rotational lift coefficient C_{RL}. The Maguns lift force was defined as [91]

$$\vec{F}_{RL} = \frac{1}{2} A_p C_{RL} \rho \frac{\left|\vec{V}\right|}{\left|\vec{\Omega}\right|} \left(\vec{V} \times \vec{\Omega}\right) \tag{A.11}$$

For the rotational life coefficient C_{RL}, different approaches are available in the literature, as follows.

a) Oesterle and Bui Dinh [98]

C_{RL} is dependent on both the rotational Reynolds number Re_ω and the particle Reynolds number Re_p and this formulation agrees well with experiment for $Re_p < 2000$

$$C_{RL} = 0.45 + \left(\frac{Re_\omega}{Re_p} - 0.45\right)\exp\left(-0.05684 Re_\omega^{0.4} Re_p^{0.3}\right) \tag{A.12}$$

b) Rsuji et al. [99]

C_{RL} is defined as a function of the spin parameter S_{spin} as follows, this formulation is widely used with validity up to $Re_p < 1600$.

$$C_{RL} = \begin{cases} 0.4 & for\ S_{spin} \geq 1 \\ (0.4 \pm 0.1)S & for S_{spin} < 1 \end{cases} \tag{A.13}$$

where

$$S_{spin} = \frac{|\vec{\omega}_p| d_p}{2|\vec{V}_F - \vec{V}_p|} \tag{A.14}$$

c) Rubinow and Keller [100]

C_{RL} is linearly proportional to the spin parameter S and this model could be useful for comparison purpose in academic applications.

$$C_{RL} = 2S \tag{A.15}$$

However, in this investigation, research interest was only focus on the particle translation. Rotation movement and the relevant effect due to rotation also neglected. Therefore, by combining Equations (A.2) and (A.3), Equation for particle motion becomes:

$$\frac{d\overrightarrow{v_i}}{dt} = \frac{\overrightarrow{v_F} - \overrightarrow{v_p}}{\tau_r} + \frac{\vec{g}(\rho_p - \rho)}{\rho_p} \tag{A.16}$$

A.3 Fluid-Particle Flow Modeling

A.3.1 Particle Movement Modeling Approaches

Currently, techniques to modeling the particle movement in fluid-particle flow system can be classified into two categories: the continuum approach at a macroscopic level and discrete approach at a microscopic level.

In continuum approach, the macroscopic behavior was described by balance equations, e.g., mass and momentum are used in the two-fluid model (TFM), closed with constitutive relations combined with boundary/initial conditions. Since the computational efficiency advantage of this approach, it is popular in process modeling and applied research. Its effective use largely depends on closure or constitutive relations and momentum exchange between different types of particles. However, there is no general accepted continuum theory that can applied to all flow conditions. The usage of this approach is strictly limited.

In discrete approach, particles movement are analyzed individually which makes this technique has advantage that there is no need for global assumptions on the solids, such

as steady-state behavior, uniform constituency and constitutive relations [80]. This method considers a finite number of isolated particles interacting through contact/non-contact forces, and each particle was described by Newton's equations of motion. In this study, ANSYS fluent is used to simulate single particle flow which particle-particle interaction forces are eliminated. In addition, Star CCM+ is used to simulate multiple particles flow which can capture the particle-particle interaction in fluid-particle flow system.

A.3.2 Discrete Element Methods

There are two types of discrete particle methods which generally used: DNS-DEM and CFD-DEM.

In DNS-DEM, the primary phase (fluid) was resolved at a scale comparable with the particle spacing while particles are treated as discrete moving boundaries [101]. Fluid-particle system is treated implicitly though introduce a combined weak formulation, which is a key feature of DNS-DEM. DNS has great potential to produce detailed results of hydrodynamic interactions between fluid and particles in a system [102]. However, impossible to handle with particle collisions was a major disadvantage of this technique.

In CFD-DEM technique, the primary phase (fluid) flow was determined by the CFD on a computational cell scale and the second phase (particles) was obtained by solving Newton's equations of motion [82]. The governing equations for fluid is Navier-Stoke equations which was same as TFM approach. The CFD-DEM technique is promising since

its superior computational convenience and capability to capture the particle physics, such as, trajectories and velocities. Therefore, CFD-DEM approach was selected in this study.

A.3.3 CFD-DEM Coupling Schemes

In CFD-DEM approach, the motion of discrete particles is described by DEM based on Newton's laws of motion applied to isolated particles and the flow of continuum fluid is described by the CFD based on the local averaged Navier-Stokes equations. The modeling of particles flow is at individual particle level and the modeling of fluid flow by CFD is at computation cell level. At each step, DEM will give information, such as locations and velocities of individual particle, for the evaluation of porosity and volumetric fluid drag force in a computational cell. CFD will then use these data to determine the fluid flow field which then yields the fluid drag forces acting on individual particles. Incorporation of the resulting forces into DEM will produce information about the motion of individual particles for next time step. At each time step, the fluid-particle interaction forces on individual particles in a computational cell are calculated first, and the values are then summed to produce the particle-fluid interaction force ate the cell scale, as shown in following equations.

$$F'_{new} = F'_{old} + \alpha(F'_{calculated} - F'_{old}) \quad \text{(A.17)}$$

$$Q'_{new} = Q'_{old} + \alpha(Q'_{calculated} - Q'_{old}) \quad \text{(A.18)}$$

$$M'_{new} = M'_{old} + \alpha(M'_{calculated} - M'_{old}) \quad \text{(A.19)}$$

For fluid phase, the governing equations derived from Navier-Stoke equations comply with the law of conservation of mass and momentum in terms of local-average variables:

$$\rho_e\left(\frac{\partial u}{\partial t}+u\frac{\partial u}{\partial x}+v\frac{\partial u}{\partial y}+w\frac{\partial u}{\partial z}\right)=F_x-\frac{\partial p}{\partial x}+\mu\left(\frac{\partial^2 u}{\partial x^2}+\frac{\partial^2 u}{\partial y^2}+\frac{\partial^2 u}{\partial z^2}\right) \tag{A.20}$$

$$\rho_e\left(\frac{\partial v}{\partial t}+u\frac{\partial v}{\partial x}+v\frac{\partial v}{\partial y}+w\frac{\partial v}{\partial z}\right)=F_y-\frac{\partial p}{\partial y}+\mu\left(\frac{\partial^2 v}{\partial x^2}+\frac{\partial^2 v}{\partial y^2}+\frac{\partial^2 v}{\partial z^2}\right) \tag{A.21}$$

$$\rho_e\left(\frac{\partial w}{\partial t}+u\frac{\partial w}{\partial x}+v\frac{\partial w}{\partial y}+w\frac{\partial w}{\partial z}\right)=F_z-\frac{\partial p}{\partial z}+\mu\left(\frac{\partial^2 w}{\partial x^2}+\frac{\partial^2 w}{\partial y^2}+\frac{\partial^2 w}{\partial z^2}\right) \tag{A.22}$$

$$\frac{\partial u}{\partial x}+\frac{\partial v}{\partial y}+\frac{\partial w}{\partial z}=0 \tag{A.23}$$

Figure 5.3 in main text shows the simulation boundaries. A spherical particle P starts at the lower left corner of the two-dimensional 300 μm × 300 μm simulation area. The vibration of the workpiece (governed by vibration frequency and amplitude) alters the position of this particle. The flow chart in Figure A.1 shows how position and velocity of the particle P are calculated. After each iteration, the position y_p of the particle is compared against the vertical boundary; when the particle exits the vertical boundary (y_p > 300 μm) then the simulation would end. A simulation flow chart is shown in Figure A.1.

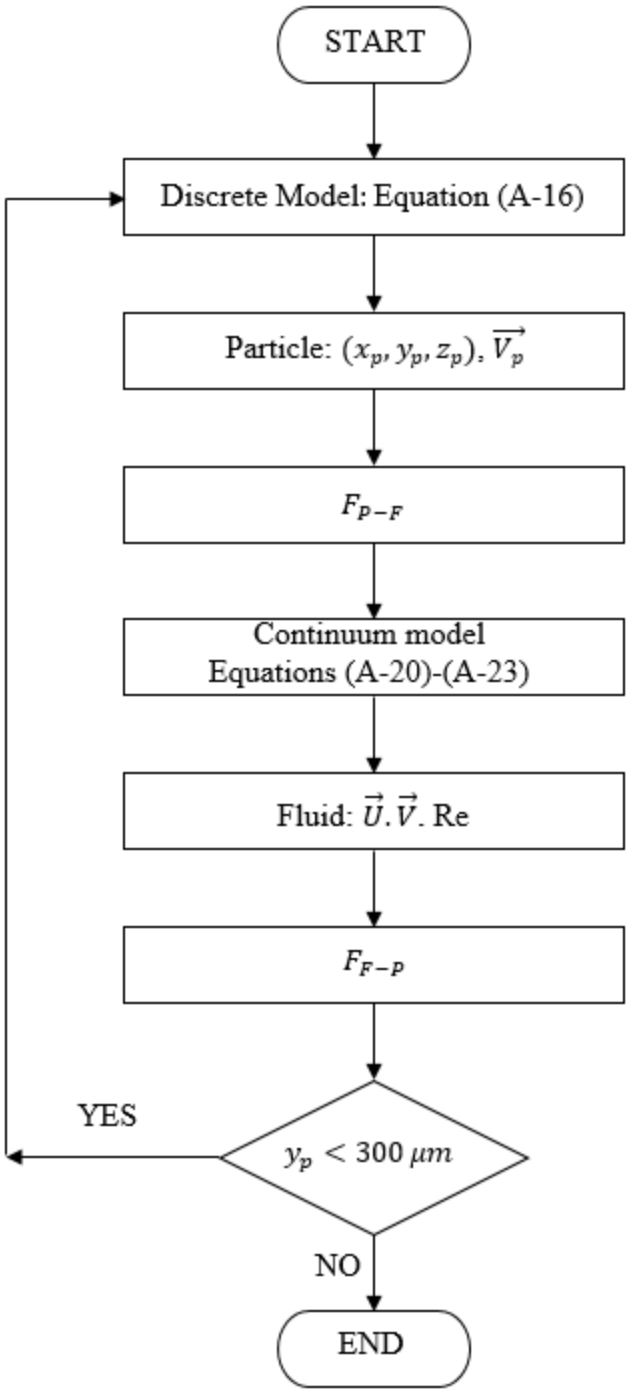

Figure A.1 Flow chart of simulation.

APPENDIX B

EQUIPMENT

The equipment used in experiments is listed in Table B.1. The detail specifications of these equipment are illustrated below.

Table B.1 List of equipment in experiment.

1	Agilent 33250A waveform generator	Figure B.2
2	Labworks pa-151 linear power amplifier	Figure B.3
3	Labworks ET-132 electrodynamic shaker	Figure B.4
4	Velmex Xslide system	Figure B.6
5	Velmex VXM controller system	Figure B.7
6	Everlast Power TIG 255EXT power supply	Figure B.8
7	Longer WT600-2J peristaltic pump	Figure B.10
8	Hannah HI8733 conductivity meter	Figure B.12
9	OMEGA HH374 4-channel data logger thermometer	Figure B.13
10	Stainless steel tube with Teflon coating	Figure B.14
11	Alicona Infinite Focus	Figure B.15

B.1 Workpiece Vibration System

Workpiece vibration system includes a waveform function generator, a linear power amplifier and an electrodynamic shaker. Signal flow in vibration system is shown in Figure B.1. Waveform generator (Figure B.2) generate a specific waveform and transmit this signal to power amplifier (Figure B.3). The signal will be amplified by power amplifier and be transmitted to electrodynamic shaker (Figure B.4) to drive the shaker vibrate. The vibration frequency of electrodynamic shaker is same as the waveform frequency. The relationship between electrodynamic shaker vibration amplitude and the gain of power amplifier (Figure B.5).

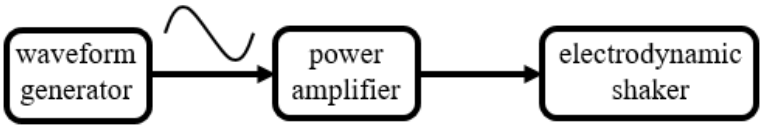

Figure B.1 Signal flow in vibration system.

B.1.1 Waveform Generator

Agilent 33250A, as shown in Figure B.2, is a high-performance 80MHz synthesized function generator with built-in ramp, triangle, noise, DC and other waveforms. Its combination of bench-top and system features makes this function generator a versatile solution for testing requirement.

Figure B.2 Agilent 33250A 80 MHz waveform generator.

B.1.2 Labworks pa-151 linear power amplifier

Labworks pa-151 linear power amplifier, as shown in Figure B.3, is a high quality, convection-cooled, direct-coupled audio amplifier primarily intended for use with small electro-dynamic vibration systems.

Figure B.3 Labworks pa-151 linear power amplifier.

B.1.3 Labworks ET-132 Electro-Dynamic Shaker

Labworks ET-132 electrodynamic shaker, as shown in Figure B.4, transforms electrical current into mechanical force for the purpose of vibration testing. A shaker consists of a magnet structure and a moving coil. Force is generated in the moving coil by interaction between current flowing in the coil and the magnetic field in which the coil is placed. An

alternating current in the coil will produce an alternating force and resultant motion at the same frequency in the coil. The moving coil and the force-transmitting structure is called the armature. The force generated in the armature coil is always defined by Equation (5.4) in main text.

Figure B.4 Labworks ET-132 electrodynamic shaker.

Thus, the force-current ratio is constant for a particular shaker. The experimental relationship between gain and vibration amplitude is shown in Figure B.5.

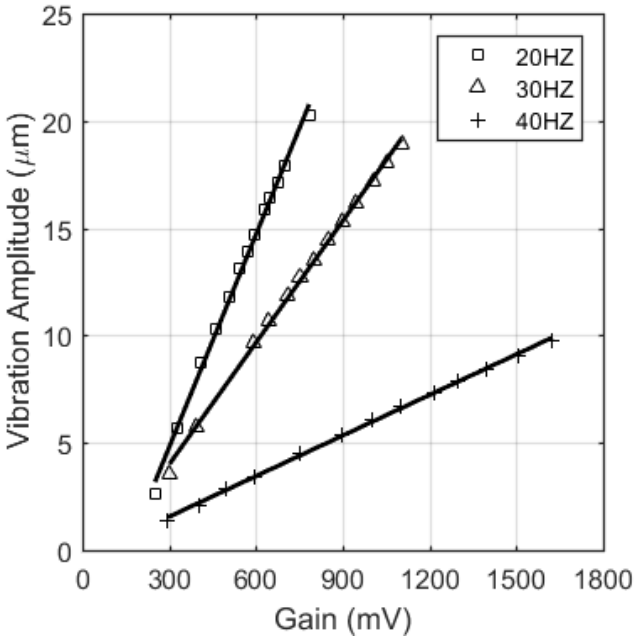

Figure B.5 Relationship between vibration amplitude and gain.

B.2 Tool Feeding System

The computed numerical control tool feed system includes 2 Velmex motorized Xslide frame and assembled in the $x - z$ direction (Figure B.6). A programmable VXM-3 controller system (Figure B.7) used to control the movement of feeding system.

The Velmex Xslide is a compact positioning stage highly suitable for high performance incrementing. Their compact design makes them ideal for limited space applications. This system has a load capacity of 15.9kg horizontally and 4.5kg vertically. Straight-line accuracy is (0.076 mm per 25 cm). Feed speed ranging from 2.5 µm/s~5000 µm/s. Repeatability is 0.00025 mm [103].

Figure B.6 Velmex XSlide system.

Figure B.7 Velmex VXM controller system.

B.3 Pulsed-DC Power Supply

The digital inverter-based EVERLAST PowerTIG 255 EXT DC power supply, as shown in Figure B.8, delivers adjustable pulsed current due to the microprocessor insider. The output pulsed current with peak current ranging from 3 A ~ 150 A, pulsed frequency up to 500 Hz and duty cycle ranging from 1% - 99%. A typical pulsed current generated

from this power supply is shown in Figure B.9, I_p is the peak current which adjustable from 3-150A, I_b is the minimum current which is 5% of peak current I_p, I_0 is the initial current, 5 A minimum.

Figure B.8 Everlast Power TIG 255EXT power supply.

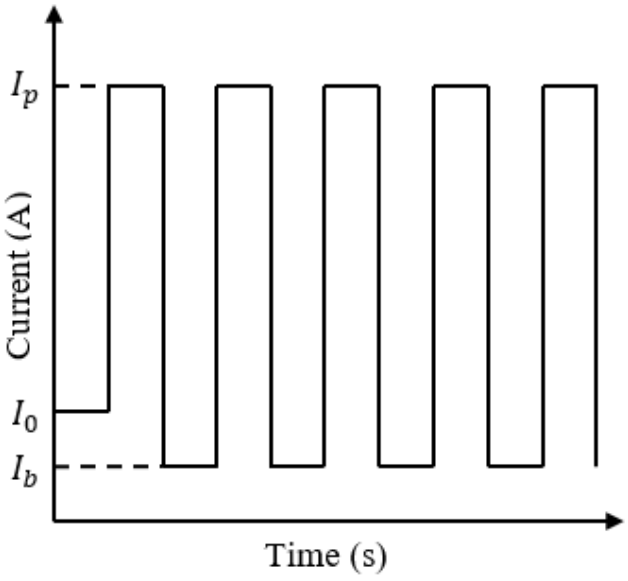

Figure B.9 Pulsed DC current output.

Figure B.10 Longer WT600-2J high flow rate peristaltic pump.

B.4 Electrolyte Circulation and Monitor System

Longer WT600-2J peristaltic pump with KZ25 pump head, as shown in Figure B.10, provides flow range from 0 to 5000 ml/min with variable pump heads and tubes. Its speeding can be adjusted manually or automatically through external control to get the suitable flow rates. The specification pump rate and the actual pump rate are shown in Figure B.11.

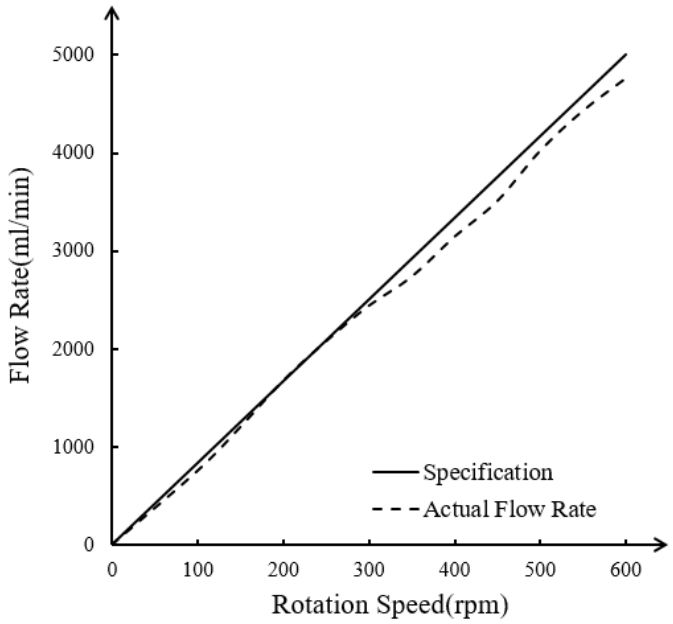

Figure B.11 Calibration results of Langer WT600-2J peristaltic pump.

The Hannah HI 8733 is a durable, portable electric conductivity meter offers versatile and accurate solution for conductivity readings, as shown in Figure B.12. It offers four measurements ranges from 0.0 µS/cm to 199.9 mS/cm with ± 1% FS accuracy. . Conductivity readings are adjusted with Automatic Temperature Compensation (ATC), assuring user of consistent and accurate measurements.

B.5 Temperature Monitor System

The OMEGA HH374 4-channel data logger thermometer has a high resolution and fast analog to digital converter, as shown in Figure B.13. Measurements setting and results can be stored in the meter or directly saved on a computer through PC interface for further analysis. This instrument provides a measurement range of -200 °C to 1370 °C with the accuracy of ±1%.

Figure B.12 Hannah HI 8733 conductivity meter.

Figure B.13 OMEGA HH374 4-channel data logger thermometer.

B.6 Cathodic electrode

Stainless steel tubes (ϕ9.5 mm OD, 0.3 mm thick), as shown in Appendix Figure B.14, were selected as a cathodic electrode. About 13 mm ends were commercially coated with DuPont 954G-304 nonconductive layer with 25 μm thick on both outside and inside

diameters. These coatings are suitable for used in conditions of mild abrasion, relatively low operating temperatures and for chemical and corrosion resistance.

Figure B.14 Stainless steel cathodic electrode with Teflon coating.

B.7 Metrology System

Alicona InifiniteFocus is a non-contact, optical, three-dimensional based microscope which combines a 3D micro coordinate measurement machine and surface roughness measurement device in one system, as shown in Figure B.15. The range of measurable volume is 100 mm × 100 mm × 100 mm with surface resolution of 100 nm and height resolution of 50 µm. The minimum measurable radius is 3 µm , minimum measurable roughness $S_a = 0.075$ µm and $R_a = 0.15$ µm. This machine provides traceable measurements with high resolution, high repeatability and high accuracy.

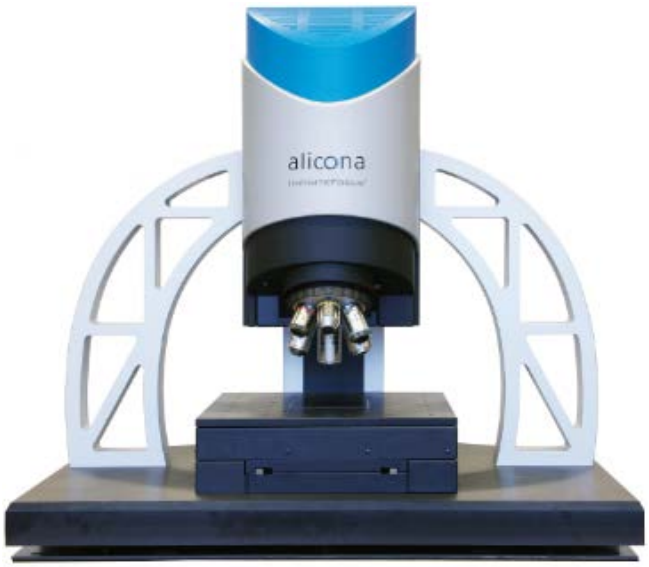

Figure B.15 Alicona Infinite Focus.